POLITECNICO DI TORINO

Master of Science

in Mechanical Engineering

Master's Thesis

Analysis of Diesel Spray and Combustion in CI Engine by Means of CFD Modeling

Supervisors

Prof. Ezio Spessa
Prof. Daniela A. Misul
Prof. Mirko Baratta
Prof. Prashant Goel

Candidate

Stefano Martone

April 2021

Acknowledgements

The author wishes to thank the Professors Ezio Spessa, Daniela A. Misul, Mirko Baratta and Prashant Goel of the Energy Department of Politecnico di Torino for the opportunity to partecipate and work on this project. Special thanks are addressed to Prof. Prashant Goel and Ing. Riccardo Cirulli for supporting me in this work. In addition, the author wants to thank his family, dad Franco, mom Vittoria and my brother Luca, for the support shown in every single decision. Finally, a special thank is addressed to the whole group “Tutto Bene?” for the love show me in this period

“There is no success without struggle”

Dedicated to my grandparents:

Abstract

This work is part of a research activity carried out at the Politecnico di Torino, by the Energy Department under the supervision of the Prof. E. Spessa, Prof. D. A. Misul, Prof. M. Baratta and Prof. P. Goel. In patnership with ENI, the project includes a research activity to investigate the effects of using the HVO, a very high-quality bio-based diesel fuel, rather than a conventional diesel fuel. The starting point has been the development of a CFD Compression Ignition model for a light-duty commercial vehicle, fueled by a conventional Diesel fuel. In the following work of thesis, the first step has been an approach to the formulation of fuel surrogates able to reproduce the behaviour of a conventional Diesel fuel. The spray CFD model for the resulting surrogates, labelled as D2 surrogate and NS2, has been calibrated and the experimental data, available on the ECN platform, are validated against the numerical results in terms of ignition delay. To improve the characteristics of the atomization process for the D2 surrogate, a recalibration process was carried out. In conclusion the surrogates were validated on a 45-degree sector of the symmetrical combustion chamber from the Intake Valve Closing to the Exhaust Valve Opening, whose engine performance has been simulated at 2000 rev/min and full load 19 bar BMEP. The models are validated against the experimental data in terms of in-cylinder pressure and heat release rate. The characteristic of the hydrotreated vegetable oil and the ENI project will be described in the introductory part of this thesis. A theoretichal overview on flow and combustion in Diesel engines, a CFD fundamentals and the CONVERGE CFD Software will be describe in the first part. The second part will focuse on the development of the Diesel surrogate approach. The spray model using the Diesel surrogates will be calibrated and compared with the experimental data in the third part. The Diesel surrogate fuels will be validated on the sector engine model in the fourth part. In the fifth part the conclusions, next steps and possible future devolepment of the project will be described.

Contents

List of Figures

List of Tables

1 A resource for the future: HVO

1.1 Introduction

Climate change is a reality of world interest, which is leading inexorably to catastrophic effects, such as the disruption of the ecosystems and the wealth of biodiversity that sustains our lives. One of the main causes is associated with high levels of CO_2 emissions. In 2020, the EU and its member states signed the so-called Paris Agreement, which was the first legally binding and universal agreement on climate change. Its main features were to contain the increase in global warming at a temperature of 1.5 º C, as well as to implement a plan to halve CO_2 emissions by 2030 [1]. Today, it is estimated that more than a quarter of global greenhouse gas emissions in the EU come from the transport sector, of which cars, trucks, buses, vans occupy the 70% [2]. The transport world not only emits greenhouse gases such as CO_2, but also includes other polluting species, such as: carbon monoxide, nitric oxide, HC and particulate matters. Which have harmful effects on human health and are generated by an imperfect combustion process. Focusing on the automotive sector, the objective is to achieve the efficiency targets, ie limit the fuel consumption and consequently the emission levels of CO_2. In which way? Adopting an approach capable of reaching a mix of efficient solutions to improve the combustion system but also introducing alternative solutions such as powertrain electrification and biofuels introduction.

1.2 Switch to biofuels

To contain the global warming, it was necessary to introduce powertrain at low green house gas emission. For this reason, the use of biofuels in the transport sector for reducing vehicle fuel consumption and to minimise related pollution, has attracted the attention of all countries in the world. New policy regarding the introduction of the biofuels in the sector transport have been developed. For example in 2018 the following policies were undertaken:

- The European Union, has promoted the achievement of 14% share of biofuels previewed for 2030 [3]
- United States, has planned 136 billion litres of biofuels for 2022 [3]

The biofuel is produced by fermentation processes or production of vegetable oils which are esterified, starting from a starting biomass, such as sugar cane and rape seed. In this way the CO_2 produced by the engine combustion process will be equal to the CO_2 amount that the biomass has accumulated during its life cycle, the balance of CO_2 will be theoretically equal to zero. Looking at the starting biomass and the technological process, the following classifications can be defined:

- Conventional biomass, for which the starting biomass may have a food destination. In this case the disadvantage is associated with an impact on land use, so called ILUC (Indirect Land Use Change) risk. For example, ethanol which is the main solution in spark ignition

engines, is produced by a fermentation process of biomass such as sugar cane, sugar beet, corn or cereals
- Advanced biomass, are produced from biomass with low risk ILUC, such as used oil or waste biomass
- Conventional process, the resulting fuel is generated by fermentation and transesterification processes, and the chemical structure is influenced by the starting biomass
- Advanced process, the final fuel is generated by different processes starting with vegetable oils and chemical structure is not influenced by the starting biomass

The ideal scenario was to realize a biofuels, starting from advanced biomass subjected to advanced technological processes. In this perspective other solutions are being made, like the HVO

1.3 Hydrotreated Vegetables Oil

The hydrotreated Vegetables Oil (HVO) is produced from vegetable oils, animal fat and waste cooking oils, which are subjected to a refinery-based process called hydrogenolysis. In this process, under standard temperature conditions of 350-450 °C, the oxygen is removed from the triglyceride thanks the use of hydrogen in presence with a catalyst. In this way the reaction promotes the breaking of single carbon-heteroatom bond [4]. HVO is the result of a process of conversion of vegetable oils and animal fat into paraffinic hydrocarbons and is presented as a mixture of normal and iso-paraffin, which do not contain sulfur and aromatics (hydrocarbons responsible in part for the formation of soot particles) and have a high cetane number. For this reasons, HVO is one of the possible alternatives to diesel fuel [5]. To understand the benefits that we can obtain from the use of HVO, it is necessary to present a comparison with the physical-chemical properties of diesel fuel. From test fuel properties carried out by Neste Oil, which made a hydrotreated vegetable oil called NExBTL, the main properties of NExBTL and diesel fuel and their comparison are described in table below:

Properties	Unit	HVO (NExBTL)	Diesel fuel
Viscosity (40°C)	mm^2/s	2.99	2.68
Density (15°C)	kg/m^3	779.9	835.7
Heating value	MJ/kg	43.7	42.9
Cetane number	-	88.2	53
Aromatics	vol%	0	19.7
Paraffin	vol%	100	-
Sulfur	ppm	3	6
H/C ratio	-	2.14	1.88
Cloud point	°C	-12	-14

Table 1-1 Fuel properties comparison [5]

The following considerations can be established from the comparison:

- Under the same temperature conditions, the viscosity of HVO shows an increase of 11.5 % while the density has a reduction of 6.67 % compared the diesel fuel
- Under normal temperature and pressure conditions, the heating value of HVO is 5 % lower per volume than diesel, for this reason the HVO fuel injected under full load conditions, could cause a reduction in torque
- The high cetane number of HVO, may cause a reduction in unburned hydrocarbons (HC) and carbon monoxide (CO) emissions
- The diesel fuel has an aromatic content of 19.7% under normal conditions, but the great advantage for HVO is to have a concentration of aromatics equal to zero. This implies that HVO is potentially capable of drastically reducing PM emissions
- The low sulfur concentration for HVO fuel represents another advantage, in fact after the combustion, sulfur from fuel diesel creates sulfuric acid, which causes corrosive wear on the metal surface of an engine
- The distillation curves shows that HVO fuel has fewer components distilling apporximately between 260 and 300 °C, this is effect is due to the HVO fuel has fewer low-boiling components. This could cause a worsening of the fuel spray and evaporization characteristics under cold-start conditions

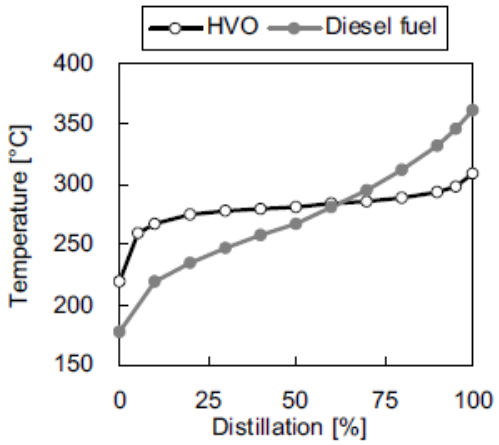

Figure 1-1-Distillation Curves of Test Fuels [5]

- Using pure HVO fuel, CO_2 emissions could be reduced due to a lower C/H ratio [6]

Focusing on the comparison between the HVO and the traditional biofuel using for diesel engine applications, such as Fatty Acid Methyl Ester (FAME), the results showed that this type of biofuel is characterized by a worse oxidation stability than HVO, which does not contain unsaturated components. In addition, the use of high concentrations of FAME mixed with diesel fuel might cause harm to the diesel aftertreatment system (for example Diesel Particulate Filter) and for the vehicle fuel systems. For these reasons, it is recommended the use only of low concentration of FAME blend that can be used as automotive fuels, while the HVO fuel can be adopted in direct injection diesel both pure and at various blend ratios.

1.4 The interest of ENI

Over the years, the growing focus on reducing global warming and reducing pollutant emissions has attracted the attention of many companies, including the Italian company ENI S.p.A. which began a research activity with the energy department of the Politecnico di Torino, to investigate the potential and future application of the bio-fuel HVO, which is produced by them. In this way, the ENI company can boast two biorefinery located in Italy. The first located in Venezia, in which 230000 tons per year of vegetable oils are treated and converted since 2014, while the second located in Gela can boast since 2019 a production capacity of 750000 tons per year of used vegetable oils, animal fats, frying fats to produce high quality biofuels [7]

2 Compression-Ignition Engines Overview

The Compression-Ignition engines, fueled by diesel, showed in time a strong interest in the automotive sector. The interest is justified by the numerous advantages that a Diesel engine can offer. Higher fuel conversion efficiency and higher volumetric efficiency compared to the Spark ignition engine. In fact, compared to the latter, a Compression-Ignition engine has the advantage of having a higher volumetric compression ratios, which changes from 12 to 24 [8], and an higher volumetric efficiency (load control does not require a throttle but only the variation of the the amount of fuel injected each cycle is required). Another feature of the Compression-Ignition engines is to be powered with high-reactivity fuels, which influence the combustion process. The foremost fuel is the diesel, whose reference hydrocarbon is Cetane C_nH_{2n+2}, composed of a long and flexible molecular structure, thanks to which intermediate reactions can occur faster under high conditions of pressure and temperature [9]. Before the desiderated start of combustion, the fuel is injected as a high-pressure liquid spray into the compressed air. The liquid jet proceeds with the velocity of a “projectile” in the environment where the air density can be 20 ÷ 30 times larger than that in standard conditions. From the impact with the “wall air” the liquid is subjected to the fragmentation in a myriad of droplets, called atomization process. The fuel droplets surrounded by high temperature air, are subject to the heat flow that causes the evaporation of them. Fuel vapors are mixed with the surrounding air and the combustion process occurs spontaneously during the compression stroke due to the high reactivity of the fuel. The time of these processes are not influenced by the variation of the turbolence into the cylinder, therefore thery are not able to self-adapt to the engine speed variation, for this reason the engine speed in Compression-Ignition engine is limited to 5000 rpm. Despite this combustion process is more complex than that Spark-Ignition, is not subjected to combustion anomalies, such as the knocking, this allow to use a larger bore diameter than the gasoline engine, for example the largest bore diameter in the world is of a Compression-Ignition engine in the naval field and equal to 900mm [9] and an higher volumetric compression ratios.

2.1 Charge motion within the cylinder

The combustion process and the mixing air-vapor fuel are influenced by the gas motion in the engine cylinder. This condition has a relevant impact on the heat transfer. In this way the turbolence characteristics and the bulk gas motion are very important. The initial in-cylinder flow pattern is based on the intake process and can vary during compression [8]

2.1.1 Intake Jet Flow

The engine intake process controls many important aspects of the flow within the cylinder. In four-stroke engine, the intake valve offers the minimum area to the gas characterized by the highest set velocity for the intake process. From the valve opening, the flow is discharged into the cylinder such as a conical jet which the axial and the radial velocities are 10 times the mean piston speed. Under this condition, the jet separates from the valve seat and lip, where the turbolence is

generated due to the production of shear layers with large velocity gradients [8]. During the intake process, the highly non-homogeneous motion of the air produced during this phase is generated by the jet from the valve. Which expands into the cylinder and interacts with the geometry of the system, creating a series of vortices on the circumferential and axial plane. This characteristic is due in part to the viscosity of the fluid and to impacts between the flow against the walls of the cylinder and piston. The generated turbulence turns out to be anisotropic (it has main directions) and non-homogeneous (it varies from point to point), in the second part of the intake process the turbulence quickly decrease, because the momentum of the jet expires. When the intake valve is closed, some aspects of the charge motion have greater resistance over time and can exert their influence longer. Organized motions such as swirl are promoted by the geometry of the cylinder and tend to retain their energy during the compression phase. In fact, during the compression stroke, the change in length scale and the increase of density have effect to amplifying the turbolence level. A further increase of the turbolence level occurs during the combustion process, after which turbolent motions are suppressed also due to decreased viscosity [10].

2.1.2 Organized motions in the cylinder: Swirl

This term refers to an organized rotation of the charge about the cylinder axis. Swirl is created by bringing the intake flow into the cylinder with an initial angular momentum, while some decay in swirl due to friction occurs during the engine cycle. The intake generated swirl persists through the compression, combustion, and expansion processes. Swirl is usually suitable for Diesel engine and Direct-Injection engine because it increases the mixing of the fuel jet into the cylinder [8]

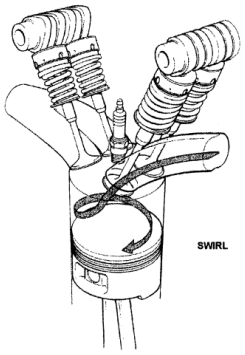

Figure 2-1 Swirl rappresentation [11]

There are two different approaches to generating swirl motions. In the first, the tangential rotatory motion is produced into the cylinder. In this way directed port are used, fig. 2-2, which give the flow jet coming out of the valve a non-homogenous velocity distirbution on the circumference so as to orient the flow towards the cylinder wall which in turn imposes a tangential motion. This approach is not particularly effective as a swirl generator, in fact the small intake valve rises due to the low flow rate in the intake pipe. The higher lift of the intake valve is more effective in

generating swirl motion, but they have low discharge coefficients, because only a part of the area uncovered by the valve is used.

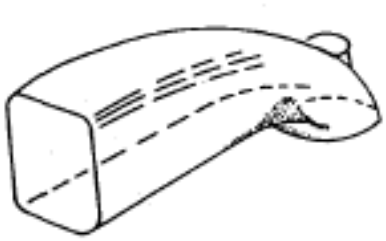

Figure 2-2 Directed Port.

An improvement is obtained with the use of the second approach. The swirl is generated within the inlet port: the flow enters in the cylinder than it is forced to rotate about valve axis. The flow distribution is forced around the circumference in non-uniform way, and the inlet flow has a significant net angular momentum about cylinder axis. An example consists of shallow ramp helical, Fig 2-3, for which an adequate level of swirl is obtained and a high discharge coefficient also for small intake valve lift is reached. Also it is possible to reach a higher volumetric efficiency [8].

Figure 2-3 Shallow ramp helical

In Diesel engine multi-valve, a combination of the two approaches directed and helical port is usually used to achieve a sufficient level of swirl for all engine operating conditions. Under low engine operating conditions, one of the two inlet port is cut with a valve. In this the flow is forced to pass through only one of the two intake valve. In addition it is possible to avoid and excess of swirl at high flowrate, which leads to excessive mixing between the air and the vapor fuel into the cylinder.

2.1.3 Organized motions in the cylinder: Tumble

The tumble is an organized rotational motion around the perpendicular axis to the cylinder axis. This motion begins during the intake process and it is amplified during the compression stroke. For this reason, the incoming flow is directed to the region below the exhaust valve due to the

presence of the intake valve, this approach generates the macrovortex with axis orthogonal to cylinder axis.

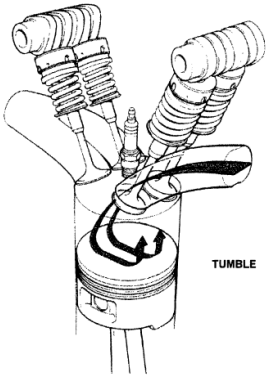

Figure 2-4 Tumble rappresentation [11]

When the vortex is crushed by the rise of the piston to the Top Dead Center, during the compression stroke, the macrovortex increases its speed to keep the angular momentum. The viscous stresses due to the higher velocity gradients cause the decay of the rotary motion organized in microvortexes. The major benefit of the tumble is to generate the turbolence near the end of the compression stroke, to accelerate and intensify the initial part of the combustion process [8]

2.1.4 Organized motions in the cylinder: Squish

Squish is directed radially inward during the end of the compression stroke when a portion of the piston face and cylinder head approach each other closely [8]. When the piston is close to the Top Dead Center, the gas flow is forced to back flow to the central area of bowl-in piston creating toroidal macrovortices around the walls of the combustion chamber.

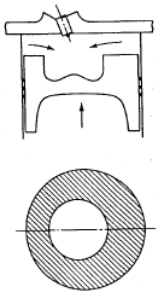

Figure 2-5 Squish rappresentation

Unlike the tumble and swirl motions, squish motions tend to arise towards the end of the compression stroke by intensifying charge turbulence near the combustion processes.

2.2 Turbolent motion in the cylinder

In the engine cylinder the flow processes are turbolent. In turbolent flows, the rate of transfer and mixing are many times greater than the rates, due to molecular diffusion. The turbolent diffusion represent the local fluctuations in the flow field which leads to increased rates of heat and mass and momentum transfer. From a physical point of view, the turbolent flow is always dissipative, because the fluid is subjected to the deformation work by the viscous shear stresses, increasing its internal energy at the expense of turbolent kinetic energy (tke). Therefore to generate turbolence, energy is required. In general, the characteristic of the turbolence is influenced by the enviroment, which is a combination of various factors in an engine. Shear layers, recirculating regions and boundary layers represent a complicated combination of this factors. The flow is unsteady and may submit important cycle-to-cycle fluctuations. Both small-scale and large-scale turbolent motions are significant factors governing the overall behavior of the flow [8]. The velocities fields generated in the engine cylinder are variable over time, in which the processes are periodic. For this reason, the flow into the cylinder is turbolent and unstable whose characteristics are not easy to quantify. A typical aspect of the turbolent flow is the irregularity and randomness which necessitate the use of statistical methods for their determination. The quantities normally used for every properties (in this case the velocity) are the mean velociy, the fluctuating velocity about the mean velocity for various time and length scales. In the engine, the flows pattern changes during the cycle, for this reason the application of these turbolence concepts is complicated. The mean flow can vary significantly from one engine cycle to the next. This means that the turbolent motion varies from one engine cycle to the next but there is also a marked variation of the characteristics of the mean flow, because the behaviours of the flow are unstable and not strictly periodic in the engine. One of the approach used is the phase-averaging or ensemble-averaging, which provide the advantage of summarizing information on many measurements necessary to define the average engine characteristics thanks also to the use of doppler laser techniques or anemometric probes. These approaches are not discussed in this thesis. Finally, there are several length scales influencing different aspects of the flow behaviour in turbolent flows. In particular, the largest eddies in the flow are limited in size by the system boundaries while the smallest eddies of turbolent motion are influenced by molecular diffusion [8].

2.3 Overall Spray Structure

The fuel is introduced into the combustion chamber through one or more orifices and nozzle, exploiting the large pressure differential between the fuel supply line and the cylinder. Different designs of the nozzles are used depending on the required combustion system. From the Fig.2-6, it is possible to observe a schematic of the spray structure in Diesel Engine Direct Injection. When the liquid fuel jet leaves the nozzle, it becomes turbolent subsequently entering the combustion chamber, spreads out and mixes with the surrounding air. The initial liquid jet velocity is greater than 10^2 m/s and the external surface breaks up into drops of order 10 μm , close to the nozzle exit. The liquid column leaving the nozzle, disintegrates inside the cylinder over a characteristic length, called “Break up Length” forming drops of different sizes. Moving away from the nozzle hole exit, the air mass increases within the spray, then the spray diverging and increasing its width, the air mass decreases its velocity. As the air entrainment proceeds into the

fuel, the fuel drops evaporate and the tip of the spray penetrates utleriorly into the combustion chamber as injection proceeds, but a decreasing rate [8].

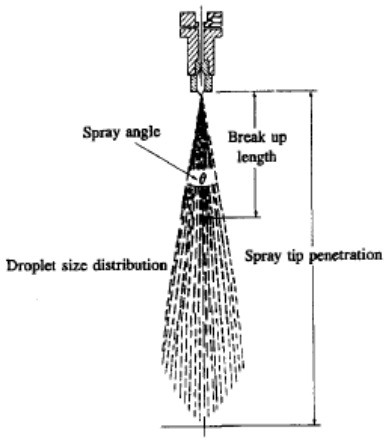

Figure 2-6 Schematic of diesel fuel spray *[8]*

The penetration process of the diesel spray into the combustion chamber can be analyzed experimentally by photographic tecniques. In this way, the Tokyo Institute of technology conducted experimental tests using rapid compression machine which simulates diesel conditions. From Fig. 2-7, it is possibile to show the photograph of the diesel spray injected into quiescent air in rapid compression machine.

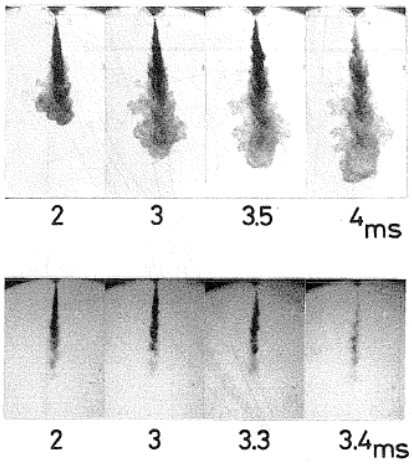

Figure 2-7 Evaporating diesel spray in quiescent chamber taken by the shadowgraph and back-lighting tecniques [12]

In this case, two different tecniques are used [12]:

- Back lighting used to distinguish the liquid containing core of the jet.
- Shadowgraph used to distinguish the extent of fuel vapor region of the spray which surrounds the liquid core.

The start of injection is in millisecond, until injection cases at 3.3 ms and 3.5 ms, the region of the jet close to the nozzle contains liquid drops and ligaments while most of the spray region contain vapor cloud contains liquid fuel around the liquid core [8]. The droplets on the outer surface of the spray evaporate to create a fuel vapor-air mix that covers the liquid-containing core. The equivalent ratio reaches the maximum values on the centerline of the jet while values close to zero are reached at the spray boundary. Starting from the penetration of the spray diesel into the outer regions of the combustion chamber, it interacts with the chamber walls and the spray is then forced to flow tangentially along the wall. In addition the sprays from multihole nozzles can interact with each other [12]. However the system combustion usually uses air swirl to increase fuel-air mixing rate. In this case, the spray pattern is totally different from the previous case for which a diesel spray is injected into a quiescent air environment.

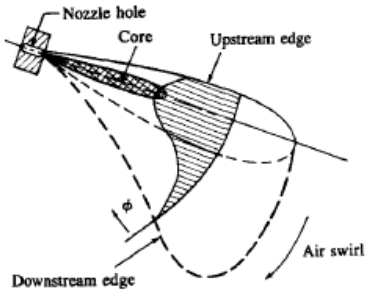

Figure 2-8 Schematic of fuel spray injected radially outward from the chamber axis into swirling air flow [8]

A schematic of the fuel spray injected radially outward from the chamber axis into swirling air flow is shown in Fig. 2-8. The structure of the jet is more complex beacuse there is relative motion in both radial and tangential directions between the air and the initial jet. After the spray entering the combustion chamber, it slows down and becomes even more bent toward the swirl direction, due to the penetration of the air into the spray. If there is swirl, the result will be that the penetration of the spray will be reduced more with respect to the case without swirl. The major benefit is the large vapor containing region downstream of the liquid-containing core [13]. Refering to the Fig. 2-9 it is possible to show that the jet starts to break up into a conical spray, immediately after leaving the nozzle hole.

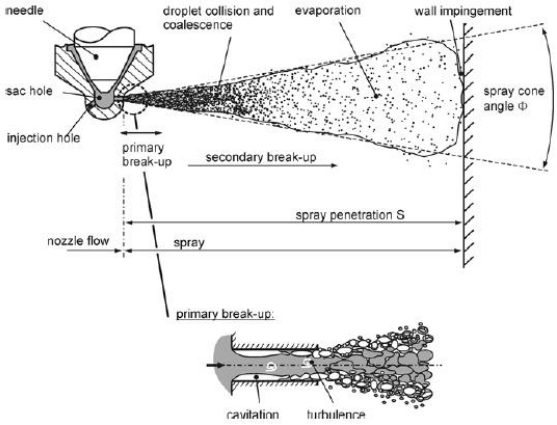

Figure 2-9 Schematic of diesel fuel spray

This first break-up of the liquid is called primary break-up and results in droplets and large ligaments that form the dense spray near the nozzle. In high-pressure injection, the main break-up mechanisms are cavitation and turbulence, which are generated inside the injection holes. The successive break-up processes are called the secondary break-up and are due to aerodynamic forces which decelerate the droplets. This phenomenon is caused by the relative velocity between droplets and surrounding gas. Near the spray tip, the drops are subjected to the strongest drag force and then are decelerated. In this way the droplets at the spray tip are continually replaced by new ones, so the spray penetration increases. It is also important to consider the droplet collision which may cause the size and velocity variations of the droplets. In fact from the Fig.2-9, a conical full-one spray is forming and most of the liquid mass is concentrated near the spray axis, while the external spray regions contain more fuel vapor and less liquid mass. In the dense region of the spray the probability of droplet collisions is high, becasue the droplet has a higher velocity at the spray axis and lower velocity in the radial direction due to interaction with the gas surrounding. However, droplets are not only prone to breakup process, but may combine with other droplet to form larger drops, which is known as coalescence [14]. To understand the impact of the injected diesel spray behavior on the combustion process it is necessary to analyze the processes that influence the air-fuel mixing, and so the time required to achieve the point of autoignition. These processes are atomization and evaporation.

2.3.1 Atomization Process

The liquid jet is transformed into fuel vapor so that it can mix with the air. This transformation takes place through the breakup process of the liquid fuel column. The atomization process is basically one in which bulk liquid is converted into small drops. The process is governed by the physical characteristics of the fuel and the aerodynamic interaction with the surrounding air that tends to disintegrate the jet itself. The surface tension tends to keep the liquid in its spherical form and the liquid viscosity of the liquid exerts a stabilizing influence by opposing any change in sistem geometry. The aerodynamic forces promote the disruption process by applying an external distorting force to the outer surface of the liquid. When the magnitude of the disruptive force exceeds the consolidating surface tension force, the breakup process takes place. Many of the

larger droplets produced by the initial disintegration process are unstable and undergo further fragmentation into smaller droplets. Thus the final range of the size of the drops produced in a spray depends not only on those produced by the primary break-up but also on the further breaking of the first drops through the secondary break-up. The action of the aerodynamic forces acting on the liquid drops involves the deformation of the same in different ways. Hinze conceived three characteristic types of deformation [15]:

- In lenticular deformation, the drop is flattened to form an oblate ellipsoid. The subsequent deformations to which it is subjected are due to the intensity of internal forces. It is assumed that the ellipsoid is converging in a toroidal form, disintegrating into small drops.
- In cigar-shaped deformation, the initial drop becomes elongated to form a ligament or long cylindrical thread that breaks up into small drops.
- In bulgy deformation, the parent drop subjected to the action of local deformation which causes the formation of bulges and protuberances on the outer surface of the drop, causing the break of the parent drop in smaller drops.

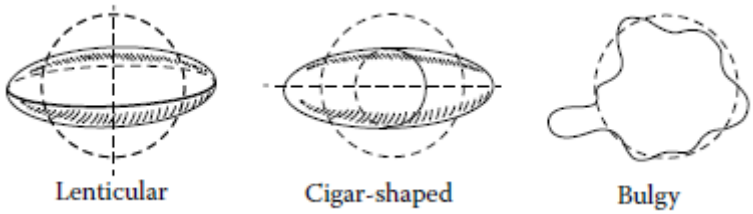

Figure 2-10 Basic types of globule deformation [15]

In general, the type of deformation and breakup listed above, depends on the physical properties of the liquid and gas, as density, viscosity, interfacial tension, and the behaviour of the flow around the drop. The mode of drop disintegration depends on whether the drop is subjected to steady acceleration or if it suddenly interacts with a flow at high velocity. With steady acceleration the drop becomes progressively flattened, and at a critical relative velocity it is popped out into the form of a hollow bag attached to an almost circular rim. In terms of disintegration, the bag produces a multitude of very fine drops, while the rim, which contains even 70% of the mass of the original drop, breaks up into larger drops. If the drop is subjected to an interaction with the fast airstream, it disintegrates differently. As opposed to being blow out into a thin vacuum bag anchored to a rim, in this case the drop is deformed in opposite direction and following the interaction with the airstream, it has a convex surface. The drop first takes a saucer-shape, which then takes the form of thin filaments which break in drops [15]

The initial condition for breakup is achieved when the aerodynamic drag force is equal to the surface tension:

$$C_D \frac{\pi D^2}{4} 0.5 \rho_A U_r^2 = \pi D \sigma \qquad (2.1)$$

Where:

- C_D, drag coefficient
- D, droplet diameter
- σ, liquid surface tension
- ρ_A, air density
- U_r, relative velocity between air and flow

$$\left(\frac{D\rho_A U_r^2}{\sigma}\right)_{crit} = \frac{8}{C_D} \tag{2.2}$$

Rearranging these terms, in dimentionless group:

The first term, in the eq. 2.2, is the Weber Number, We_g, which represents the ratio between the aerodynamic force and the force of cohesion due to the surface tension [15]. For $We_g < 12$, the drops become intact [9]. The fuel jet normally forms a cone-shaped spray at the nozzle exit, under diesel engine injection conditions. This type of behavior is classified as the atomization breakup regime which produces droplets with sizes very much less than the indicated nozzle hole exit diameter. This behavior is different from other types of liquid jet breakup. A first breakup method is called first-induced breakup regime. In this approach, the breakup is due to the unstable growth of surface waves caused by the surface tension and it results in droplet larger than the jet diameter. As the jet velocity increases, the forces due to the relative motion of the jet and the surrounding air increase the surface tension and the droplets reach the size of the order of the jet. A subsequent increase in jet velocity results in breakup characterized by divergence of the jet spray after an intact length downstream of the nozzle. Subsequently the second wind-induced breakup regime takes place where the unstable growth of short-wavelength waves induced by the relative motion between the surrounding air and the liquid produces whose sizes is much less than the jet diameter. Further increases in jet velocity leads to breakup in the atomization process, where the breakup of the outer surface of the jet takes places at, or before, the nozzle exits plane and results in droplets whose size diameter is much smaller than the nozzle hole diameter. The aerodynamic interactions at the liquid/gas interface appear to be one major factor of the atomization process in this regime [8]. To reduce the time required by the evaporation process, the surface of the jet should be increased as much as possible by pulverising it into small droplets, because the surface of the same depends on the heat flow that the drop can receive from the surrounding air at high temperature. Droplets, bubbles, and particles into the spray occur with a certain size distribution. For this reason, it is useful to characterize the level of atomization through

an average diameter, called Sauter mean diameter, SMD. In literature, the SMD is known as the surface-volume mean diameter and is defined from the following equation [16]:

$$SMD = \frac{\sum N_i d_i^3}{\sum N_i d_i^2} \tag{2.3}$$

Where:

- N_i, numbers of droplets
- d_i, diameter droplet

The Sauter mean diameter expresses the mean diameter of poly-dispersed droplets by taking account the volume-to-surface area ratio and must have a physical meaning [16].The SMD is one of the most important parameter used to characterise the efficiency of the atomization process. The droplet size varies in time and space: for the same spray, the breakup process will be developed depending on the distance from the nozzle hole exit. Statistically at 18.5mm distance from the nozzle hole exit the average diameter of the drops is 90 μm while further away from the injector hole at 74.5 mm the average diameter of the drops is less than and equal to 50 μm

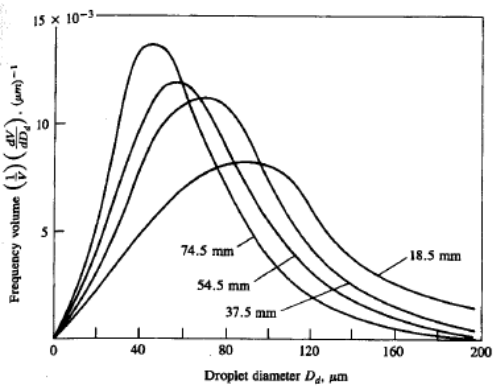

Figure 2-11 Droplet size distribution [8]

The Sauter Mean Diameter decreas or improves the atomization process when [8]:

- The nozzle diameter or the diameter of the initial droplet decreases. In this way, this nozzle hole diameter is subject to technological limit ($d_{nozzle} \approx 0.1\, mm$) due to the formation of carbon deposits (cooking)
- The injection pressure and the jet velocity increas: the aerodynamic processes that lead to breakup jet increases. From the Fig 2-13, it is possible to observe that beyond a certain level of injection pressure the average size of the droplet tends to stabilize. Because a certain number of Weber has been reached and a further increase of the injection pressure does not affect especially on the breakup process

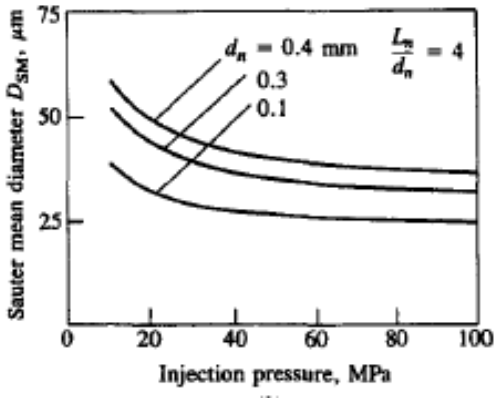

Figure 2-12 Effect of nozzle diameter and injection pressure [8]

- The liquid viscosity which opposes the sliding of fluid threads and the liquid suface tension which opposes changes in the shape of the drop compared to the spherical shape decrease.

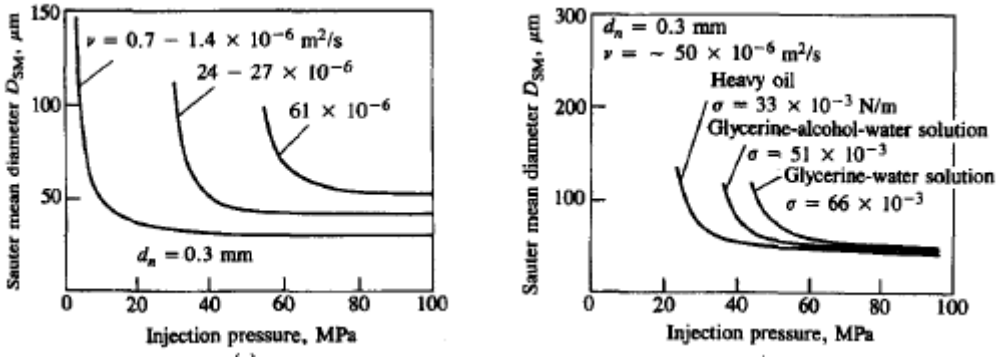

Figure 2-13 Effect of liquid viscosity and liquid surface tension [8]

- The surrounding air density increases favoring the breakup process.

2.3.2 Spray Evaporation

The liquid fuel injected into the combustion chamber is atomized in small drops near the nozzle outlet, forming the spray, which will have to evaporate before mixing with air and then burn. In the Fig. 2-7, the basic structure of an evaporiting diesel spray, under conditions typical of a large-direct injection engine, is shown. Thanks to the back illumination tecniques, cited above, it is possible to observe the presence of a liquid core, which exists along the axis of the spray where the drops are sufficiently dense to mitigate the light beam. Until the injection phase is finished, the core length remains costant. The core is surrounded by a region with a high rate of spray vapor, which continues to penetrate more and more inside the combustion chamber. The core extends only partly to the spray tip. Looking at the evaporation process in more detail, it is possible to consider a liquid drop that will start from an environment at ambient temperature and reach,

through the injection phase, an environment with air at typical end of compression engine conditions. In this way, three phenomena will determinate the history of the drop [8]:

- Deceleration of the drop due to aerodynamic drag
- Heat transfer to the drop from high temperature air
- Mass transfer of vaporized fuel away from the droplets

As the drop temperature increases, due to the heat transfer to the drop from high temperature air, the fuel vapor pressure increases so the evaporation rate increases. As the drop velocity decrease, the convective heat-transfer coefficient between the drop and the air decreases, which is dependent from the droplet velocity. The combination of these factors gives the behavior shown in Fig. 2-15 where temperature, drop mass, velocity, heat transfer rate from the air and vaporization rate are shown as a function of time following injection [8]:

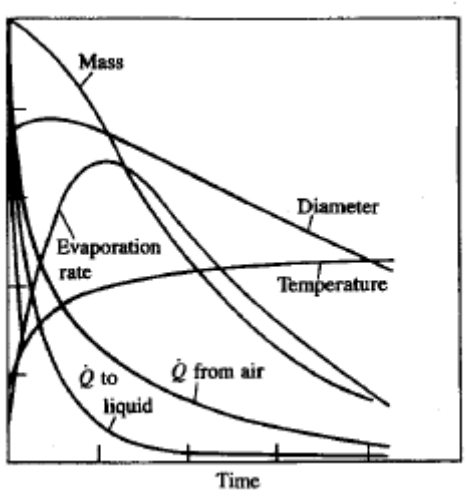

Figure 2-14 Evaporation process of an individual drop in diesel environment at the time of injection [8]

From the analysis of individual fuel drops 25 μm in diameter injected into air environment at typical diesel conditions have highlighted that the time required to evaporate the drop is usually less than 1 ms. In the spray core, the evaporation process has an important effect on the fuel-vapor concentration in the air within the spray and the temperature, because in this region of the spray the number of droplets is high. As fuel vaporizes, the local fuel vapor pressure will increase while the local air temperature will decrease. To precisely quantify the fuel vaporization rate within a diesel fuel spray it is necessary to have recourse to the solution of the coupled conservation equations for the liquid droplets and the air within the combustion chamber. For this purpose, several phenomenological models and Computational Fluid Dynamic models have been proposed, the analysis of which will not be discussed in this thesis work. However, the results obtained from these models showed that 70 to 95 percent of the injected fuel is in the vapor phase at the start of combustion under normal diesel engine conditions. But only 10 to 35 percent of the vaporized fuel has mixed within flammability limits in a typical medium-speed direct injection diesel engine [8].

2.4 Combustion Process

From the Fig. 2-16, it is possible to observe the typical data for pressure cylinder (p), fuel-injector needle-lift and fuel pressure in the nozzle gallery in functions of crank angle θ through the compression and expansion strokes of a small direct-injection diesel engine [8]:

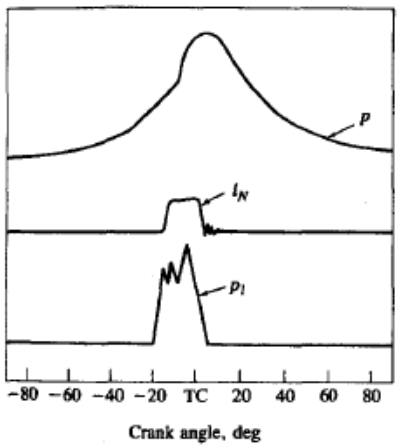

Figure 2-15 Cylinder Pressure, injector needle-lift and injection-system fuel-line [8]

The injection takes place through a four-hole nozzle into a disc shaped bowl in the piston combustion chamber. In this case, there is a delay of 9 degrees between the start of injection and the start of combustion, this last is identified by the change in slope of the p(θ) curve. The pressure grows rapidly for a few degrees, then the growth is slower until it reaches the peak located about 5 degrees before the TDC a few degree and the injection continue after the start of combustion. In corrispondence of the same cylinder pressure data and the rate fuel of injection, a rate-of-heat-release diagram is shown in Fig. 217 [8].

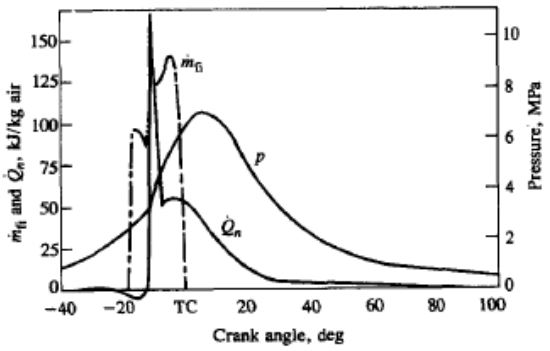

Figure 2-16 Net-heat release rate [8]

The general shape of the rate-of-heat-release curve is typical of this type of Direct injection engine over its speed range and load, which shows irrilevant heat release until toward the end of compression when a light loss of heat during the delay period [8]. In fact, the liquid fuel draws energy from the surrounding environment, subtracts heat to evaporate. At the end of the delay,

the heat-rate-release grows rapidly [9]. During the combustion process the burning proceeds in three different stages. In the first stage, the rate of burning is usually very high and has a duraction of only a few degrees, which corresponds to the period of rapid cylinder pressure. In the stage, the heat-release rate gradually decreases. About 80 percent of the total fuel energy is normally released in first two stages. The tail of the heat-release rate corresponds to the third stage, in which a small rate of heat release persists trough the expansion stroke. In this stage, the 20 percent of the total fuel energy is released [8]. Observing the pattern of the typical heat-rate-release diagram for Direct Injection diesel engine, fig. 2-18, it is possbile to identify four distinguishable phases [8]:

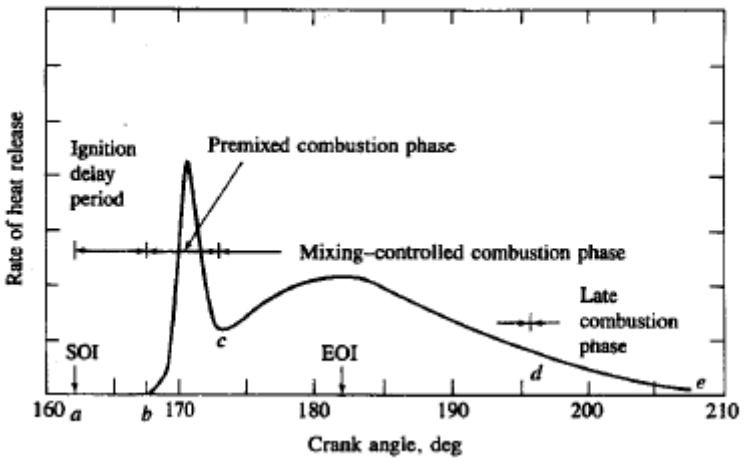

Figure 2-17 Typical DI engine heat-release diagram [8]

- Ignition delay (ab). The time between the start of hydraulic fuel injection and the start of combustion [8]
- Premixed Combustion phase (bc). Once the ignition delay of the first injected fuel core has been completed, the rise in temperature produced by the combustion of these fuel greatly accelerates the combustion process of the accumulated fuel, which burns simultaneously resulting in a sharp pressure gradient. This increase, although advantageous from the point of view of the thermodynamic efficiency, is responsible for the characteristic operating noise of the diesel engine [8]
- Mixing-controlled combustion phase (cd). Once the rapid combustion of the accumulated fuel is exhausted, the process is regulated by the speed with which new fractions of fuel are available to burn therefore by the speed with which the fuel injected can evaporate and spread in the air. This phase can be controlled by the injection rate check at differences from the previous phase [8]
- Late Combustion Phase (de). The injection has been completed but the chemical reactions are still proceeding, gradually running out. This phase is powered by turbolent motions that mix the gas into the combustion chamber; it is necessary do not prolong this phase much so as not to reduce the engine efficiency [8]

2.5 Direct-Injection Diesel Combustion: Conceptual model

To understand the experimental measurements and improve the development of numerical modelling, an accurate coneptual model of the Diesel combustion is described in this section. Diesel combustion is turbolent, it is composed by three dimensional, complex, multiphase process that occurs in high-pressure and high-temperature environment [17]. Thanks to studies conducted by John E. Dec at the Sandia National Lab, since the 90s, we can effectively answer the following question: "What happens to fuel injected into the combustion chamber?". The devolpment of advanced laser-based diagnostics provides a means to detailed in-situ measurements of the process occuring inside of a reacting diesel jet fuel. These diagnostics techniques allow specific species within the reacting jet to be measured at multiple points concurrently with high temporal and spatial resolution. From the fig. 2-19, it is possible to observe the schematic of optical-access diesel engine used by John E. Dec [17]:

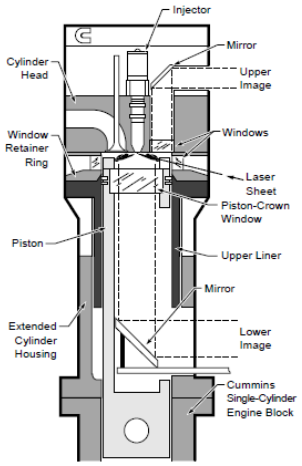

Figure 2-18 Schematic of optical-access diesel engine [17]

The optical-access diesel engine used in the [17] was a single cylinder, direct-injection and 4 - stroke diesel engine, which size-class was typical for Heavy-Duty applications. From the engine design, there are some constructive differences, in particular a window in the cylinder head offers a view of the squish region and the outer portion of the combustion bowl. Around the top of the cylinder wall, additional windows are located to offer orthogonal optical access, which is required for two-dimensional laser imaging diagnostics. These windows allow access to the laser sheet inside the cylinder, for example along the fuel axis. Finally, this engine incorporated a unique separating cylinder liner to rapid cleaning of the windows [18].

Fig. 2-20 represents a temporal sequence of schematic showing, which describe the devolpment of a diesel fuel jet from the start of injection to the premixed burn and the first part of the mixing-controlled burn. These schematics images represent idealized cross-sectional slices through the middle plane of the jet which show conceivably how DI diesel combustion occurs in the absence of swirl and wall interactions. These schematic images represent the base operating condition in the research diesel engine, and this is a distinctive operating condition for DI diesel combustion,

in any case for production engines the amount of intercooling and turbocharger boost and the injector characteristics can vary significantly, affecting both the spatial and temporal scaling [17].

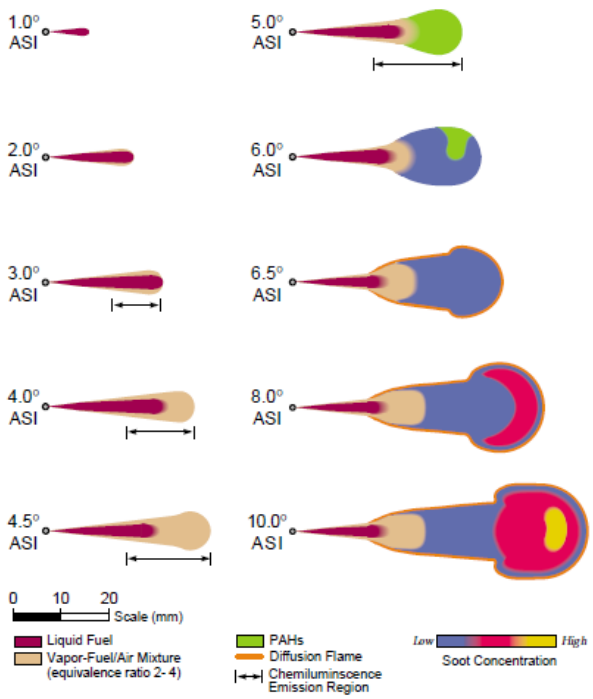

Figure 2-19 A temporal sequence of schematic DI Diesel combustion [17]

Each images are provided of the crank angle degree After Start of Injection, ASI and the color scheme is shown in the legend:

(0.0° - 4.5 °ASI) Initial Jet Development

The first three images in Fig. 2-19 show the jet penetration out to the point where all the liquid is vaporized. The dark purple region tagged as liquid fuel shows the maximum extent of the liquid fuel droplets. This region contains only liquid fuel at the injector while the air is entrained, and fuel vaporizes so these gases are present along with the liquid-fuel droplets at the downstream. As shown in the 1.0° ASI schematic, liquid fuel covers the cross section. For 2.0° ASI schematic a vapor-fuel region begins to develop along the sides of the jet in addition to the extent of the liquid droplets. The liquid reaches its maximum penetration of about 23 mm at 3.0° ASI. The entrainment of hot air into the jet allows its vaporization for all the fuel by this point. In the subsequent images, it is possible to observe how the gas phase continues to penetrate across the chamber, and a head vortex possibly develops. By 4.5° ASI, the jet continues its penetration into the chamber until it reached a distance of about 34 mm and whose main part contains a enough uniform fuel/air mixture with equivalence ratios variable from about 2 to 4 [17].

(3.0° - 5.0° ASI) Autoignition

The exact point where the ignition takes place is not well defined both from a spatial and temporal point of view. For 3.5° ASI, chemilluminescence occurs along the entire region downstream of the jet. At this time, vapor can barely penetrate through the liquid. From Fig. 2-20, it is possible to observe the chemilluminescent region of the jet indicated by the arrow. This region is shown from 3.0° ASI. Furthermore, it is not known whether chemilluminescence may occur at the surface or volumetrically in the vapour-fuel/air mixture region. At 3.0° and 3.5 ASI, the vapor layer is not very thick, but from 4.5° ASI most of the chemilluminescence is coming from the large fuel-vapor/air mixture region up to the starting portion of the region. In this region, autoignition is likely to occur volumetrically as denoted by chemilluminescence, also denotes the formation of volumetrically PAH in the region between 4.5°-and 5.0° ASI. followed by the formation of Soot between 5.0° and 6.0° ASI [17]

(4.0° - 6.5° ASI) Firtst Part of Premixed Burn Spike

From the Fig. 2-20, the heat release rate curve starts to rise at 4.0° ASI and then increases very greatly after 4.5° ASI. By 4.5° ASI the main portion of the jet is extremely chemiluminescent as indicated in the figure 2-19. The fuel breaks down starting from 5.0° ASI, and in the entire cross section of the main portion of the jet, where the equivalent ratio is variable from 2 to 4 large PAHs is forming. In addition this timing coincides with the rapid rise in the heat release rate, which indicates the premixed burn characterized by the combustion of this fuel-rich mixture. At 6.0° ASI, the cross-section of the fuel jet presents the formation of small particles of soot, due to premixed combustion rich in fuel. The soot is generated in the whole cross-section of the downstream region of the jet from 6.5° ASI [17].

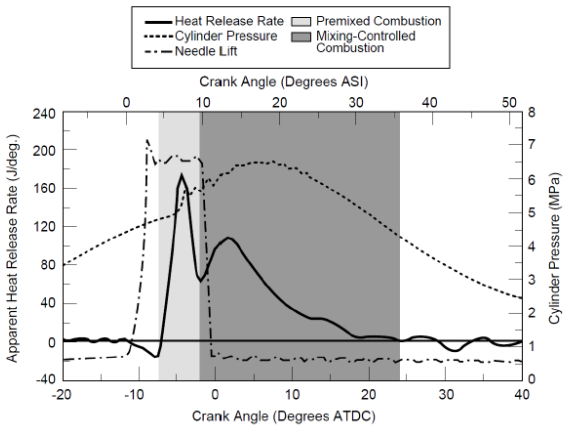

Figure 2-20 Cylinder Pressure, Apparent HRR, injector needle lift [17]

(5.5°-6.5° ASI) Onset of the Diffusion Flame

Between 5.5° ASI and 6.5° ASI, a diffusive flame is formed along the entire edge of the jet, due to the interaction between the surrounding air and especially the products of rich combustion within the jet. As shown in Fig. 2-19, the thin diffusive flame, highlighted in orange, surrounds the region downstream of the jet. Due to local heating by the flame there is a reduction in the length

of the liquid fuel from about 2 to 3 mm. In addition to 6.5° ASI, there is a growth of soot particles [17]

(7.0°- 9.0° ASI) Last Part of Premixed Burn Spike

During the completion of premixed combustion, the jet continues to grow and penetrate through the combustion chamber. The concentration of soot increases along the whole cross-section, with greater increase towards the front edge where the vortex of the head is forming, 8.0° ASI. The larger particles of soot, presumably due to turbulent mixing, are distributed inwards from the periphery for a few millimeters. In addition, a much larger soot particle region begins to form near the front edge with a distribution like that shown at 8.0° ASI. At the end of the premixed burn the small soot particles present throughout the cross section extend upstream to about 27 mm from the injector. In the vapor-fuel region downstream, the soot particles appear quickly enough across the entire cross section of the jet at this 27 mm location as shown in the 8.0° ASI [17].

(9.0° ASI to end of injection) First Part of the Mixing-Controlled Burn

The general appearance of the jet shows that the combustion process is purely controlled by mixing. At 10° ASI, the jet is further penetrated the chamber and the head vortex is developing effectively, in this region the concentration of large particles of soot is high. However, at about 27 mm downstream of the injector, the presence of soot is very marked across the entire cross-section, along the sides of the jet and precisely upstream of the head vortex the soot particles, generated in the diffusive flame, reside. These are larger than the soot particles located in the central region of the jet but smaller than the soot particles located in the region of the head vortex. This general aspect of the soot and jet is maintained until the end of the fuel injection, although the concentration and size of soot particles increase in the head vortex region [17]

Mixing-Controlled Combustion Phase

Looking at the Fig. 2-22, it is possible to show a schematic of the conceptual model of DI diesel combustion during the mixing-controlled phase [17].

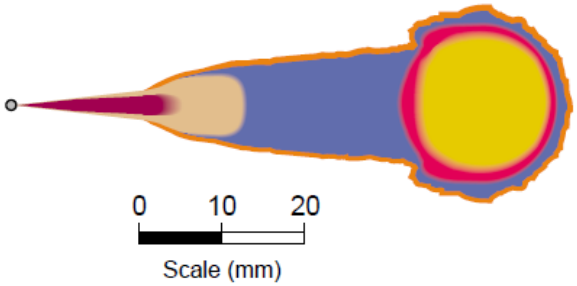

Figure 2-21 Schematic of the mixing-controlled burn in DI diesel combustion [17]

The schematic of mixing-controlled in Fig. 2-22 follows temporally the figure at 10° ASI and it represents the remaining part of the mixing-controlled phase before the end of injection. The schematic assumes a rather jagged behavior, this is due to the turbolent nature of the jet. Moving downstream of the injectore tip, the inlet air to the jet is sufficient to evaporate all fuel up to get at distance from the injector tip of about 18 or 19 mm. Downstream at this point, vapor fuel and inlet air formed a relatively uniform mixture for a short distance. About 27 mm from the injector tip, the soot appears in small particles across the whole cross section, also the largest concentration of large soot particles is concentrated downstream of the jet in the head vortex. At this point, about 27 mm from the injector tip, the soot accumulated in the center of the head vortex has time to grow, also reaching the edge of the jet can be oxidized by OH. From the schematic in Fig. 2-23, it is possible to show the thin layer of soot along the diffusive flame at upstream the main soot formation region. It is due to the local heating by the diffusion flame which promotes the pyrolysis of the fuel and the soot formation [17].

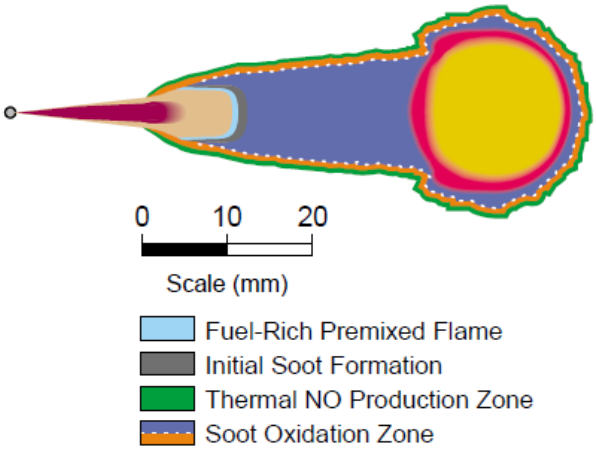

Figure 2-22 A schematic of conceptual model from fig. 2-22

As a result of the process described above, a light-blue color region appears in Fig 2-23. In this region there is a standing-fuel rich premixed flame, located upstream of the region where soot first appeared. In addition, this region is characterized by values of equivalent ratio varying between 2 and 4, downstream of the maximum liquid penetration. A region of this type is an ideal environment to produce soot, due to the high content of fuel, which are sufficiently hot for pyrolysis

and the formation of soot. Same behaviour as for the distribution of soot particles downstream and in the central jet region, which contains only small particles [17].

2.6 Pollutant formation mechanisms in DI diesel engine

In the diesel engine the pollutant formation processes are highly dependent on the fuel distribution and how that distribution changes with time due to mixing between vapor-fuel and the air. A qualitative assessment can be obtained from fig. 2-24, which illustrates the various parts of the fuel jet and the flame that are subject during the premixed and mixing-controlled phases of diesel combustion in a direct-injection engine with swirl to unburned hydrocarbons (HC), the formation of nitric oxide (NO), and soot (or particulates). Also due to the classic overall lean environment following a diesel combustion process the formation of carbon monoxide (CO) is not significant [8].

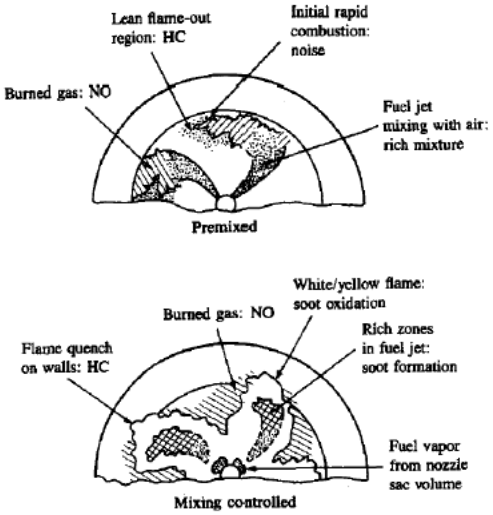

Figure 2-23 Summary of pollutant formation mechanisms in DI diesel engine [8]

Returning to the mixing-controlled burn phase, the Fig. 2-23 shows the region in which takes place the production and oxidation of soot and formation of NO. The initial formation of soot occurs in the gray zone or just downstream of the standing fuel-rich premixed flame in the products of rich combustion, which about 27 mm from the injector tip show the initial formation of soot. The Soot oxidation process takes place through the high concentration of OH radicals, particularly at the edge of the jet along the diffusive flame, which is the only region where oxygen can enter through the jet, as shown by the dashed white line in Fig. 2-23. The NO formation is expected along the periphery of the jet. Because in the diffusive flame region the two conditions necessary for the formation of NO_x are reached through the thermal mechanism: high temperature and sufficient oxygen concentration [17].

3 Computational Fluid Dynamics: Principles and Applications

3.1 Overview

The history of the Computational Fluid Dynamics starts from the early 1970s, at that time the acronym CFD described a combination of physical applications, numerical mathematics extended to computational sciences to simulate fluid flows. Early CFD methods simulated transonic flows based on solutions of nonlinear potential equation. Starting in the early 1980s, the increasing computational velocity achieved by supercomputers and the development of numerical techniques such as multigrid, made possible the resolution of the first two-dimensional (2-D) and three-dimensional (3-D) Eulero equations. In this way it was possible to simulate inviscid flows past complete aircraft or fluids inside turbomachines. In the mid-1980s, the focus shifted to viscous flow simulations governed by the Navier-Stokes equation, introducing a variety of turbolence models of varying levels of numerical complexity and accuracy. Among which the main models are represented by Direct Numerical Simulations (DNS) and Large Eddy Simulation (LES). With the advancement of numerical methods, since the 80s, were introduced models of real gas. Taking a step forward, up to the present day, CFD methodologies are normally used in many fields, such as automotive, turbomachines, naval, up to astrophysics, oceanography, and architecture. Important development has been achieved thanks to the high computing speed of today's supercomputers. For example, a wide range of viscous flow simulations can be performed with grids composed of dozens of millions of grid cells in a few hours [19]. The typical approach used in CFD analysis, requires the discretization of the fluid domain into the cell elements, to obtain a grid of calculation or mesh. Iterative resolution methods are applied for solutions of Navier-Stoks equations or Eulero equations. The following steps are used such as approach to the CFD calculations [20]:

- Definition of the characteristic geometry of the problem analyzed.
- Discretization of the volume occupied by the fluid, in terms of the generation of the calculation grid.
- Definition of the physical model and the numerical model.
- Definition of boundary conditions, or definition of fluid properties in the computing domain.
- Solving the equations iteratively, in this case the calculation is interrupted when the desired degree of accuracy has been reached.
- Visualization of the results through a post-processor.
- Analysis of the results

3.2 Governing equations

Fluid behavior is associated with the meaning of the term 'fluid dynamics', which is the investigation of interactive motions of many individual particles, in our case are represented by molecules or atoms. This characteristic implies that the density of a fluid is high enough to consider the fluid as a continuum. In this way a very small particle can contain enough particles, for which it is possible to specify the average velocity and the average kinetic nergy. At the end

we can define pressure, velocity, density, temperature, and other significant quantities for each point of the fluid. To determine the dynamic behavior of a fluid it is necessary to use the derivation of the principal equations of fluid dynamics, or the following conservation laws:

- The conservation of the mass
- The conservation of the momentum
- The conservation of the energy

The preservation of a certain flow quantity implies that one's total variation in an arbitrary volume is expressed as the net effect of the amount transported through the boundary, any sources, any internal and external forces acting on the volume. The amount of the quantity that crosses the boundary is called flux. This flux is decomposed in two contributions: the first is due to the convective transport and the second is due to the molecular motion present in the fluid at rest. The latter is influenced by the diffusive nature, which is proportional to the gradient of the quantity considered [19].

Depending on the flow model applied, governing equations can be obtained in different forms such as integral or partial differential, conservation, or non-conservation. In Fig. 3-1, it is possible to observe the roadamp for the derivation of these equations [21].

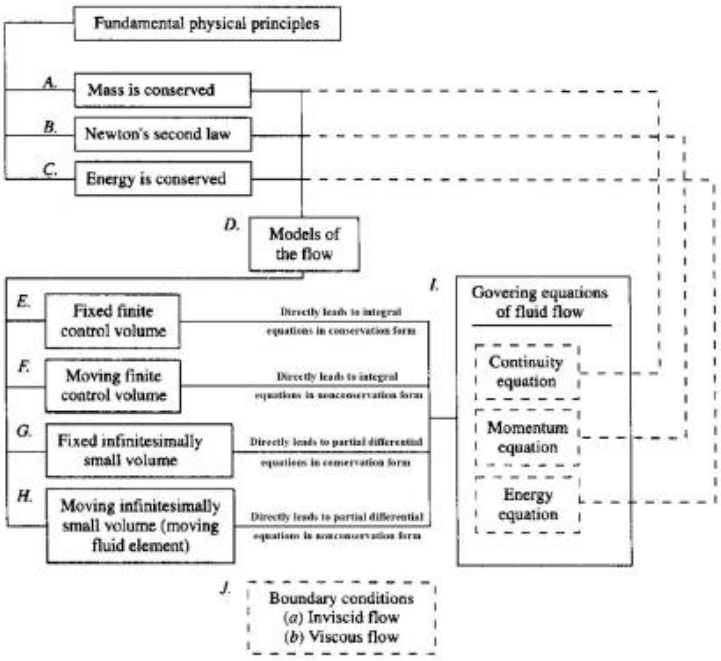

Figure 3-1 Road map for derivation of the governing equations [21]

3.2.1 Finite Control Volume

For a continuum fluid, it is necessary to construct one of the following model flow. The Conservation Laws express the concept of dividing the flow field into a few volumes where to concentrate fluid model behavior for each finite region. From the road map in Fig. 3-1, there are four different flow models, each of which is characterized by a different mathematical statement of governing equations.

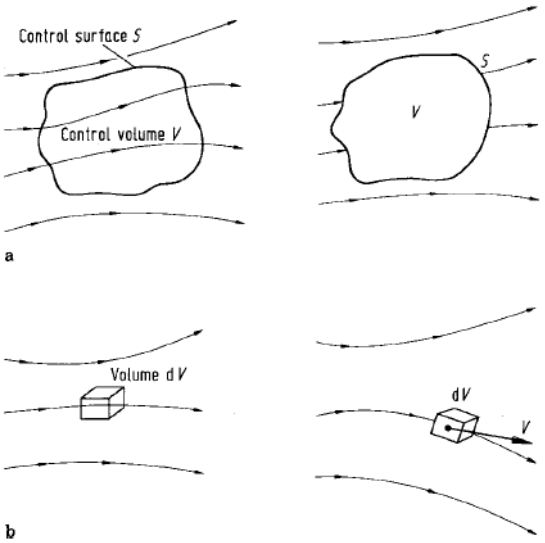

Figure 3-2 Finite control volume approach-Infinitesimal fluid element approach [22]

The general flow field is represented by the streamlines in Fig. 3-2(a), in which the closed volume within a finite region of the flow is called control volume, V, and its surface, control surface. The control volume can be fixed in space with the fluid moving inside it, as shown on the left of Fig. 3-2 (a). Another configuration is represented by the control volume that moves with the fluid, so that all the fluid particles throughout the volume are always inside the volume, as represented to the right of fig. 3-2 (a). In both cases the volume control must be large enough to consider a finite region of the flow. The fundamental physical principles are applied to the fluid inside the control volume and to the fluid that crosses the control surface. Fluid flow equations obtained from the application of fundamental physical principles are applied directly to finite control volume in integral form, which can be manipulated indirectly to obtain partial differential equations. These equations obtained from finite fixed volume control in space are integral or partial differential forms and are called the conservation form of governing equations. While the equations obtained in integral or partial differential form form for a control volum in motion with the fluid (right side of fig. 3-2 a) are called the non-conservation form of the governing equations [22].

3.2.2 Infinitesimal Fluid Element

Assuming a general flow field as represented by the streamlines in Fig. 3-2(b), we consider a very small fluid element, which is characterized by a differential volume, dV. The infinitesimal fluid element is characterized by a differential calculation and must be large enough to contain enough molecules, so as to be considered as a continuous medium. The fluid element can be considered fixed in space with the fluid moving inside it, as shown on the left of Fig. 3-2 (b) or it can move along the streamline with a velocity vector, V, equal to the flow velocity at each point. The fundamental equations related to the fundamental physical principles can be applied directly in partial differential equation form. Partial differential equations are obtained directly from the fixed fluid element in space are called the conservation forms of equations, while partial differential equations are obtained directly from the fluid element in motion, called the non-differential form of the equations of conservation (right side in Fig. 3-2 b) [22].

3.2.3 The Continuity Equation

The law of mass conservation expresses the condition that mass cannot be created and cannot disappear in a fluid system. In fluid at rest conditions, it does not take the diffusive flux contribution in continuity equations since a mass variation implies a displacement of the fluid particle. Considering the finite volume control model fixed in space, as shown in fig. 3-2, we derive the continuity equation. On the control surface, we consider a point characterized by flow velocity $\vec{v}$ the unit normal vector $\vec{n}$ and the elemental surface area, dS. In this case, the conserved quantity is the density ρ. The time rate of change of total mass inside the finite volume Ω, is expressed by the following equation [22]:

$$\frac{\partial}{\partial t}\int_{V} \rho d\Omega \tag{3.1}$$

The mass flow of fluid that crosses the surface fixed in space is equal to the product of the (density) x (surface area) x (velocity component to the surface), in this way it is possible to show the contribution from the convective flux accross each surface element dS [22]:

$$\rho\,(\vec{v}\cdot\vec{n})\,dS \tag{3.2}$$

From the convection for the $\vec{n}$ on each point of the control volume, we can state if the product $(\vec{v}\cdot\vec{n})$ is negative, we are considering inflow, if the product $(\vec{v}\cdot\vec{n})$ is positive we are talking about outflow because mass flow leaves the control volume. So we can write the equation into integral form of the continuity equation [22].

$$\frac{\partial}{\partial t}\int_{V} \rho d\Omega + \oint_{S} \rho(\vec{v}\cdot\vec{n})dS \tag{3.3}$$

This represents the conservation law of mass.

3.2.4 The Momentum Equation

The starting point of the derivation of the momentum equation is the Newton's second law which express that the variation of the momentum is caused by the net force acting on the mass element. Considering an infinitesimally small portion of the control volume, Ω [22]:

$$\rho\vec{v}d\Omega \tag{3.4}$$

The variation in time of the momentum into the control volume is equal to:

$$\frac{\partial}{\partial t}\int_{V} \rho\vec{v}d\Omega \tag{3.5}$$

In this case, the conserved quantity is product of the density times the velocity:

$$\rho\vec{v} = [\rho u, \rho v, \rho w]^T \tag{3.6}$$

The transfer of the momentum accross the boundary of the control volume, or the convective flux tensor, can be expressed through three components in the Cartesian coordinate system [22]:

$$\begin{matrix} x-component: \rho\vec{u} \\ y-component: \rho\vec{v} \\ z-component: \rho\vec{w} \end{matrix} \tag{3.7}$$

The contribution of the convective flux tensor to the the conservation of momentum is expressed by the following formula:

$$-\oint_{S} \rho\vec{v}(\vec{v}\cdot\vec{n})dS \tag{3.8}$$

Finally, we must introduce the forces acting on the fluid, which are divided into two types, depending on whether they act on the control volume [22]:

1. The forces act directly on the volume mass, for example gravitational forces, Coriolis or centrifugal forces.
2. The forces act directly on the surface of the control volume and are resulting from two sources:
    - The pressure distribution is imposed from the outside surroundind the volume.
    - The normal and shear stresses, resulting from the friction between the volume surface and the fluid.

The contribution of the body (external) force to the momentum conservation is expressed by [22]:

$$\int_V \rho \overrightarrow{f_e} d\Omega \tag{3.9}$$

Where - $\rho \overrightarrow{f_e}$, body force per unit volume

The surface sources $\bar{\bar{Q}}_s$ is composed by two terms [22]:

- Isotropic pressure component $-p\bar{\bar{I}}$
- Viscous stress tensor $\bar{\bar{\tau}}$

$$\bar{\bar{Q}}_s = -p\bar{\bar{I}} + \bar{\bar{\tau}} \tag{3.10}$$

The effect of the surface sources on the control volume is shown by the fig. 3-3.

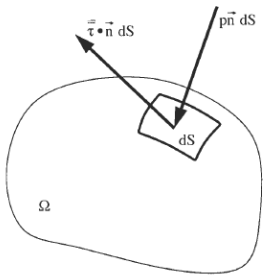

Figure 3-3 Surface forces acting on a surface element of the control volume [22]

In accordance with the general conservation law, summing all the above contributions we finally obtain the equation [22]:

$$\frac{\partial}{\partial t}\int_V \rho\vec{v}d\Omega + \oint_S \rho\vec{v}(\vec{v}\cdot\vec{n})dS = \int_V \rho\overrightarrow{f_e}d\Omega - \oint_S p\vec{n}dS + \oint_S (\bar{\bar{\tau}}\cdot\vec{n})dS \quad (3.11)$$

For the momentum conservation into an arbitrary control volume Ω, fixed in the space.

3.2.5 The Energy Equation

The derivation of the energy equation is related to the application of the First Law of Thermodynamics. Focusing on the flow model of a fixed volume control in space, Fig. 3-4, any variations in time of the total energy inside the control volume are equal to the sum of the heat transferred to the control volume and the rate of the work done on the control volume [19].

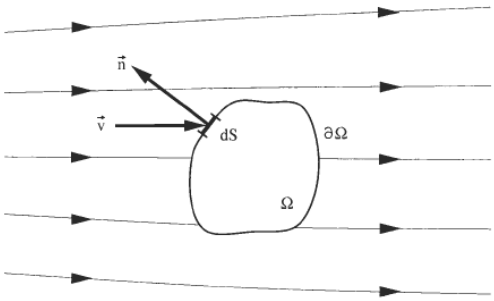

Figure 3 4 Definition of fixed control volume [19]

The total energy per unit mass of fluid, E, is the sum of the internal energy, e, represents the energy associated to each molecule and atom and to their sum, and the kinetic energy per unit mass, $\frac{|\vec{v}|^2}{2}$, thus we can write the following equation [19]:

$$E = e + \frac{|\vec{v}|^2}{2} = e + \frac{(u^2+v^2+w^2)}{2} \quad (3.12)$$

In this case, the conserved quantity is the total energy per unit volume, ρE, and its variation in time inside the volume, Ω, such as the following equation [19]:

$$\frac{\partial}{\partial t}\int_{V} \rho E d\Omega \tag{3.13}$$

For the derivation of the general conservation equation, we can specify the contribution of the convective flux [19]:

$$-\oint_{S} \rho E(\vec{v}\cdot\vec{n})dS \tag{3.14}$$

Unlike the continuity and momentum equation, in this case, we have the diffusive flux, which is proportional to the gradient of the conserved quantity per unit mass, in accordance with the Fick's law. The diffusive flux, $\vec{F}_D$, represents one of the terms that characterize the heat flux into the control volume, the diffusion of heat due to the molecular thermal conduction and the heat transfer due to the temperature gradient [19].

$$\vec{F}_D = -\gamma\rho k\nabla_e \tag{3.15}$$

Where $\gamma = \frac{c_p}{c_v}$ is the ratio of the specific heat, and k is the coefficient of thermal diffusivity. As described above, the equation 3.14 can be written as:

$$\vec{F}_D = -k\nabla T \tag{3.16}$$

With k is the thermal conductivity coefficient and T is the absolute static temperature of the fluid. In net heat flux within the finite volume control consists of other parts. The volumetric heating component due to absorption or emission of radiation or due to chemical reactions. In general, we can define the heat sources like the time rate of the heat transfer per unit mass $\dot{q}_h$, combined to the rate of work done by the body forces introduced previously in the equation of the momentum, $\vec{f}_e$ [19].

$$Q_v = \rho\vec{f}_e\cdot\vec{v} + \dot{q}_h \tag{3.17}$$

The last contribution to the conservation energy is the surface sources, Q_s, which are expressed by the time rate of work done by the pressure in addition to the shear and the normal stresses on the fluid element (fig. 3-3):

$$\vec{Q}_s = -p\vec{v} + \bar{\bar{\tau}} \cdot \vec{v} \tag{3.18}$$

From the classification of the contributions and terms, described above, we can obtain the expression for the energy conservation equation [19]:

$$\begin{aligned} &\frac{\partial}{\partial t}\int_V \rho E d\Omega + \oint_S \rho E(\vec{v}\cdot\vec{n})dS \\ &= \oint_S k(\nabla T\cdot\vec{n})dS + \int_V \left(\rho\vec{f_e}\cdot\vec{v} + \dot{q}_h\right)d\Omega \\ &- \oint_S p(\vec{v}\cdot\vec{n})dS + \oint_S (\bar{\bar{\tau}}\cdot\vec{v})\cdot\vec{n}dS \end{aligned} \tag{3.19}$$

Usually the energy equation (3.18) is written in the different form, considering the general relation between total enthalpy, total energy and pressure, as expressed by the following formula [19]:

$$H = h + \frac{|\vec{v}|^2}{2} = E + \frac{p}{\rho} \tag{3.20}$$

Expressing the term convective ($\rho E\vec{v}$) and pressure term ($p\vec{v}$) in the energy conservation law and applying it to the previous formula (3.19), we finally get the energy equation in the form [19]:

$$\begin{aligned} &\frac{\partial}{\partial t}\int_V \rho E d\Omega + \oint_S \rho H(\vec{v}\cdot\vec{n})dS \\ &= \oint_S k(\nabla T\cdot\vec{n})dS + \int_V \left(\rho\vec{f_e}\cdot\vec{v} + \dot{q}_h\right)d\Omega \\ &+ \oint_S (\bar{\bar{\tau}}\cdot\vec{v})\cdot\vec{n}dS \end{aligned} \tag{3.21}$$

3.2.6 Equation of State

Considering a compressible flow without external heat addition or body forces, we can use the continuity equation (3.3), the three momentum equations (3.10) and the energy equation (3.20). These five scalar equations contain seven unknowns p, ρ, e, T, u, v, w, so it is necessary to use two additional equations to close the system of equations, which are obtained from certain relationships that exist between the thermodynamics variables. These relations are known as

state equations. Choosing e and ρ as two independent variables, the form state equations are required [23]:

$$p = p(e, \rho) \qquad T = T(e, \rho) \tag{3.22}$$

For many dynamic gas problems, it is possible to assume a perfect gas. This is defined as a gas whose intermolecular forces are negligible, so the perfect gas equation of state is expressed as follows [23], where R is the gas costant:

:

$$p = \rho R T \tag{3.23}$$

3.3 Discretization Methods Approaches

After selecting the mathematical model, the next step is to choose a suitable discretization method, which is a method of approximation of differential equations to the algebraic equations system, the variables are defined in a set of discrete positions in space and time. There are various approaches to use, here are the most important ones: finite difference (FD), finite volume (FV) and finite element (FE) methods. Each mentioned methods returns the same solution if the grid is very fine [24]

3.3.1 Finite Difference Method

Introduced by Euler in the 18th century, this represents the oldest method for the numerical solution of PDE's, which for simple geometries represents the simplest method. The starting point is the conservation equation in differential form, the solution domain is composed of a grid, where for each point the differential equation is approximated by the substitution of partial derivatives by the approximation of nodal values of the functions. The result is an algebraic equation for grid nodes, in each of which the value of the variable and nearby nodes appears as an unknown. The FD method can be applied to any type of grid, although it has been associated with structured grids, in which this method is particularly simple and effective grids lines are used as local coordinate lines. Taylor series expansion or polynomial fitting can be used to obtain first- and second-derived approximations of variables against coordinates. The disadvantage of FD methods is that conservation is not enforced, even restrictions on simple geometries can be a disadvantage for complex flows [24]

3.3.2 Finite Volume Method

The starting point of the FV method is to use the integral form of conservation equations. The solution domain is divided into a finite and contiguous number of control volumes, where

conservation equations are applied to each control volume. The centroid of each CV has a computational node in which the variable values can be calculated. The interpolation method is used to express variable values at the CV surface in terms of nodal values. Surface intragrals and volume are approximated using formulae quadratures. The FV method can be applied to each type of grid and is also suitable for complex geometries. The grid only features the control volume boundaries and is not related to coordinate systems. The FV approach is the easiest to understand and program, however the disadvantage is that compared to FD schemes, the methods of order higher than second are more difficult to develop in 3D, this is due to the three levels of approximation required by FV methods: interpolation, differentiation adn integration [24].

3.3.3 Finite Element Method

The FE method is like the FV method, in this case the domain is defined by a set of finite elements or discrete volumes generally unstructured in 2D triangles or quadrilateral, in 3D are usually used tetrahedra or hexahedra. The characteristic of an FE method is that the equations are multiplied by a weight function before these have been integrated over the whole domain, then the solution is approximated by a linear shape function within each element to ensure the continuity of the solution through the element boundaries. In this way a function of this type can be construed by these values at the Corners of the elements. The approximation used is then replaced in the weighted integral of the conservation law and the equations are solved. The result is a set of non-linear algebraic equations. An important advantage of FE methods is to be able to adapt to arbitrary geometries, grids can be refined in a simple way and each element simply subdivided. It is also a method that is very easy to analyze mathematically, however the disadvantage is that linearized equations are not structured in the same way as regular grids, making it more difficult to search for an efficient solution methods [24]

3.4 Turbolence Modeling

3.4.1 Turbolent phenomenon

Turbolent phenomena are part of daily experience, such as:

- The smoke of a cigarette, which highlights the disordered flow of air that carries it.
- air flow on an obstacle or wing profile: turbulence in the boundary layer and generation of a turbulent wake; there is usually an increase in hydrodynamic resistance.
- Oceanic and atmospheric phenomena

Many engineering applications involve fluids in turbulent conditions. The first scientific note on turbulence to Leonardo Da Vinci, who studied the movement of water in the river streams used at the time for transport and as a source of energy [26].

The turbulence is a dynamic characteristic, in which the fluid is moving can become turbulent, a sperimantal evidence was proposed by Osborne Reynolds (1842-1912). Reynolds was the first

to distinguish the difference between a fluid flow in laminar motion and turbulent motion expressed by a fundamental parameter that describes the turbulent flow transition, known as the Reynolds number:

$$Re = \frac{\rho V L}{\mu} \tag{3.24}$$

Where:

- ρ – density of the fluid
- V-velocity of the fluid
- L- characterstics linear dimension
- μ-dynamic viscosity of the fluid

The distinction between laminar and turbulent pipe flow is dependent on this size. For example, considering a flow in a round pipe results in laminar motion if the Reynolds number is less than 2100, while if it is greater than about 4000, the flow is turbolent [27].

3.4.2 Energy Cascade of Turbolence

Analyzing the phenomenological theory underlying the turbulent flows it is necessary to introduce the definition proposed by Richardson (1922), who stated that turbulence consists of different eddies, located in the structure of the flow, the size of which may vary from large eddies made up of small eddies [28].

From Fig. 3-5, the modeling of a turbulent flow is described by the Energy Cascade theory of Kolmogorov, for which the smaller vortices created by the turbolents motions, absorb energy from the larger vortices. The energy transferred to the smaller vortices is dissipated until it reaches the last vortices, the energy is not conserved. In accordance with the Navier-Stokes equation, the phenomenon is described by the pressure force, which allows the fluid particle to move, and by a variable described by the viscosity which stops its motion [29]:

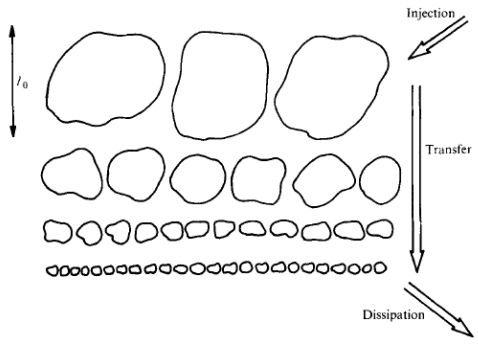

Figure 3-4 Tne energy cascade Kolmogorov Theory [29]

An important consequence of this process is that there is no trace of the possible orientation of the larger scales at the smaller scales [30]. The productions of the vortices are associated with the size, L, of the largest vortices, which varies up to the minimum scale l_0. This is the same order of magnitude as the thickness of the viscous substrate near the wall, or the same size as the smaller turbulent structures responsible for viscous dissipation. The cascade energy occurs when the size of the turbolent structure l, respect the condition: $L < l < l_0$, where the reciprocal of l is called Wave-Number. In accordance with Kolmogorov's theory, the energy contained in vortices vary with k, and it is expressed according to the following formula [30]:

$$E(k) = C_k \varepsilon^{2/3} k^{-5/3} \tag{3.25}$$

Where:

- Kolmogorov Costant, $C_k = 1.6 \pm 0.06$ [30]
- ε, turbolence dissipation rate
- k, wave-number

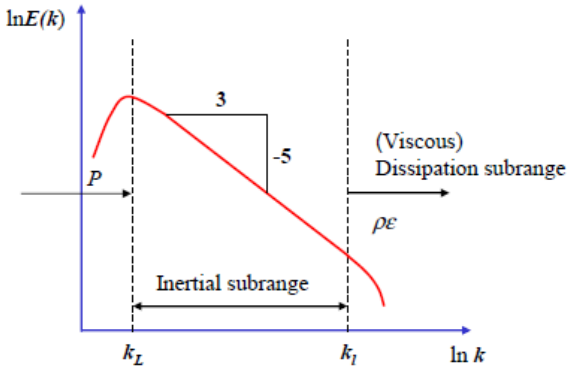

Figure 3-5 Inertial subrange [30]

The spectrum of the specific energy $E(k)$ is represented by the only inertial subrange, in which k values between $\frac{1}{L}$ and $\frac{1}{l_0}$

3.4.3 Turbolence Modeling: Overview

In the past various approaches are used for the experimental study of turbulent flows. The parameters used such as the time-averaged drag or heat transfer are relatively easy to measure but by increasing both the sophistication of engineering devices and the level of precision

required, the inevitable consequence has been an increase in the costs and difficulties of measuring. It is necessary to analyze the source of the undesirable effects, which require costly, long and sometimes impossible measurements. Therefore, numerical methods are a solution to this type of problem. The equation of Navier-Stokes, or the conservation equations in differential form can be solved numerically to predict the transition and evolution of the turbolence, which is usually refered to the Direct Numerical Simulation (DNS). This approach requires massive computational power, in fact all scales of turbolence from the smallest to largest must be accommoted. For this reason, this approach for most engineering applications is impratical. The number of grid points that can be used in a computation is limited by the memory of the machine and the processing speed. Only for geometrically simple domains and flows at relatively low Reynolds numbers, it is possible to use the DNS approach [24].

The second approach is the Large Eddies Simulation (LES) where large scale structure flows are directly simulated and filtering out the small-scales, which are calculated from turbulence models called subgrid scale models. The small-scale eddies are characterized by more uniform and common behaviours. In this way, the modeling approaches for small scale eddies appears more appropriate and avaible for over wide range of applications. Comparing this approach with DNS the small-scale modeling of turbulence implies that the grid spacing could be much larger than the Kolmogorov length scale, this allows to apply the LES method to higher Reynolds numbers. Therefore LES approach requires significantly less computational effort and is more applicable for practical purposes [24]

The third approach is called one-point-closure, which is expressed by a set of partial differential equations called the Reynolds-averaged-Navier-Stokes (RANS) equations. The introduction of approximations (turbolence model) is required because this approach do not form a closed set. From an engineering point of view, only some quantitative properties of a turbulent flow usually cause interest, such as the average forces on a body, the degree of mixing between two incoming fluid flows or the amount of a substance that reacted. Using previously described DNS or LES approaches, the calculation of these quantities is not practical, due to the high computational effort. Therefore these methods should only be used as an effective last resort, occasionally to check the validity of the RANS approach [24].

Finally, through Fig. 3-6, the schematic representation of the turbulent kinetic energy spectrum as a function of the wave-number k is shown again, which graphically exposes the application differences of the three numerical approaches described:

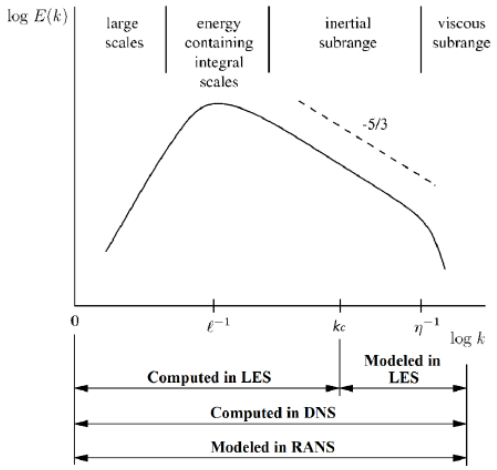

Figure 3-6 Turbulent kinetic energy spectrum as a function of the wavenumber k

3.4.4 Reynolds-Averaged Navier-Stokes (RANS) Equations

The approach of the Reynolds-averaged Navier-Stokes equations present as a starting point the Reynolds decomposition of the flux variables in an average and fluctuating component, where the insertion of the Reynolds decomposed variables in the Navier-Stokes equations (followed by an average of the equations) give rise to Reynolds stress tensor. Which is an unknown and needs to be modeled so that the RANS equations are solved. The problem of closure of the system of Navier-Stokes equations consists mainly in this operation. The flow of a viscous incompressible fluid with costant properties is ruled by the Navier-Stokes equations, applying the Einstein convention to the repeated Indices [31]:

$$\frac{\partial u_i}{\partial t} + \frac{\partial}{\partial x_j}\left(u_i u_j\right) = -\frac{\partial p}{\partial x_i} + v\frac{\partial^2 u_i}{\partial x_j \partial x_j} \tag{3.26}$$

$$\frac{\partial u_i}{\partial x_i} = 0 \tag{3.27}$$

Where u_i is the fluid velocity, p is the pressure divided by the density of the fluid and v is the fluid kinematic viscosity. In accordance with the concept of Reynolds decomposition, the dependent variables of the system are decomposed into mean and fluctuating parts, for the velocity u [31]:

$$u_i = \bar{u}_i + u_i' \tag{3.28}$$

Considering a generic flow variables, ϕ, its mean value can be calculated in a turbolent statistically steady state as a time average ($\overline{\phi}^T$), in a turbolent spatially homogeneous flow as a volume

average ($\bar{\phi}^V$). In a turbolent flow of more general nature the mean value can be calculated as an ensemble average [31]:

$$\bar{\phi}^E(x,t) = \lim_{N\to\infty} \frac{1}{N} \sum_{k=1}^{N} \phi^k(x,t) \tag{3.29}$$

Where N, is the number of repeated experiments.

In a turbolent statistically steady state and in a turbolent spatially homogeneous flow, it is assumed that [31]:

$$\bar{\phi}^T = \bar{\phi}^E \qquad \bar{\phi}^V = \bar{\phi}^E \tag{3.30}$$

By substituing the Eq. (3.27) into the Eqs (3.25) and (3.26), it is possible to obtain the system of partial differential equations that governs the mean-velocity and pressure fields of incompressible turbolent flow [31]:

$$\frac{\partial \bar{u}_i}{\partial t} + \frac{\partial}{\partial x_j}\left(\bar{u}_i \bar{u}_j\right) = -\frac{\partial \bar{p}}{\partial x_i} + v\frac{\partial^2 \bar{u}_i}{\partial x_j \partial x_j} \tag{3.31}$$

$$\frac{\partial \bar{u}_i}{\partial x_i} = 0 \tag{3.32}$$

The nonlinear term of the Eq. (3.30):

$$\overline{u_\iota u_J} = \overline{(\bar{u}_\iota + u'_\iota)\left(\bar{u}_J + u'_J\right)} = \overline{u_\iota u_J} + \overline{u'_\iota u'_J} \tag{3.33}$$

The RANS equations are obtained:

$$\frac{\partial \bar{u}_i}{\partial t} + \bar{u}_j \frac{\partial \bar{u}_i}{\partial x_j} = -\frac{\partial \bar{p}}{\partial x_i} + v\frac{\partial^2 \bar{u}_i}{\partial x_j \partial x_j} - \frac{\partial \tau_{ij}}{\partial x_j} \tag{3.34}$$

The last term at the right of the Eq. (3.33) is expressed in non-conservative form:

$$\tau_{ij} = \overline{u_\iota u_j} \tag{3.35}$$

The Eq.3.35 represents the Reynolds-stress tensor that incorporates the effects of turbolent motions on the mean stresses [31].

3.4.5 Turbolence Models

Several classes of RANS turbolence models exist, which we can list as follows [31]:

1. Zero-equation models. For this class, only a system of partial differential equations (PDEs) is solved for the the mean field, while no other PDEs are used. These models are called mean-velocity-field (MVF)
2. One-equation models. This class, compared to the previous class, involves an additional transport equation for the calculation of the turbolence velocity scale, which is usually expressed by the average turbolent kinetic energy, k
3. Two-equation models. This class, compared to the One-equation models, involves an additional transport equation for the calculation of the turbolence length scale, which is expressed in terms of the scalar dissipation rate of turbolent kinetic-energy ε. These models are also called: $k-\varepsilon$ or $k-\omega$ models
4. Stress-equation models. This class, compared to the Zero-equation models, involves an additional transport equation for the components of the Reynolds-stress tensor, τ_{ij}, and one for the scalar dissipation rate, ε. In fact, these modelas are also called: $\tau_{ij}-\varepsilon$ models.

One of the most widely used turbolence models are Two-equation models. These models are the simplest complet turbolence models. In fact, a significant advantage of these models is the ability to calculate not only the turbolent kinetic energy, k, but also turbolence length scale or equivalent. The best known is the $k-\varepsilon$ model

3.4.6 k-ε Turbolence Model

From the analysis of the RANS equation [32]:

$$\begin{aligned} &\frac{\partial(\rho U)}{\partial t} + \nabla\cdot(\rho UU) \\ &= -\nabla p + \nabla\cdot[\mu(\nabla U + \nabla U^T)] + \rho g \\ &-\nabla\left(\frac{2}{3}\mu(\nabla\cdot U)\right) - \nabla(\overline{\rho U'U'}) \end{aligned} \tag{3.36}$$

The Reynolds Stress (the last term at the right of the Eq. 3.35) needs to be modelled to close the RANS equations. The most common approach is the Boussinesq hypothesis (1872) [32]:

$$-\overline{\rho U'U'} = \mu_T(\nabla U + \nabla U^T) - \frac{2}{3}\rho k I - \frac{2}{3}(\nabla \cdot U)I \quad (3.37)$$

The Reynolds Stress can be described by the Eq. 3.36, in which the term μ_T needs to be calculated to close the equation, it is called eddy viscosity. Older models used a mixing length approach, l_m, to calculate the eddy viscosity. From a physical point of view, the mixing length represents the indicative size for the eddies containing in a fluid flow [32]:

$$\mu_T = \rho k^{1/2} l_m \quad (3.38)$$

The early eddy viscosity is algebrically expressed by the Eq. 3.37, it is possible to observe that this term only depends on the distance to the nearest wall. The transport equation for turbolence quantities can be solved to improve this model. In this way, it is necessary to the transport equation for the turbolent kinetic energy, k, and for the turbolence dissipation rate, ε. From the solution of the latter transport equation for ε [32]:

$$\mu_T = C_\mu \frac{\rho k^2}{\varepsilon} \quad (3.39)$$

We can use the Eq. 3.38, to compute eddy viscosity, μ_T, and replace it in the RANS equation. In this way, it is possible to close the system of RANS equations. Replacing the Eq. 3.38 into the Eq. 3.37, and combining them [32]:

$$l_m = \frac{C_\mu k^{3/2}}{\varepsilon} \quad (3.40)$$

The Eq. 3.40 shows that the mixing lenth, l_m is directly related to the turbolence dissipation rate and the turbolent kinetic energy. The transport equation for k is the same in the RNG (Re-Normalisation Group (RNG) methods by Yakhot et al to renormalise the Navier-Stokes equations, to account for the effects of smaller scales of motion) and standard $k - \varepsilon$ model (in which the eddy viscosity, μ_T, is determined by a single turbulence length scale, so the calculated turbulent diffusion is that which occurs only at the specified scale) [33]:

$$\begin{aligned} &\frac{\partial(\rho k)}{\partial t} + \nabla \cdot (\rho U k) \\ &= -\nabla p + \nabla \cdot \left[\left(\mu + \frac{\mu_t}{\sigma_k}\right)\nabla k\right] + \rho g \\ &- \nabla\left(\frac{2}{3}\mu(\nabla \cdot U)\right) + P_k + P_b - \rho\varepsilon + S_k \end{aligned} \tag{3.41}$$

Where:

- P_k is the production due to mean velocity shear
- P_b is the production due to buoyancy
- S_k is a user-defined source

The transport equation for the turbolence dissipation rate, ε, is:

$$\begin{aligned} &\frac{\partial(\rho\varepsilon)}{\partial t} + \nabla \cdot (\rho U \varepsilon) \\ &= -\nabla p + \nabla \cdot \left[\left(\mu + \frac{\mu_t}{\sigma_\varepsilon}\right)\nabla \varepsilon\right] \\ &+ C_1 \frac{\varepsilon}{k}(P_k + C_3 P_b) - C_2 \rho \frac{\varepsilon^2}{k} + S_\varepsilon \end{aligned} \tag{3.42}$$

The model coefficients C_1, C_2, C_3 vary between models. In this way the Launder & Sharma coefficients are the most up-to-date [30]:

Model	σ_k	σ_ε	C_1	C_2	C_μ
Launder & Sharma	1.0	1.3	1.44	1.92	0.09

Table 3-1 Launder & Sharma Model Costant

4 CONVERGE CFD Software

The Convergent Science is an innovative Computational Fluid Dynamics company, whose flagship product is CONVERGE CFD, which is a revolutionary software able to remove the grid generation bottleneck from the simulation process. The company was founded in 1997 by graduate students at the University of Wisconsin-Madison and was born initially as a CFD consulting company in the first years of activity. In 2008, the company transitioned to a CFD software company after that the first CONVERGE licenses were sold. [34]

Several areas of CONVERGE CFD applications includes thermal and hydraulic machines. For the simulation of internal combustion (IC) engine a high level of complexity is required due to the complexity of the geometry, spatially and temporally varying conditions and complex combustion chemistry in the engine. In this context, one of the biggest barriers in solving IC engine combustion is spending computational resources efficiently. In an IC engine case, the mesh resolution conditions are important to capture significative flow features variable in time and space. The solution to this problem is provided by the Adaptive Mesh Refinement. CONVERGE CFD automatically creates the mesh at runtime, dynamically adapts the mesh during the simulation and utilizes Adaptive Mesh Refinement to maximize both accuracy and computational efficiency. [35]

In addition CONVERGE Software contains a wide variety of modelling options for combustion, emissions and spray modellig which have been tested and verified for many applications.

4.1 Discretization Method

CONVERGE uses a finite volume approach to numerically solve the conservation equations, as described above in the section 3.3.2. The flow quantities are calculated and stored at cell centers depending on the summed fluxes through the cell faces. When an internal source term is present an example of this concept is shown in Fig. 4-1 [36].

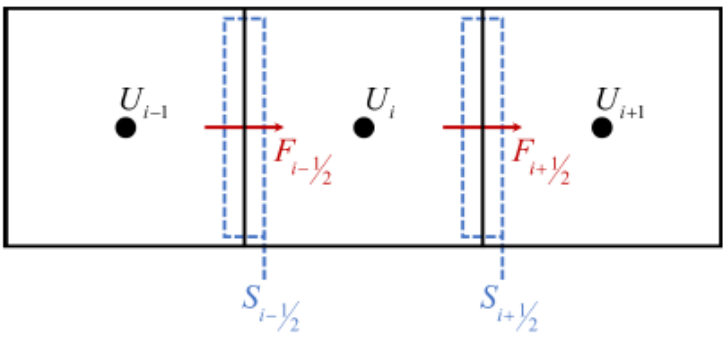

Figure 4-1 Sample three-cell, one-dimensional spatial domain

Considering the semplified quasi-1D case in Fig. 4-1, U_i is the vector representing the conserved variables for the cell i and $F_{i-1/2}$ is the flux vector on the $i-1/2$ face. To solve the integral form of the equation for a variable ϕ, the same variable must be interpolated to the cell surface. There

are wide options for obtaining the cell surface value. The first option is to average the two adiacent cell values and place them on the surface:

$$\phi_{i+1/2} = \frac{1}{2}\phi_i + \frac{1}{2}\phi_{i+1} \quad (4.1)$$

And

$$\phi_{i-1/2} = \frac{1}{2}\phi_i + \frac{1}{2}\phi_{i-1} \quad (4.2)$$

Another option is to upwind the surface value for ϕ:

$$\phi_{i+1/2} = \phi_i \quad (4.3)$$

And

$$\phi_{i-1/2} = \phi_{i-1} \quad (4.4)$$

4.2 Solution Procedure

To appropriately configure the simulation parameters, it is important to understand the order in which the transport equations are solved. From the Fig. 4-2:

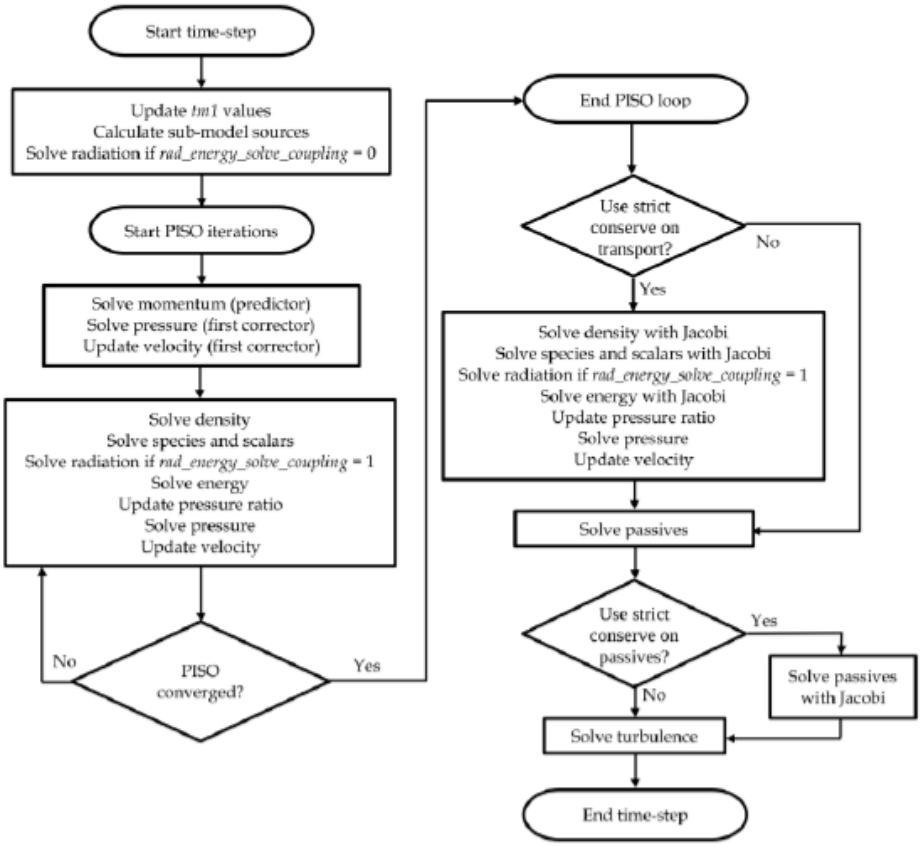

Figure 4-2 Solution order of the transport equations

At the start of each time-step, the previous values (*tm1* in Fig. 4-2, which is the time-step minus 1) are stored for all transported quantities. The explicit sources are subsequently calculated for each submodel that is currently activated and radiation is solved if the energy and radiation are decoupled. In the initial steps of the PISO loop, CONVERGE solves for momentum and pressure, which establishes the velocity for the other transport equations. It is necessary to check for PISO loop convergence, after each PISO iteration. For compressible case the software considers the PISO loop to be converged if [36]:

$$\Delta\rho < piso\_tol \tag{4.5}$$

Where $\Delta\rho$ is the density correction error.

While for incompressible cases, CONVERGE considers the PISO loop to be converged if:

$$\Delta P < piso\_tol \tag{4.6}$$

It is important to note that if the PISO iteration has converged but the PISO iteration number is less than *piso_itmin* the result will be that the PISO iterations continue as long as the minimum number of PISO iterations has been exceeded. Otherwise CONVERGE executes an additional PISO iteration. Moreover CONVERGE may perform an additional Jacobi iteration after the PISO loop has ended. The Jacopi iteration ensures that the quantity is conserved to machine zero rather than to the tolerance set by *piso_tol* [36]

4.2.1 The PISO Algorithm

The pressure-velocity coupling in CONVERGE is obtained using a modified Pressure Implicit with Splitting of Operator (PISO).

This method was introduced by R.I. Issa in (1986), who definied it as a non-iterative method for handling the pressure-velocity coupling of the implicitly discretised fluid flow equations. The PISO Algorithm utilises the splitting of operations in the solution of the discretized momentum and pressure equations, in this way the fields obtained at each time-step are close approximations of the exact solution of the difference equations. It is a predictor-corrector methodology which is generalised to the treatment of the coupling between the other transport equations [37]

The PISO Algorithm in CONVERGE starts with a predictor step where the momentum equation is solved. A pressure equation is subsequently derived and solved. This process leads to a correction and it is applied to the momentum equation. The process of correcting the momentum equation and re-solving can be repeated until the desired accuracy is reached. Only after completion of the momentum predictor and first corrector step, the other transport equations are solved in series. The PISO method can be used for solving either compressible or incompressible flows with only minor variations. The predictor- corrector process allows for a semi-implicit treatment of sources and sinks and can be updated at each corrector step. Another advantage is that the hyperbolic nature of the transport equations is respected and the use of the elliptic nature of the pressure equation leads to an improvement into the communication of information through the domain. For these reasons, the PISO method was chosen for use in CONVERGE. [36]

4.2.2 CFL Number

The Courant-Friedrichs-Lewy numbes plays an important role in Computational Fluid Dynamics and it is a necessary condition for convergence while solving certain partial differential equations numerically. The CFL numbers can estimate the number of cells through which the related quantity will move in single time-step, in particular a higher CFL number generally leads to a less computationally expensive simulation. The speed of sound CFL number, the diffusive CFL number and the convective CFL number are given respectively as [36]:

$$cfl_{mach} = c\frac{\Delta t}{\Delta x} \tag{4.7}$$

$$cfl_v = v\frac{\Delta t}{\Delta x^2} \tag{4.8}$$

And

$$cfl_u = u\frac{\Delta t}{\Delta x} \tag{4.9}$$

Where Δt is the time-step, Δx si the grid spacing, u is the cell velocity, c is the speed of sound and v is the viscosity. In CONVERGE each CFL number can be a fixed value or can very temporally

4.3 Mesh Generation

The CONVERGE Software discretizes the domain into control volumes called cells or nodes. A node is defined by its center and the faces that bound the node. To define the domain(s) of the mesh, CONVERGE uses internal data structure, assign an order to nodes and the faces of the nodes and establish connectivity between nodes. The software has an innovative approach to grid generation, which automatically generates the grid at runtime. In this way, CONVERGE uses a modified cut-cell Cartesian grid generation method, in which the geometry surface is immersed into a Cartesian block. The cells are sliced at the intersecting surface, the intersection information is later reduced before being stored for each cell. This method allows for complex surface intersections to be represented more easily; the same method is shown in Fig. 4-3 [36]:

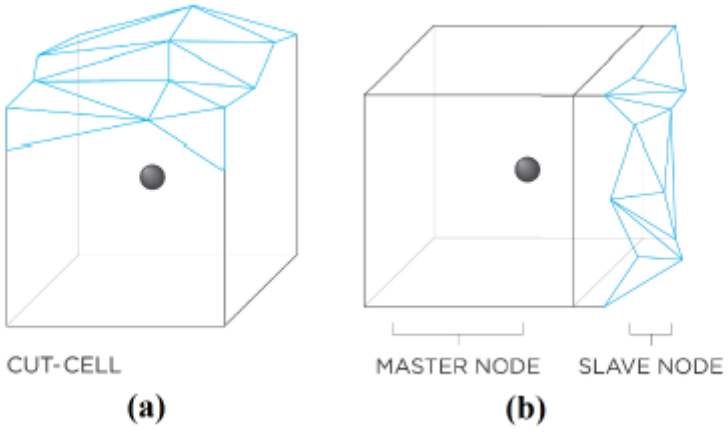

Figure 4-3 Cut-cell method in CONVERGE

CONVERGE considers as slave node a cut-cell whose volume is less than 30% of master node volume. The software matches the master and slave nodes to form a single node, during a process called cell pairing. In this way, the center of the paired node is at the volumetric center of the matched nodes. The slave and master node share the values of the transported quantities, an example of master and slave is shown in the Fig. 4-3 [36].

The Fig.4-4 shows a schematic of the types of cells in CONVERGE, where all nodes are transport nodes and all the transport quantities such as temperature, velocity and species are solved at the center of the transport node (Fig. 4-4a). Another important type of cells in CONVERGE is the parcel cell (shown in Fig. 4-4b), which represents a theorical rappresentation of spray drops that are identical (in terms of size and properties) to one another and it is used to statistically represent the discrete phase of all the spray drops in the parcel [36]

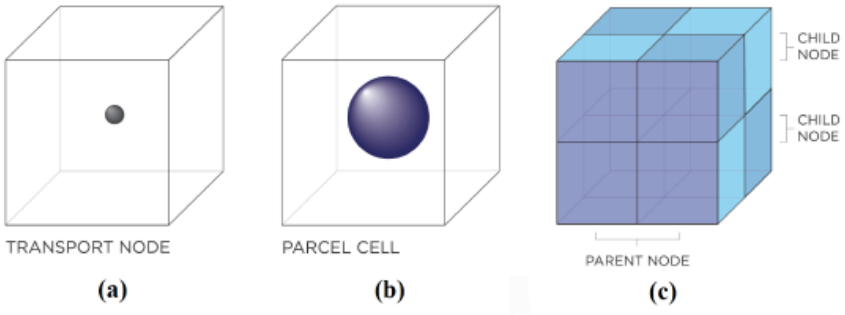

Figure 4-4 Types of Cells in CONVERGE

As described above one of the advantages of CONVERGE is the automatic grid generation, which represents an important tool for the geometry including moving surface (such as the piston in the IC engine). In this case the boundary cells are trimmed, any embedding areas are refined and the refinements from the embedding area are removed, also the grid generation process at each time-step is performed. For the stationary geometries, the software performs the same process once at the start of the simulation and again every time the geometry is refined or coarsened [36].

To control the grid size before and during the simulation, CONVERGE includes a several tools. The grid scaling coarsens or refines the base grid size, the fixed embedding refines the grid at specified locations and times, while the Adaptive Mesh Refinement automatically changes the grid based on the fluctuating and moving conditions [36].

An octree data structure, which is a tree data structure in which each internal parent transport node has exactly eight (or multiplies of eight) children nodes, is employed for grid refinement [36].

4.3.1 Grid Scaling

Grid scaling is related to the variation of the base grid size at specified times during the simulation, which can widely reduce runtimes by coarsening the grid during non-critical simulation times and can allow to catch critical flow phenomena by refining the grid at other times. For an in-cylinder diesel engine flow simulation involving spray and combustion models, in order to ensure accurate

results during the spray the grid must have a higher resolution while a lower grid resolution may be adequate during the compression. CONVERGE uses the *grid_scale* parameter to change the base grid size, depending on: [36]

$$scaled_{grid} = dx\_base/2^{grid\_scale} \quad (4.10)$$

The $grid\_scale$ is the scaling factor, in which the scaled grid is the new base grid size. In addition, CONVERGE uses the the following convention:

- For a $grid\_scale$ value of 0, the software will leave the base cells unchanged
- For a negative $grid\_scale$ value, the software will coarsen the base grid
- For a positive $grid\_scale$ value, the software will refine the base grid

4.3.2 Fixed Embedding

The fixed embedding is used to refine the grid at specific locations into the domain where a finer resolution is fundamental to the accuracy of the solution. For example in the spray simulation it is possible to add an area of fixed embedding by the nozzle to resolve the complex flow charactestic. Moreover, to minimize the simulation time, a fixed embedding allows the rest of the grid to remain coarse. In CONVERGE for each fixed embedding, it is possible to specify an embedding scale, which indicates the grid refinement mode in that location. It must be a positive integer and the base grid size (dx_base, dy_base, dz_base) is scaled in accordance with [36]:

$$dx\_embed = dx\_base/2^{embed\_scale} \quad (4.11)$$

In CONVERGE, it is possible to specify a time for each fixed embedding which allows reducing the computational time of the simulation thanks to refining the grid only for a portion of the simulation. The main types of embedding scales are described below [36]:

1. *Boundary Embedding* is used for a moving surface, in this case the embedding will move with the surface automatically which is very useful when simulating a flow around a valve in IC engine simulation, to have an extra resolution near the valve surface

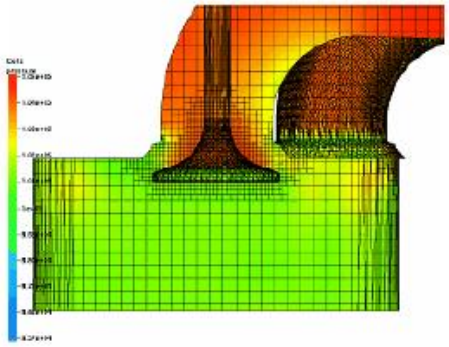

Figure 4-5 A visualization of bound embedding around a valve

2. *Sphere Embedding* is used to specify a spherical area of fixed embedding
3. *Cylinder Embedding* is used to specify a cylindrical or truncated conical area of fixed embedding
4. *Nozzle and Injector embedding*, the *Nozzle* keyword specifies a conical area of fixed embedding around a nozzle, while *Injector* keyword specifies a conical area of embedding around all nozzles in an injector

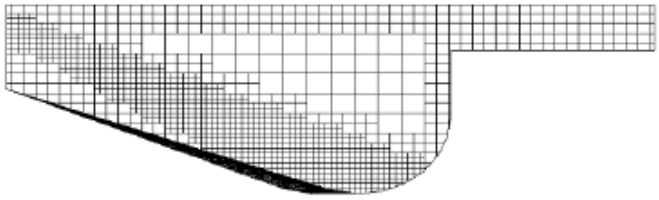

Figure 4-6 A grid generated using a nozzle embedding

5. *Box Embedding* specifies a box of fixed embedding
6. *Region Embedding* speciifes a fixed embedding for an entire region

4.3.3 Adaptive Mesh Refinement

The Adaptive Mesh Refinement automatically refines the grid based on fluctuating and moving conditions such as the velocity and temperature. This option allows to obtaine a highly refined grid to precisely simulate complex phenomena such as high velocity-flow or flame propagation without slowing the simulation with a globally refined grid. A good AMR algorithm will lead to a higher grid resolution where the flow field is most under-resolved or the sub-grid field is the largest, in this way the AMR method in CONVERGE defines the magnitude of the sub-grid field to establish where the software will add embedding [36].

The theory behind the AMR method, establishes that for a scalar quantity, the sub-gride is defined as the difference between the actual field and the resolved field, from the following formula [36]:

$$\phi' = \phi - \bar{\phi} \tag{4.12}$$

Where the actual scalar field is indicated as ϕ, the resolved scalar field is $\bar{\phi}$ and $\bar{\phi}$ is the sub-grid scalar field. The sub-grid for any scalar can be expressed as an infinite series, in which only the first term or the second-order term is used to approximate the scale of the sub-grid [36]:

$$\phi' \cong -\alpha_{[k]} \frac{\partial^2 \bar{\phi}}{\partial x_k \partial x_k} \tag{4.13}$$

Where $\alpha_{[k]}$ indicates the $\frac{dx_k^2}{24}$ for a rectangular cell and the brackets [] indicate no summation. The above equation (4.13) can be easily generalized for a vector field, such as the velocity and AMR method can be used for the following fields such as number of parcel per cells, temperature, void fraction, species, passives or boundary For each condition, the AMR method can be characterized with a different sub-grid criterion and different embedding scale, moreover it is possible to specify for each field, the time when AMR will start and when it will end, similarly to fixed embedding timing control [36].

4.3.4 Adaptive Collision Mesh

An Adaptive Collision Mesh option has been implemented in CONVERGE, where the collision calculations can be highly grid-sensitive. Considering a simulation without coliision mesh, the parcels come up against only with the parcels in the same grid cell, this condition can lead to artifacts in the spray and can be computationally expensive. The use of Adaptive Collision Mesh can eliminate both these problems, in which the simulations with collision mesh, by eliminating grid effects, can more accurately represent the spray dispersion. Only for parcel collision, a uniform grid is used for the collision mesh, which rotates about a random axis at every time-step. In this way, the generated mesh is totally indipendent of fluid-phase mesh and it is used only for the collision mesh. This mesh is created by an algorithm based on randomly selecting of a coordinate system and creating a collision mesh at each time-step [36]:

$$dx_{coll} = dx\_base/2^{coll\_scale} \tag{4.14}$$

Where dx_base is the base cell size. After that, the mesh is created, the parcels are successively placed in the appropriate collision mesh cell, then the collision calculation normally proceeds

4.4 Combustion Modelling

There are several combustion models and chemistry tools available in CONVERGE, one of them that includes combustion models for both premixed and non-premixed models is SAGE detailed chemical kinetics solver described in [38]. The mechanism describing a chemical reaction composed by a set of elementary reactions that involve an overall chemical reaction. From the change of the mechanism (there are mechanisms for gasoline, n-heptane, isooctane, natural gas, etc.) it is possible to model the combustion of different fuels. In this case, SAGE calculates the reaction rates for each elementary reaction while the CFD solver can solve the transport equations. It is possible to use SAGE to model either constant-volume or costant-pressure combustion [36].

From the description of Turns [39], a multi-step chemical reaction mechanism can be written in the following formula:

$$\sum_{m=1}^{M} v'_{m,r} x_m \Leftrightarrow \sum_{m=1}^{M} v''_{m,r} x_m \quad for\ r = 1,2 \ldots . R \tag{4.15}$$

Where the stoichiometric coefficients for reactants and products are denoted by $v'_{m,r}$ and $v''_{m,r}$, respectively for species m and reaction r; R is the total number of reactions and the term x_m is the chemical symbol for species m.

The net production rate of species m is defined by [36]:

$$\dot{\omega}_m = \sum_{r=1}^{R} v_{m,r} q_r \quad for\ m = 1,2 \ldots . M \tag{4.16}$$

Where -M is the total number of species and:

$$v_{m,r} = v''_{m,r} - v'_{m,r} \tag{4.17}$$

The rate-of-progress parameter q_r for the r^{th} reaction is expressed by the following equation [36]:

$$q_r = k_{fr} \prod_{m=1}^{M} [X_m]^{v'_{m,r}} - k_{rr} \prod_{m=1}^{M} [X_m]^{v''_{m,r}} \tag{4.18}$$

Where $[X_m]$ is the molar concentration of species m , k_{fr} and k_{rr} are the forward and reverse rate coefficients for reaction r. The forward rate coefficient in SAGE is expressed by the Arrhenius form, as [36]:

$$k_{fr} = A_r T^{br} e^{(-E_r/TR_u)} \tag{4.19}$$

Where A_r is the pre-exponential factor, b_r is the temperature exponent, E_r is the activation energy and R_u is the universal gas costant. The reverse rate coefficient can be specified from the equilibrium coefficient K_{cr}, as [36]:

$$k_{rr} = \frac{k_{fr}}{k_{cr}} \tag{4.20}$$

From the thermodynamic properties, it is possibile to determine the equilibrium coefficient k_{cr}, as [36]:

$$k_{cr} = k_{pr} \left(\frac{P_{atm}}{RT}\right)^{\sum_{m=1}^{M} v_{mr}} \tag{4.21}$$

Where R is the gas costant, T is the temperature and P_{atm} is the atmospheric pressure.

The equilibrium costant k_{pr} is determined from the following equation [36]:

$$k_{pr} = exp\left(\frac{\Delta S_r^0}{R} - \frac{\Delta H_r^0}{RT}\right) \tag{4.22}$$

The Δ is refered to the variation that occurs in passing completely from reactants to products in the r^{th} reaction [36]:

$$\frac{\Delta S_r^0}{R} = \sum_{m=1}^{M} v_{mr} \frac{S_m^0}{R} \tag{4.23}$$

And

$$\frac{\Delta H_r^0}{RT} = \sum_{m=1}^{M} v_{mr} \frac{H_m^0}{RT} \tag{4.24}$$

Where H and S denote enthalpy and entropy, respectively

The governing equations for mass and energy conservation can be solved for a given computational cell from the above information, in which the governing equation for mass is expressed by [36]:

$$\frac{d[X_m]}{dt} = \dot{\omega_m} \tag{4.25}$$

And the governing equation is expressd for a costant-volume combustion, by.

$$\frac{dT}{dt} = \frac{V\frac{dP}{dt} - \sum_m \left(\overline{h_m}\dot{\omega_m}\right)}{\sum_m \left([X_m]\overline{c_{p,m}}\right)} \tag{4.26}$$

For a costant-pressure combustion:

$$\frac{dT}{dt} = \frac{\left(\dot{Q}/_V\right) - \sum_m \left(\overline{h_m}\dot{\omega_m}\right)}{\sum_m \left([X_m]\overline{c_{p,m}}\right)} \tag{4.27}$$

Where $\dot{Q}$ is the heat release rate, V is volume, T is temperature, P is the pressure, $\dot{\omega_m}$ is expressed by Eq. 4.21, $\overline{h_m}$ and $\overline{c_{p,m}}$ are the molar specific enthalpy and molar costant-pressure specific heat for the species m. At each computational time-step the above equations are solved, and the species are updated adequately. In addition, the temperature obtained from Eq. 4.27, is used to update the rate coefficient but not the CONVERGE cell temperature. The latter is updated after the detailed chemistry calculation has converged using the computed species concentrations. In order to quicken the detailed chemistry calculations, the kinetics components are not solved in cells that drop below a minimum cell temperature (T_{cut}) and a minimum mole fraction (HC_{min}), which represent the minimum mole fraction of CO, H2 and the hydrocarbon species and includes more than just the hydrocarbon species to allow carbon monoxide chemistry occured in the computational cells which does not incorporate hydrocarbon species [36]

4.5 Emissions Modelling

In CONVERGE many models are included to simulate soot or NO_x production, other species of interest such as CO, CO_2, unburned hydrocabons are interpolated or calculated in the software, if they are inserted in the file related to the reaction mechanism and its combustion model used in the simulation. [36]

4.5.1 NOx Modelling

CONVERGE contains three NOx models: thermal NOx, prompt NOx and the third, which is based on the use to the SAGE detailed chemistry solver (described in the section 4.4). For the latter models, if the SAGE detailed chemistry solver is actived, to model NO and NO2, it is necessary to specify the reactions in the mechanism data file and the thermodynamic data file. One of the most important NOx model parameter is the Schmidt number, which is sometimes adjusted to tune NOx with generally only a small effect on the global combustion characteristics. For diffusion flames, in which there is usually actual production of NOx, as the Schimdt number increases, the predicted fuel-air mixing decreases conducting a lower NOx concentration, while for premixed flames, as the Schimdt number increases, the turbolent diffusivity decreases, that leads to a higher NOx concentration. [36]

4.5.2 Thermal NOx Model

The production of NOx is based on wide variety of mechanisms, one of them is the thermal mechanism, which is presentend as the extended Zeldovich mechanism. This mechanism consists in a set of reactions used to calculate NO formation as described in [8]. A more detailed analysis of this mechanism is not present in this thesis work. If the equilibrium values of $[O], [OH]$ and $[H]$, the rate of formation of NO can be written as: [36]

$$\frac{d[NO]}{dt} = \frac{2R_1[1 - ([NO]/[NO]_e)^2]}{1 + ([NO]/[NO]_e)R'} \tag{4.28}$$

Where

$$R' = \frac{R_1}{R_2 + R_3} \tag{4.29}$$

And

$$R_1 = k_{R1,r}[NO]_e[N]_e$$
$$R_2 = k_{R2,f}[N]_e[O_2]_e \quad (4.21)$$
$$R_3 = k_{R3,f}[N]_e[OH]_e$$

Where the subscript f denotes a forward reaction, r denotes a reverse reaction and the subscript e is used to denote the equilibrium species concentration. The terms k_R is used to denote the equilibrium constant for the reactions R.

After the calculation of the equilibrium constant for each species involved in the set of chemical reactions of Zeldovich, the Eq. 4.28 can be solved and by rewriting as:

$$\frac{d\alpha}{dt} = \frac{2R_1[1-\alpha^2]}{[NO]_e(1+\alpha R')} \quad (4.22)$$

$$\alpha = \frac{[NO]}{[NO]_e} \quad (4.23)$$

From the integration of the Eq.4.22:

$$\alpha_2 - \alpha_1 = \beta(1-\alpha_2^2) \quad (4.24)$$

Where:

$$\beta = \frac{2R_1 dt}{[NO]_e(1+\alpha R')} \quad (4.25)$$

In particular:

$$\alpha = (1-\alpha_2^2) \quad (4.26)$$

The term α is evaluated at the end of the computational time-step dt.

Reformulating the Eq. 4.24, in a quadratic form, the solution the updated value of α is expressed by the following equation:

$$\alpha_2 = \frac{-1 + \sqrt{1 + 4\beta(\alpha_1 + \beta)}}{2\beta} \quad (4.27)$$

Finally, the Eq. 4.27 is used to calculate the updated value of α, the Eq. 4.23 is used to calculate $[NO]$ at the end of the time-step. [36]

4.5.3 Prompt NOx Model

The Prompt NO is secundary mechanism to produce NO_x in fuel-rich, low-temperature conditions, which is identified by Fenimore (1971) as a rapid transient formation of NO. This mechanism is most useful for surface combustion, staged combustion applications and gas turbine. CONVERGE employs a simplified model to ensure computational practicability, due to the complexity of the prompt NO mechanism. In this way, the software uses the De Soete (1975) global kinetic parameter to solve the reaction rates. The De Soete approach is expressed by the following Equation: [36]

$$\frac{d[NO]}{dt} = r_{NOx} - r_{N2} \quad (4.28)$$

Where, r_{N2} is the overall molecular nitrogen formation rate and r_{NOx} is the overall prompt NO_x. Also for the Prompt NO_x model, a more detailed analysis of this mechanism is not present in this thesis work

4.5.4 Soot Modeling-Particulate: Size Mimic Soot Model

The complex soot formation and the oxidation process is described using various global steps, including soot inception, surface growth, coagulation and oxidation [36]:

- Soot inception is the process of formation of smallest solid soot particles from the gas-phase hydrocarbon molecules involving the polyciclic aromatic hydrocarbons species. This process serves as connection between gas-phase chemistry and soot particle dynamics, which is described by the collision of two PAH molecules
- Soot surface growth is required to obtain two-way coupling with the gas phase. The soot mass growth, heterogeneous reactions on surfaces and the loss of soot particles due to reactions with gas-phase species play a fundamental role in the soot formation
- The physical process of collisions between small soot particles leading to the formation of larger soot particles is called soot coagulation

- The PAHs coagulate together and form large soot particles in the soot condensation

The various steps of soot formation are shown in the Fig. 4-7.

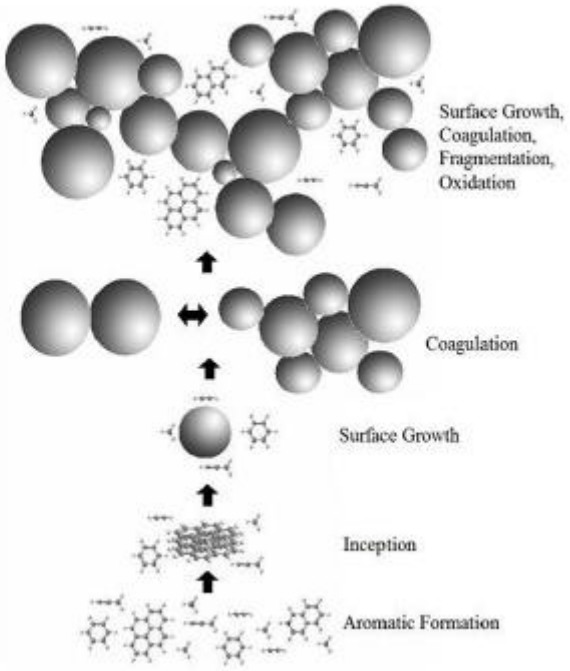

Figure 4-7 A descriptive overview of soot formation [36]

CONVERGE uses various models to describe the steps of soot formation, in which the reaction rates of these global steps are defined by implementing simplified physical models or by empirical expression involving some parameters to match the experimental results. In addition the soot models introduced in CONVERGE generally are solved with detailed PAH chemistry. The empirical soot oxidation model is described by the Hiroyasu-NSC model and the phenomenological models describing the inception, surface growth, coagulation and oxidation are described by the Gokul, Dalian and Waseda models. All the models are included in CONVERGE. In addition, the software contains two detailed soot models: Particulate Mimic (PM) model and Particulate Size Mimic (PSM) model. The detailed soot models offer a comprehensive mathematical description for the soot particle distribution function, called PSDFand they can solve the complex soot formation and oxidation with detailed chemistry. For these reasons, the detailed models perform better over wide ranges of operating conditions, so when more comprehensive soot formation analysis is required these models represent the best option. [36]

The soot particle distribution function describes the properties of a soot ensemble and it influenced by the physical and chemical processes which may lead to variations for the same. From the knowledge of these processes, it is possible to solve the equations for the number density of all size classes to obtain the PSDF of soot. In this way, the result will be an infinite set of partial differential equations to be solved. There will be hunderds of thousands of equation resulting computationally impossible to obtain numerical solutions using today's computer power. Therefore, to reduce the size of the problem, it is possible to use certain mathematical methods.

In pratical simulations, the focus is the integral features of PSDF, which provide the most important information about the soot particle ensemble, such as mean mass or volume, mean diameter of the particles and mean particle number density. In this way, the method of moments play an important role, which is based on the concept that the resolution of an infinite set of equations for the statistical moments of the soot particle distribution function is equal to the direct simulation of the PSDF. For this method, the accuracy of the approach increases with the number of moments used, in which a set of equations for the first two to six moments is usually applied. In this way, the method shows a higher computational efficiency, in addition the major features of the PSDF such as soot volume fraction and mean number density are extracted from the moments. The Particulate Mimic model is based on the method of the moments in CONVERGE. The basic physical and chemical processes described above, assumed to be important for the soot formation process such as: inception, coagulation, condensation and heterogeneous surface reactions, surface growth and oxidation by the O2 and OH. A set of equations for the moments of the soot particle size distribution function are used to describe the dynamic of soot particle characteristics: [36]

$$\frac{dM_r}{dt} = \dot{M}_{r,pi} + \dot{M}_{r,con} + \dot{M}_{r,coag} + \dot{M}_{r,sr} \tag{4.29}$$

Where $\dot{M}_{r,pi}, \dot{M}_{r,con}$, $\dot{M}_{r,coag}$, $\dot{M}_{r,sr}$ represent the rates of particle inception, condensation, coagulation and surface growth for the r^{th} moment of the PSDF. The moments are expressed from the following equation:

$$M_r = \sum_{i=1}^{\infty} i^r N_i \tag{4.30}$$

Where N_i indicates the number density of soot particles of size i.

The zeroth moment is related to the mean number density and the first moment is related to the mean volume or mean mass of the soot particles. Considering each moment in the particulate mimic model, this is solved as globlal transport passive [36]:

$$\frac{D\left(\dot{M}_r/\rho\right)}{Dt} = \nabla\left(\frac{\mu}{SC}\nabla\left(\frac{\dot{M}_r}{\rho}\right)\right) + \dot{S}_{Mr} \tag{4.31}$$

$$\dot{S}_{Mr} = \dot{M}_{r,pi} + \dot{M}_{r,con} + \dot{M}_{r,sg} + \dot{M}_{r,ox} + \dot{M}_{r,coag} \tag{4.32}$$

Where $\dot{S}_{Mr}$ is the source term and SC represents the Schimdt number.

The moment source term is matched with species source term and solved using SAGE solver. In represents a two-way coupling, which indicates that the soot formation will influence the gas phase and system heat release. [36]

Stages of the PM model including soot inception, coagulation, surface reactions and condensation are characterized in [36]

4.6 Discrete Phase Modelling: Spray Modeling

To calculate the spray in the simulation, CONVERGE introduces drop parcels into the domain where the injector is located at a user-specified rate. The parcels represent a group of drops which have the same physical and thermodynamics properties, such as radius, velocity, temperature, etc, and they are used to represent the entire spray field in a statistical way. The concept of the drop parcels allows CONVERGE to reduce the computational time of a simulation involving spray. The spray droplets are subject to maby processes, which take place from the time of injection until the time of vaporization, such as breakup, collision, coalescence and turbolence dispersion [36].

4.6.1 Liquid Injection

Two categories of liquid injection mechanism are included in CONVERGE: The injector is a group of nozzles, which have the same characteristics and each injector can have any number of nozzles, with its own cone angle, hole size, orientation and position. [36]

The contraction effects of the nozzles in each injector are included in CONVERGE. The contraction coefficient, C_a, is expressed by the following equation:

$$C_a = \frac{C_d}{C_v} \tag{4.33}$$

Three orifice coefficients can be introduced to describe the liquid fuel flow leaving the injector nozzle, with reference to the theory of Siebers. From the Eq. 4.33, C_d is the discharge coefficient, C_a is the area contraction coefficient and C_v is the velocity coefficient. These coefficients are calculated based on the injection pressure at that time of injection. When the liquid fuel is injected from the nozzle injector, the effective area of the nozzle is reduced due to the cavitation or hydraulic flip effects, which are included in the area contraction coefficient, while the drop velocity is increased proportionally [40]. The effective flow area, A_{eff}, is given by:

$$A_{eff} = C_a A_0 \tag{4.34}$$

Where A_0 is the geometric area of the nozzle. From the Eq. 4.34, it is shown that the effective diameter of the nozzle is reduced with reducing of the contraction coefficient:

$$d_{eff} = \sqrt{C_a} d_0 \tag{4.35}$$

Where d_0 is the geometrical nozzle diameter

To preserve the mass flow rate, the effective fuel velocity U_{eff} is modified through the following Equation, including the velocity coefficient C_v

$$U_{eff} = C_v U_b \tag{4.36}$$

Where U_b is the Bernoulli velocity

When the effective area of the nozzle A_{eff} is reduced has the consequence the reduction of initial parcel size and the proportional increase of the drop velocity magnitude. The nozzle coefficients are important to calculate the experimental quantity for a particular experimental condition, such as the effective nozzle flow area and velocity, which are used to set the boundary condition for the spray model [40].Then, the injection pressure is given by:

$$P_{inj} = \frac{\rho_l}{2}\left(\frac{V}{C_d}\right)^2 \tag{4.37}$$

Where ρ_l is the liquid fuel density and V is the liquid fuel velocity. From the Eq. 4.37, it is shown the importance of the nozzle discharge coefficient to predict the quantity of premixed phase of diesel combustion, which is directly influenced by the injection pressure

4.6.2 Injection Size Distributions

CONVERGE offers four injection size distributions: blob, chi squared, Rosin-Rammler and constant injected radius distibutions [36].

Blob Injection Model

The Blob Method was discovered by Reitz and Diwakar in 1987, is one of the simplest and most popular models. This model creates a group of large spherical droplets with the same diameter, which is usually equal to the nozzle hole diameter, these droplets are then subject to secondary breakup. The number of drops injected per unit time is calculated from the mass flow rate and the injection velocity of the blobs is determined by the conservation of mass [41]

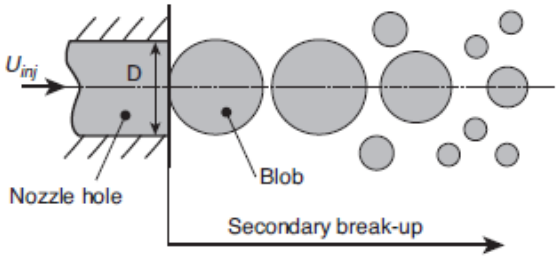

Figure 4-8 Schematic of the Blob Method

An enhanced version of the blob method, suggested by Kuensberg Sarre *et al*. (1999), calculates the effective injection velocity and injection particle diameter by the reduction of the nozzle cross section due to the cavitation. However the blob methods are a good way to determine the initial starting conditions for the liquid jet entering the combustion chamber, unfortunately it does not represent a detailed physical model of the relevant processes during primary break-up [41]

Rosin-Rammler Distributions

The cumulative probability function for the Rosin-Rammler distribution is expressed by the following formula [36]:

$$\check{R}(r) = 1 - exp[-\zeta^q] \quad 0 < \zeta < \zeta_{max} \tag{4.38}$$

Where:

$$\zeta = \frac{r}{\bar{r}} \tag{4.39}$$

And

$$\bar{r} = \Gamma(1 - q^{-1}) r_{32} \tag{4.40}$$

Where Γ is the gamma function, r_{32} is the Sauter mean radius and q is an empirical costant. This last parameter measures the diffusion of the droplet size, the fluid flow will be more uniform when q parameter quickly grows. After selecting a value of ζ, the injected drop radius is calculated from:

$$r = \bar{r}\zeta = \Gamma(1 - q^{-1}) r_{32}\zeta \tag{4.41}$$

4.6.3 Drop Drag

The determination of drop drag coefficient is more important for detailed spray modelling, two drop drag models are used in CONVERGE. In the first model, the drops are considered perfectly spherical and then the drag coefficient is calculated. The second model, called dynamic drag model, calculates the droplet drag coefficient dynamically. In this case the variations in the drop shape are considered through the drop distorsion parameter y. The values of the drop distorsion parameter are determined from the Taylor Analogy Breakup (TAB) model, which is based on Taylor's analogy between a distorting and an oscillating droplet and a spring-mass system, detail descriprion is given in [36].

When the spherical droplet initially moves through the gas, its shape changes significantly and under this condition the Weber number (a dimensionless parameter defined as the ratio of aerodynamics forces to surface tension forces) reaches high values. In the extreme case, the drop will take the shape of a disk, in which the drag is greatly higher than the spherical drop. In this way, the condition described above shown the dependency of the drag force on the drop shape, for this reason a drag model must include the effects of the drop distorsion. These effects are represented by a linear dependence variation between the drag coefficient in spherical condition and the drop distorsion parameter, finally the drag coefficient is given by the following equation [36]:

$$C_D = C_{D,sphere}(1 + 2.632y) \tag{4.42}$$

Where, y is the drop distorsion, which is described in the TAB model.

4.6.4 Spray Breakup

Several spray breakup mechanisms are included in CONVERGE, which include models based on the Kelvin-Helmholtz (KH) and Rayleigh-Taylor (RT) instability mechanisms, the LISA sheet breakup model and the Taylor Analogy Breakup (TAB) drop breakup model. In addition, the Eulerian-Lagrangian Spray Atomization (ELSA) for the prediction of the primary spray breakup is included.

The TAB model is used in many CFD codes for secondary atomization of the droplets, which were formed during the primary atomization process. This model is suitable, in conjunction with primary breakup models, in simulating the penetration length or SMD of hollow-cone sprays injected at pressures variables 4 to 10 Mpa. [42]

The LISA sheet breakup model is also used for hollow-cone GDI spray, which assumes that the hollow liquid sheet is created near the nozzle exit and breaks into ligaments first and subsequently form primary droplets. This model consists in both a film formation, a sheet breakup and the atomization [42]

The Blob model describes the injection of liquid drops with a diameter equal to the effective nozzle diameter and the Kelvin-Helmholtz instability is used to predict the breakup of the jet.The Kelvin-Helmholtz model was proposed by Reitz (1987), and it is based on a first order linear analysis of a Kelvin-Helmholtz instabily, which grows on the surface of a cylindrical liquid jet penetrating into a stationary, inviscid and incompressible gas with a relative velocity [41]

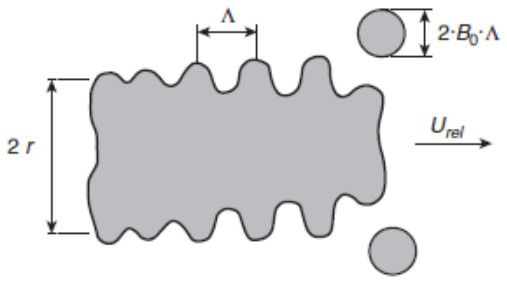

Figure 4-9 Schematic of KH instability [41]

The model considers the stability of a cylindrical, viscous, liquid jet of radius r_0, outgoing from a circular orefice at a velocity U into a inviscid, incompressible, stagnant gas of density ρ_g. The liquid has a viscosity μ_l , a density ρ_l and a cylindrical polar coordinate system moves with the jet. [36]

In the KH model, the parent parcel with radius r, breaks up to form new droplets with radius r_c, which is proportional to the wavelength of the fastest growing unstable surface wave Λ_{KH}:

$$r_c = B_0 \Lambda_{KH}: \tag{4.43}$$

Where B_0 is a model constant, for which a smaller value of B_0 will result in smaller drops from breakup, while a large value will result in larger droplets.

The rate of change of drop radius in a parent parcel is expressed by:

$$\frac{dr_p}{dt} = -\frac{(r_p - r_c)}{\tau_{KH}} \quad (r_c \leq r_p) \tag{4.44}$$

Where τ_{KH} represents the breakup time and it is given by:

$$\tau_{KH} = \frac{3.726 B_1 r_p}{\Lambda_{KH} \Omega_{KH}} \tag{4.45}$$

Where Ω_{KH} is the maximum growth rate, B_1 is the breakup time constant, which is related to the initial disturbance level on the liquid jet and varies from one injector to another. CONVERGE allows to run the KH model with or without the generation of new child parcels. After the droplet break-up, pieces of it fragment away. When the accumulation of these fragmented masses reaches a sufficient amount of mass, they are considered as child parcels. The mass of the fragmented liquid is expressed by:

$$\sum_n s N^n \frac{4}{3} \pi \rho_l \left[\left(r_p^n \right)^3 - \left(r_p^{n+1} \right)^3 \right] \tag{4.46}$$

Where s is the $shed\_factor$, which characterizes the fraction of the parent parcel mass that contributes to the child parcel mass. CONVERGE creates a child parcel with a drop size of radius r_c each time that the mass of the fragmented liquid exceeds the $newparcel\_cutoff$ which is generally 3 to 5 percent of the average injected parcel mass. After that the child droplets are determined, they must be added to the computation. The child droplets are defined by a velocity component normal to the path of the parent drop, this normal velocity is given by:

$$v_n = C_1 \Lambda_{KH} \Omega_{KH} \tag{4.47}$$

Where C_1 is a model costant.

Rayleigh-Taylor Breakup Model

The secundary break-up consists into the disintegration of already existing droplets into smaller ones because of the aerodynamic forces. These forces are produced by the relative velocity between the droplet and the surrounding gas. Therefore an unstable growth of waves is produced on the droplet surface, leading to the disintegration of this and the formation of new droplets [41].

The Rayleigh-Taylor model is used to predict the secundary atomization. The RT model defines the instabilities on the surface of the drop, which grows until a certain characteristic break-up time when the drop breaks up. [43]

In the RT mechanism, the unstable waves occurs due to the rapid deceleration of the drops from the intensity of drag force, $\left| F_{D,i} \right|$ which is expressed by:

$$\left| F_{D,i} \right| = M_d |a_i| = \frac{3}{8} M_d C_d \frac{\rho_g |U_i|^2}{\rho_l r_0} \tag{4.48}$$

Where $|a_i|$ is the deceleration of the drop, M_d is drop mass and C_d is the drag coefficient. The effect of gas and liquid viscosity is usually neglected in the RT breakup model but CONVERGE extend the standard RT model to include viscosity. The viscosity has a large effect on high decelerations of the spray droplets.

The wavelength corresponding to the fastest growth rate is compared to the radius of the droplet. When the wavelength is smaller than the droplet diameter, the RT waves are grown on the surface of the drop, which begin to grow on the surface of the droplet within a characteristic time. This time is compared to the breakup time:

$$\tau_{RT} = \frac{C_\tau}{\Omega_{RT}} \tag{4.49}$$

Where τ_{RT} si the RT liquid breakup time, C_τ is a costant and Ω_{RT} is the maximum growth rate. If the RT waves grows for a time greater than the breakup time τ_{RT}, the drop is assumed to break up, and the radii of the new smaller droplets is calculated by:

$$r_c = \frac{\pi C_{RT}}{\Lambda_{RT}} \tag{4.50}$$

Where C_{RT} is the RT model size constant, which can be decreased or increased to change the size of the predicted break up radius, the Λ_{RT} is the fastest growing wavelength for RT instabilities. In similiar way, the RT break up constant time C_τ can be increased to delay RT breakup or decreased to promote faster RT breakup mechanism

4.6.5 KH-RT Breakup Length Model

The two break-up models Kelvin-Helmholtz and Rayleigh-Taylor, based on the fundamental liquid/gas instability mechanism, can be run cuncurrently on CONVERGE. This hybrid model predicts a better drop size distribution and calculates drop size trends closer to experimental data than the lone Kelvin-Helmholtz model. The KH-RT model toghther with the breakup length concept was introduced by Ricart et al. Reitz and Bacco mentioned the existence of a length of intact liquid near the nozzle of the jet, in which an intact liquid core must exist in a region inside the jet where it has not yet been affected by the surrounding air. Hiroyasu noted that breakup after a certain length occurs at a different rate than before the core length [43]

If the KH-RT breakup length model is actived on CONVERGE, this intact core or the breakup length L_b, is described as [36]:

$$L_b = C_{bl}\sqrt{\frac{\rho_l}{\rho_g}}d_0 \tag{4.51}$$

This model assumes that the drop breakup inside of the characteristic breakup distance, L_b, is due to the only KH mechanism, while both KH and RT mechanisms are activated beyond the breakup length. In this case, CONVERGE first controls if the RT mechanism can break up the droplet, if not, the only KH mechanism is responsible for breakup. The following figure summarises the model described above [36]:

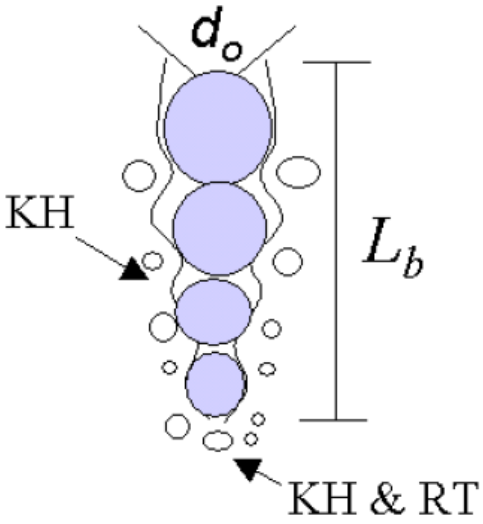

Figure 4-10 Schematic of the KH-RT spray breakup model [36]

From the Eq. 4.51, C_{bl} is the breakup length constant, which can be tuned to decrease or increase spray breakup. For very high gas Weber number, We_g, which is a typical condition of Diesel sprays and $\mu_l = 0$, the Eq. 4.45 (KH model breakup time) is expressed as: [36]

$$\tau_{KH} = \frac{B_1}{U}\sqrt{\frac{\rho_l}{\rho_g}}r_0 \tag{4.52}$$

And

$$L_{KH} = U\tau_{KH} \tag{4.53}$$

Finally:

$$L_{KH} = B_1 \sqrt{\frac{\rho_l}{\rho_g}} r_0 \qquad (4.54)$$

From the comparison between the Eqs. 4.54 and 4.51, the C_{bl} must be equal to $\frac{B_1}{2}$, which is breakup time constant in KH model.

4.6.6 Modified KH-RT Model

CONVERGE allows to run a simulation with both breakup mechanism without the use of a characteristic breakup length definition. In this case, the aerodynamic instabilities are responsible for the primary breakup of the the injected liquid blobs, called the parent drops. The child drops are created during the same process, in which the secondary breakup of these is modeled by the competing effects of the KH and RT mechanisms. [36]

4.6.7 Drop Collision

CONVERGE offers two collision and coalescence models O'Rourke Numerical Scheme and No Time Counter model, and two models for the collision outcomes O'Rourke and Post Collision Outcomes. The No Time Counter (NTC) model is described in [36], this method is based on techniques used in gas dynamics for Direct Simulation Monte Carlo calculations. The NTC method requires stochastic sub-sampling of the parcels within each cell, this method results in much faster collision calculations. Comparing the O'Rourke method with the NTC method, in the first method the multiple collisions can occur between the parcels, in which the process is governed by a Poisson distribution. If the collisions have effects the parcels, the Poisson distribution is not correct. The collisions can change the velocity, size and number of the parcels, in this way the method of repeated sampling used by the NTC model produces more accurate answers. In addition, the NTC method shows a linear relation between the computational cost and number of the parcels, while the O'Rourke method predicts that the computational cost grows with the square of the number parcels. [36]

The No Time Counter method is based on the basic probability model for stochastic model, in which the basic probability model requires that the cell size be sufficiently small to neglect spatial differences for spray quantities. These hypothesis are a subset of those required for deriving the O'Rourke collision model. Initially the NTC method orders packages in groups, which reside in the same cell, this process requires only 2N operations, where N is the number of droplets in a cell. Later, the NTC method choose a stochastic subsample from all the possible pairs in a cell. In this way, the probabilities for the subsample pairs are multiplied by the reverse of this fraction, so the probability of the collision is increased. The sampling is done thanks to the replacement so that multiple collisions for a pair can be calculated in a currect way. The resulting method shows

the linear proportianlity between the cost and the number of parcels, as opposed to the N-squared cost. [36]

For the collision outcomes, the O'Rourke Collision method can result in grazing collisions or in coalescence. Post and Abraham (2002) included both stretching separation and reflexive separation in their method based on experimental results of hydrocarbon drops, this method is called Post collision outcomes. [36]

4.6.8 Drop turbolent dispersion

The effects of the turbolent flows on spray drops are included in CONVERGE. The fluctuating velocity u' is described into the RANS or LES turbolence model. For the RANS turbolence model, the depletion of turbolent kinetic energy due to the work done by turbolent eddies to scatter the liquid spray droplets, CONVERGE includes source terms. In addition, the source terms include the fluctuating component of the velocity u' for the fluid-phase. Two models are used to calculate u' [36]

1. Turbolent Kinetic Enery preserving model, in which each each component of u' is chosen as $|u_i'| = \sqrt{2k}$, k is the cell turbolent kinetic energy
2. O'Rourke Model, in which each component of u' follows a Gaussian distribution

A more accurate description of the two models is present in [36]

4.6.9 Drop/Wall Interaction

CONVERGE includes three options for modelling drop/wall interaction, which are described as follows:

1. Rebound/Slide Model: this model is based on the wall impingement model of Naber and Reitz (1988), successively improved by Gonzalez et al., (1991). Two impingement regimes, rebound and slide are introducend in this model, which are based on the Weber number of the incoming drop at impact:

$$We_i = \frac{\rho_l V_n^2 d_0}{\sigma} \tag{4.55}$$

   Where V_n is the velocity component normal to the surface.
   From the Eq.4.55, if the We_i is less than 80, the regime bound is activated, in which the drop rebounds elastically with a normal velocity. While, if the We_i is greater than 80, the drop velocity is updated by using the Naber and Reitz jet model, in which it is possible to determine the sheet thickness produced from an impinging liquid jet
2. Wall Film Model: this model uses a hybrid approach to film modelling including the interaction of liquid drops with the solid surfaces. In fact, some calculations are carried out

considering only certain quantities of the particles. For example, to model the film wall, a wall face α is used and thickness of the film h_α on it, which is expressed by the following Equation:

$$h_\alpha = \frac{\sum_p V_p}{|A_{\alpha,i}|} \tag{4.56}$$

Where V_p is the volume of the parcel, p, the term $A_{\alpha,i}$ identifies the area projection vector of the face α, the summation is refered to all particles located on the face α. The area projection vector of the face α is described as film initialization, in which a wall film can be initialized on the entire boundary in a specifi shape, circular or rectangular, and then the projection of these is taken on wall boundaries, as shown in Fig.4-11. To model the liquid film transport, the film momentum equation of O'Rourke and Amsden is used, which updates the velocities of the particles that impinged on the solid surface in the previous time-step, a more accurate description of this equation is presented in [36]. In addition, if the particle has just impinged on a wall in the current time-step, CONVERGE determines the velocity of the particle with the Rebound/Slide Model

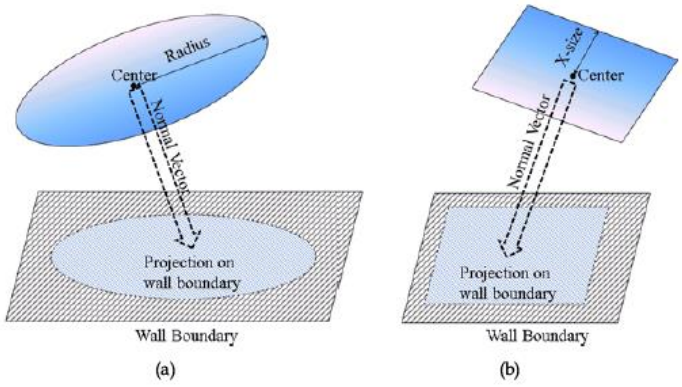

Figure 4-11 Circular/Rectangular wall-film initialization

3. Drop Vanish Model: When the spray droplets collide on the wall boudary, these vanish due to the disappearance of the drop mass from the simulation in such an istance.

In addition, three wall film model including the drop/film spashing are available in CONVERGE: O'Rourke, Kuhnke and Bai-Gosman. The Wall Film Model, previously described, inclueds two additional effects: film separation and film stripping.

The first can occur if the wall film particles flow over a sharp corner. The film separation takes place through the criterion of O'Rourke and Amsden (described in [36]), which if it is satisfied, the film parcels are transformed into a spray parcel with a diameter equal to the film thickness.

The second effect, called film stripping, the growth of waves on the surfaces, generated by aerodynamic forces acting on the the flm wall, create the film stripping. When the waves reach a

critical amplitude, the liquid is fragmented into ligaments, which tend to take a cylindrical shape that subsequently move normal to the ligament axis. Finally, the capillary forces cause the unsteadiness of the ligaments to break into drops.

4.6.10 Drop Vaporization Model

CONVERGE offers two vaporization models to describe how the radius of a drop changes over time, which are called Frossling correlation and the Chiang correlation. In addition, the software includes two different methods for computing thermal transfer to the drop, the uniform temperature model, in which the temperature of the droplets is assumed to be uniform, and it is solved through two ordinary differential equations. The Discretized temperature model, in which the temperature of the droplet is asumed to be spherically simmetric and it is solved through a partila differential equation.

The Frossling correlation is based on the concept that when liquid fuel is injected into the computational domain, a model is required to convert the liquid into gaseous vapor:

$$\frac{dr_0}{dt} = -\frac{\alpha_{spray}\rho_g D}{2\rho_l r_0} B_d Sh_d \qquad (4.57)$$

Where the term α_{spray} indicates the user-specified scaling factor for the mass transfer coefficient, the mass diffusivity of liquid vapor in air is expressed by D, B_d is defined as:

$$B_d = \frac{Y_1^* - Y_1}{1 - Y_1^*} \qquad (4.58)$$

Where, Y_1^* represents the vapor mass fraction at the surface of the drop, Y_1 is the vapor mass fraction. The term Sh_d is the Sherwood number expressed as:

$$Sh_d = \left(2.0 + 0.6 Re_d^{1/2} Sc^{1/3}\right) \frac{ln(1 + B_d)}{B_d} \qquad (4.59)$$

And

$$Re_d = \frac{d\rho_{gas}|u_i + u_i' - v_i'|}{\mu_{air}} \qquad (4.60)$$

Where the Eq 4.60, d is the drop diameter and μ_{air} represents the air viscosity which is determined at the temperature $\hat{T}$ expressed as the follows equation:

$$\hat{T} = \frac{T_{gas} + 2T_d}{3} \tag{4.61}$$

In the previous Equation, T_d represents the temperature of the droplet. From the Eq. 4.59, the Schmidt number of air, Sc, and D are shown in it. The term D is calculated with two experimentally-determined model constants D_0 and n_0

In the Chiang correlation, two different correlations of Nu_d and Sh_d are used:

$$Nu_d = 1.275(1 + B_d)^{-0.678} Re_d^{0.438} Pr_d^{0.619} \tag{4.62}$$

And

$$Sh_d = 1.224(1 + B_d)^{-0.568} Re_d^{0.365} Sc_d^{0.492} \tag{4.63}$$

The Eqs. 4.62 and 4.63 are subsequently used to determine the rate of change of droplet radius, as:

$$\frac{dr_0}{dt} = -\frac{\alpha_{spray}\rho_g D}{2\rho_l r_0} B_d Sh_d (Y_1^* - Y_1) \tag{4.64}$$

In addition, CONVERGE offers a model for droplet radius change boiling regime, the time rate change of the droplet radius when the temperature of the droplet exceeds the boiling point, is expressed by the following equation:

$$\frac{dr_0}{dt} = \frac{k_{air}}{\rho_d c_{p,\infty} r_0}\left(1 + 0.23\sqrt{Re_d}\right) ln\left[1 + \frac{c_{p,\infty}(T_{air} - T_d)}{h_{fg}}\right] \tag{4.65}$$

Where $c_{p,\infty}$ is specific heat capacity of the air, and k_{air} represents the thermal conductivity of the air. This model considers that each droplet reaches the the boiling temperature, which is determined individually for each component

5 Surrogate Fuel

5.1 Introduction

The Computational Fluid Dynamics calculations for the internal combustion engines are diffusely used by automotive research to optimize IC engine designs for performance, low pollutant emissions and efficiency. The reformulated fuels, such as Fischer-Tropsch or biofuels, has made it possible to assess the effect of the fuel composition on the engine performance and emissions. The chemical kinetics model which governs the combustion process, must be validated and accompanied by a CFD code to carry out a numerical simulation. In this way, a real fuel includes hundreds if not thousands of chemical compounds and their behaviour are described by certain physical and chemical properties. In addition, due to the high number of individual constituents in real fuel make the CFD modelling computationally unfeasible, therefore the choice of a surrogate fuel, which is defined by a mixture of a small number of compounds, is necessary to represent the real fuel chearacteristics and simplify the development of a model of chemical kinetics. [44] Thanks to the development in high-performance computing (HPC) capability, complex chemistry can now be applied for large scale practical engine simulations.

5.2 Surrogate Selection Approach

From the work of Edwards and Maurice [45] surrogate formulation can be divided into two main categories. In the first, the goal is focused on matching physical, chemical and combustion properties of the real fuel, such as cetane number, volatility and density. The second approach is focused on the direct emulation of the active functional groups like propyl, methyl and ester groups. The first apprach was followed in this work, and the aim is to improve the CFD simulations, reducing the difference between target and surrogate fuels, also a high computational power is required. The combustion process in DI Diesel engine consists of the following phases, described in detail in the section.2.3:

- Ignition delay
- Premixed Combustion phase
- Mixing-Controlled Combustion phase
- Late Combustion phase

The liquid fuel injected into the combustion chamber is subjected to a physical and chemical phenomena, which characterize the ignition delay period. The liquid jet fuel is sujected to a breakup process generating small droplets. In this first phase, the suface tension is one of the key-properties for the spray breakup model and collision/coalescence model, the liquid viscosity is considered in modeling drop internal flow, wall film motion and drops breakup. After the breakup, the fuel droplets are subjected to an evaporation process, due to the heat flow from the high temperature environment to the single drop of fuel. In this phase, the liquid thermal conductivity is used to evaluate the heat transfer between the drop interior and the outer surface, also the vapor heat capacity is important to determine the temperature distribution and internal energy of the gas mixture which involves the fuel droplets. [46]
Finally, the air-vapor fuel mixture is highly influenced by the geometry of the combustion chamber and turbulent motion in the chamber. Analyzing the chemical process, the fuel is divided into small

hydrocarbons, and the active radicals favor the spontaneous ignition, up to the premixed phase. In this phase, some fuel properties are the most important: cetane number, the oxygen content, and the C/H ratio
The cetane number represents the measure for the the selfignitability of the fuels and in this work the cetane numbers for each components are taken from the literature. The oxygen content has an impact on stoichiometry and the soot formation, and the C/H ratio reflects the adiabatic flame temperature and the heat of combustion [47]
The schematic of ignition delay is shown in the Fig. 5-1

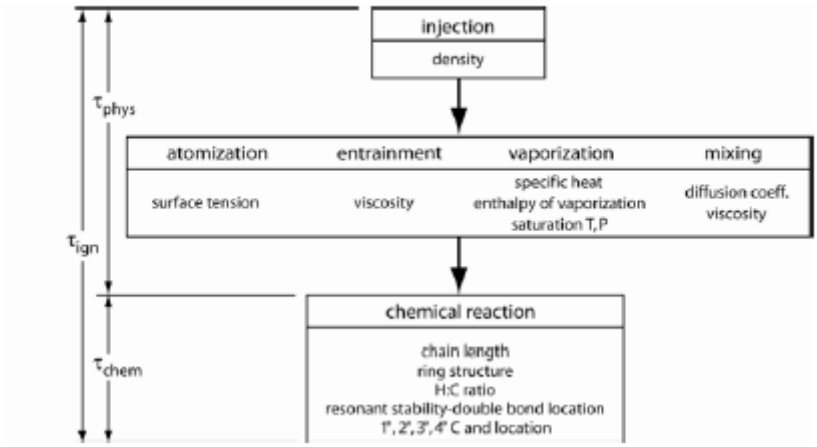

Figure 5-1 A conceptual model of ignition delay [48]

In this work, the following target properties are considered to create the surrogate fuel:

- Cetane number CN
- Density ρ
- Lower Heat of Combustion LHC
- C/H mass ratio ……. C/H
- Distillation curve

In Fig. 5-2, the flow chart describes the validation process of the surrogate formulation approach used in this work

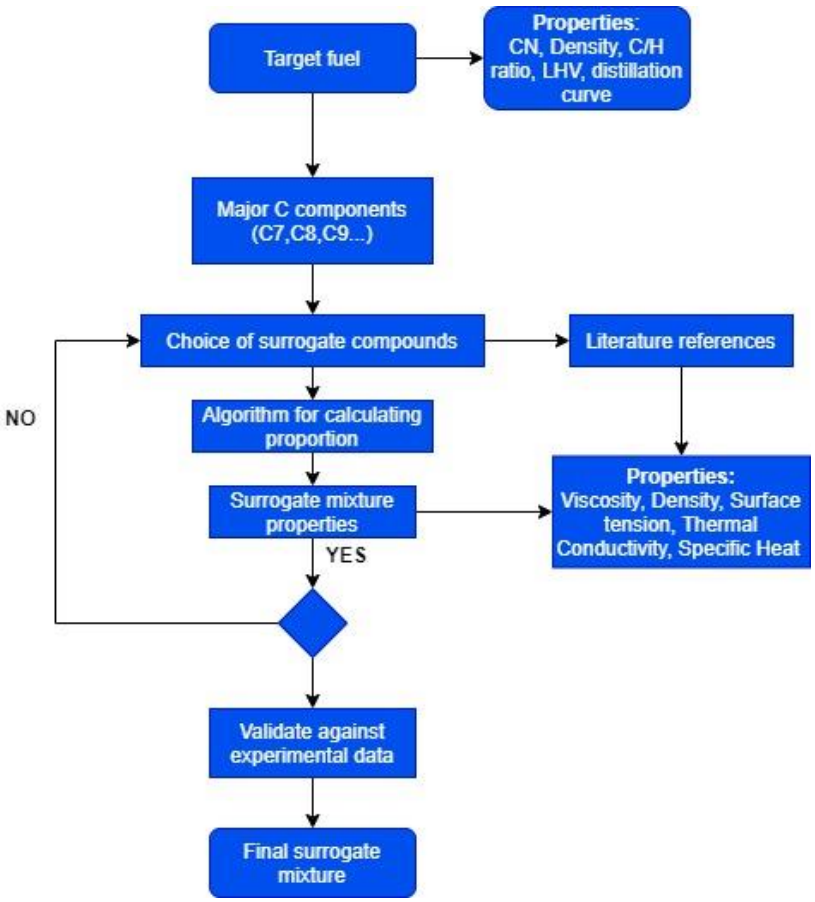

Figure 5-2 Flow Chart validation process

5.2.1 Surrogate Formulation algorithm

The algorithm is proposed by the work of Li et al. [49], which is based in a N-Dimensional space, where N represents the number of the target properties, so the target and surrogate fuel can be identified as two vectors in the space. Finally, through the Euclidean distance between the two vectors, the algorithm can minimize this distance, obtaining the optimal composition for the surrogate. In Fig. 5-3, a representation of this method, considering a ternary mixture is shown:

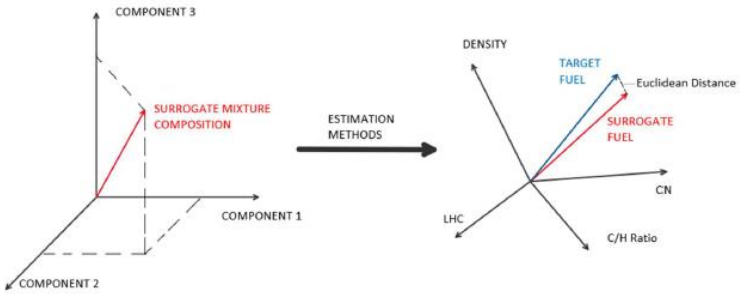

Figure 5-3 Li et al. Method

In addition the properties of the mixture have been calculated by estimation methods based on the volume, mass, molar fractions:

Property	Estimation
Cetane Number	$CN_{mix} = \sum v_i CN_i$
Density	$\rho_{mix} = \sum v_i \rho_i$
Lower heat of Combustion	$LHC_{mix} = \sum \gamma_i LHC_i$
C/H mass ratio	$CH_{mix} = \sum X_i CH_i$

Table 5-1 Property estimation

From the Table 5-1 v_i, γ_i, X_i respectively represent the volume, mass and molar fraction of the i-component, and the algorithm is created by a MATLAB script, so the Euclidean distance is calculated through the following formula:

$$ED = \sqrt{\left(CN_{target} - CN_{mix}\right)^2 + \left(\rho_{target} - \rho_{mix}\right)^2 + \left(LHC_{target} - LHC_{mix}\right)^2 + \left(CH_{target} - CH_{mix}\right)^2}$$

(Eq. 5.1)

5.2.2 Diesel Surrogate

The Diesel fuel is usually composed of C_{10}~C_{24} hydrocarbons including [50]:

- 50~65 % alkanes, mostly n-alkanes
- 20~30 % cycloalkanes
- 10~30 % aromatics

The primary hydrocarbons types are:

- n-alkanes, satured straight-chain hydrocarbons
- Iso-alkanes, satured branched-chain hydrocarbons
- Cyclo-alkanes, satured hydrocarbons with one or more satured ring structure
- Aromatics, hydrocarbons with one or more benzene ring structure

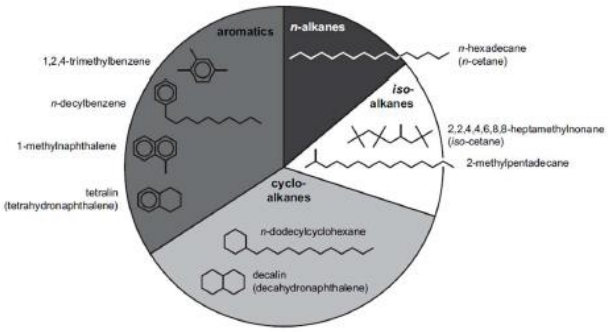

Figure 5-4 Diesel Composition

The fuel Diesel composition is highly variable, which is shown in the Fig. 5-4. In the work of Mueller et al [50], was presented a selection of nine types of candidate components to create two types of 8-component surrogates. This approach leads to a greater precision in numerical results, but it is costly from a computational point of view in CFD simulations. In this way, the surrogate fuel simulates the physical and chemical characteristics of the target fuel to validate its engine performance. For this reason, a brief description is made of the effects of the physical and chemical properties of the diesel surrogate on the fuel spray, through a collection of results available from other work

5.2.3 Effects of physical and chemical properties of Diesel surrogate on fuel spray

The spray characteristics of n-octane, n-dodecane, n-hexadecane and their 3-component mixtures are analyzed by Myong et al. who verified how the components with a higher boiling point influenced the liquid phase length during the vaporization process.

The effects on the spray penetration behaviour for a mixture in different proportions of n-decane/1-methylnaphthalene are analyzed by Aye et al. The results showed that the decrease in the penetration distance and the increase in the spray cone angle are due to the addition of n-decane, which has a lower saturated vapor pressure. The spray and combustion processes of multi components surrogate are studied by Zhang et al and the results showed that the components with larger molecules are mostly distributed around the spray beam. The n-heptane is considered as one of the basic reference components for diesel, in particular Curran et al. constructed a detailed chemical reaction mechanism of n-heptane. The ignition delay behaviour of a selection of n-alkanes, including the n-heptane investigated in the work of Shen et al, is the same over a wide range of pressure and temperature [50].

5.3 Diesel Surrogate Validation

The target fuel data used to validate the surrogates derives from the ECN platform, which is the traditional diesel fuel, indicated as D2, whose properties are shown in Table 5-2

Fuels	D2
Type	No.2 Diesel
T_{10} [°C]	211
T_{50}[°C]	315
T_{90}[°C]	350
Cetane number	46
Lower Heating Value [MJ/kg]	42.975
Density at 15°C	843
C/H mass ratio	6.53
Stoichiometric Air/Fuel ratio	14.47
Aromatics volume %	27
Sulfur [ppm]	9
Kin. Visc. (-20°C) [mm²/s]	-
Kin. Visc. (40°C) [mm²/s]	2.35
Freeze Point [°C]	-
Flash Point [°C]	73

Table 5-2 D2 properties

The distillation curve was determined using a linear interpolation from three given point, indicated as $T_{10,50,90}$, which represent the volume fraction evaporated at the correspondent temperature. In this work the following list of hydrocarbons has been considered as candidate componds:

- N-hexadecane $C_{16}H_{34}$,*nC16*
- N-dodecane $C_{12}H_{26}$,*nC12*
- Toluene C_7H_8, *TOL*
- P-xylene C_8H_{10},*PX*
- Propylbenzene C_9H_{12},*PBZ*
- 2,2,4,4,6,8,8-heptamethylnonane $C_{16}H_{34}$, *HMN*

Three different mixtures have been investigated. The first is based on the work of Carr et al. [51] which consider a binary mixtures of n-hexadecane straight-chain alkane and toluene, an alkyl-aromatics, in this work it is labelled as “NS1”. The second is based on the work of Pei et al. [52], which consider a fixed volume composition of 77% of n-dodecane and 23 % of P-Xylene, which is labelled in this work as “NS2”. The third mixture is composed by the n-alkanes, n-dodecane, the iso-alkanes 2,2,4,4,6,8,8-heptamethylnonane, and the alkylbenzene, n-propylbenzene and it is labelled as “D2 surrogate”.

The compositions of the D2 surrogate and the NS1 surrogate have been determined using the algorithm described above, the results are shown in the Table 5-3

NS1	**N-hexadecane**	**Toluene**	**-**
[%vol]	53.2%	46.8%	-
NS2	**N-dodecane**	**P-Xylene**	**-**
[%vol]	77 %	23%	
D2 surr	**N-dodecane**	**HMN**	**N-propylbenzene**
[%vol]	52.01%	22.98%	25%

Table 5-3 Surrogates Compositions

Finally, the properties target for the three surrogates are determined with the estimation methods, listed in the Table 5-1, based on the volume, mass and molar fractions of each compounds.

Property	**D2 surrogate**	**NS1**	**NS2**
Cetane number	46.45	56	59
Density [kg/m³]	782.86	817.524	775.3
C/H mass ratio	6.51	9.08	7.052
LHC [MJ/kg]	43.35	42.28	43.36

Table 5-4 Surrogates Properties

Yaws equations [53], which allow to highlight a linear behavior between the investigated property and the temperature have been considered to estimate the individual physical properties of liquid phase surrogates. To assess the potential of the surrogates mixtures, a comparative analysis of the majors physical properties with respect to the D2 target Diesel fuel is carried out. The investigated mixtures have a different behaviour at different temperatures. In addition the mains properties for each component are listed in the Table 5-5

Property	**HMN**	**nC12H26**	**PBZ**	**nC16**	**TOL**	**PX**
Cetane number	14.7	74	16	100	6	7
Density [kg/m³]	778.25	751.89	868.4	774	867	860
C/H mass ratio	5.651	5.543	9.008	5.651	10.5	9.6
LHC [MJ/kg]	44.07	44.21	41.29	43.952	40.58	40.86
Molecular weight	226.44	170.338	120.194	226	92	106.16

Table 5-5 Components properties

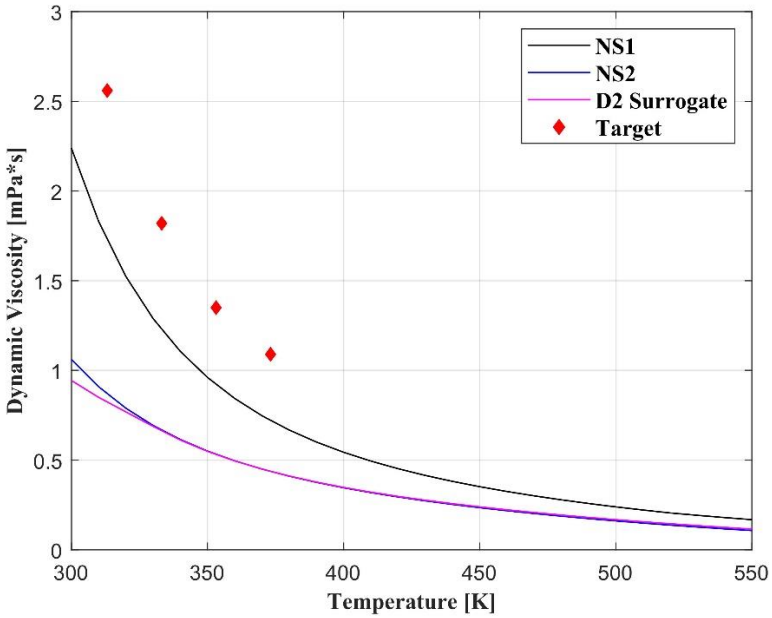

Figure 5-5 Dynamic Viscosity

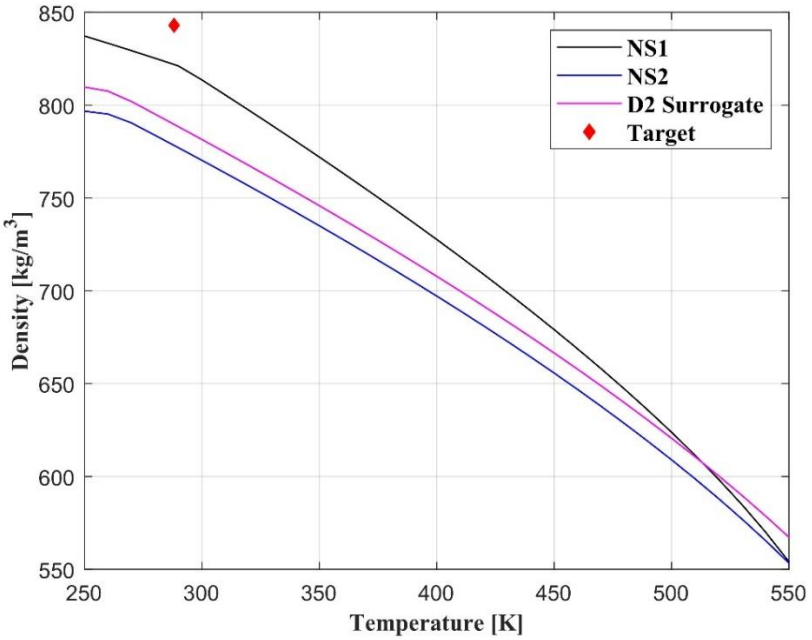

Figure 5-6 Density

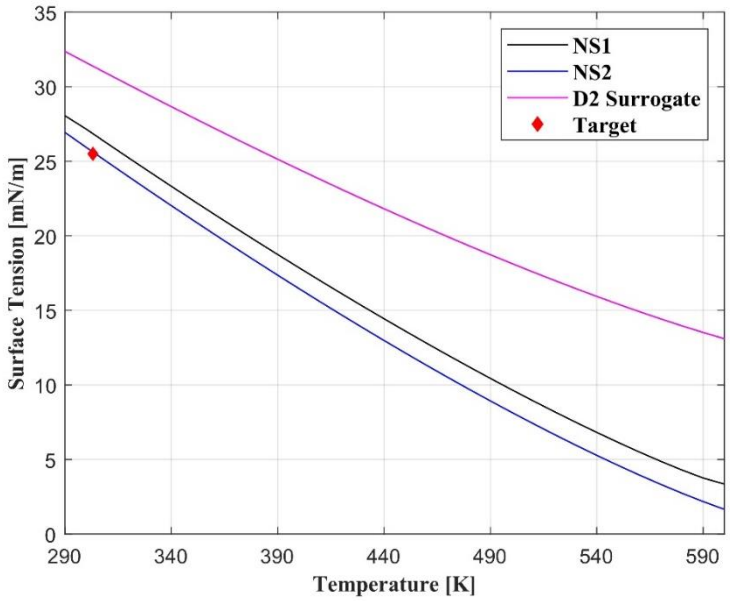

Figure 5-7 Surface Tension

From the Fig. 5-5, 5-6 and 5-7, the NS1 surrogate shows a good results in terms of density and dynamic viscosity compared to the other surrogates investigated

In conclusion, the resulting distillation points and the experimental distillation curve for the Diesel fuel target are represented in Fig. 5-8:

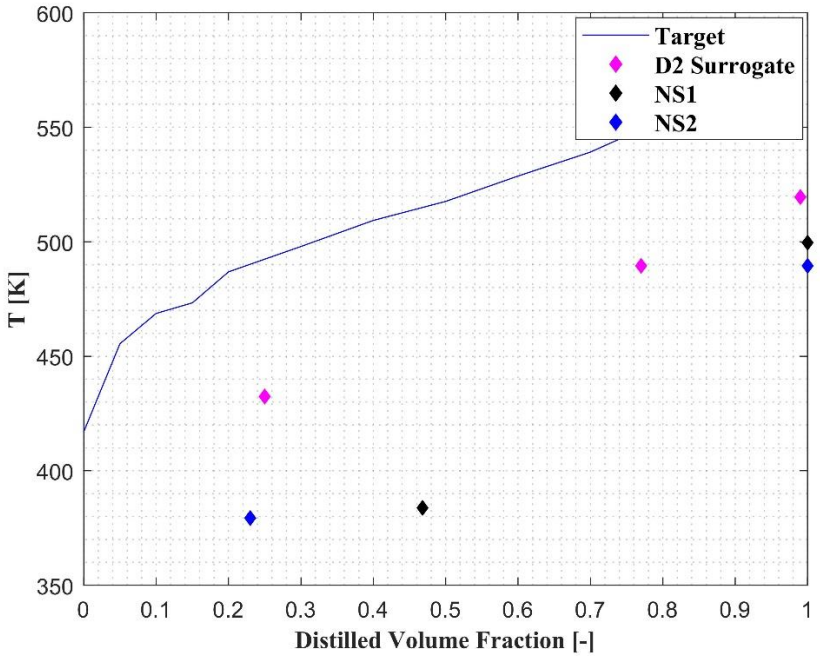

Figure 5-8 Distillation Curve

Due to the absence of a chemical kinetic mechanism in CFD code available for the surrogate NS1, the resulting surrogates used in this work are D2 surrogate and NS2, for the latter the chemical kinetic mechanism is used by the Lawrence Livermore National Laboratories [54] which has given the chance to develop and analyze new more specific surrogates for Diesel fuel.

The resulting mixtures are implemented in the numericals simulations to reproduce the experimental data obtained from the Engine Combustion Network (ECN) platform. Two reacting cases are simulated, in which the ambient gas density is varied from 14.8 to 30 kg/m³

6 Spray Injection Simulation

6.1 Experimental Data

Numerous institutions, like the Sandia National Laboratories, the Argonne National Laboratory and the CMT-Motores Termicos collaborate with the Engine Combustion Network, ECN, which is an international patnership among experimentals and computationals research in engine combustion. In this way, it is possible to collect and share experimental data, diagnostical and computational results. [55]

The investigation of the diesel combustion was carried out in a precisely defined vessel, a costant volume combustion, which can be simulated the spray injection behaviour over a wide range of conditions, usually based on the experience in diesel engines: [55]

- Ambient gas oxygen concentrations from 0 % to 21%
- Ambient gas temperatures from 300 K to 1400 K
- Ambient gas densities from 7.3 kg/m³ to 60 kg/m³

From the Fig. 6-1, a schematic cross-section of the vessel is shown

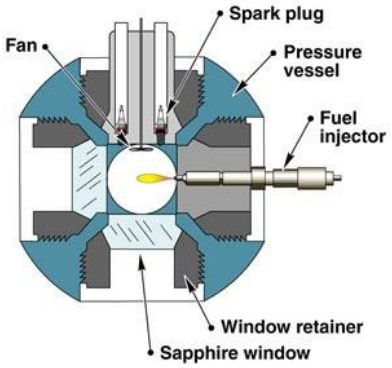

Figure 6-1 Schematic cross-section of the combustion vessel

The vessel has cubic shape, which dimension is 108 mm. Each side of the combustion chamber consists of a round port with a diameter of 105 mm. The fuel injector is positioned in one side port using a metal insert which constitutes the right wall of the combustion chamber, Fig.6-2. The top wall of the combustion chamber is composed by two spark plugs (mounted in another metal insert) and a mixing fan. [55]

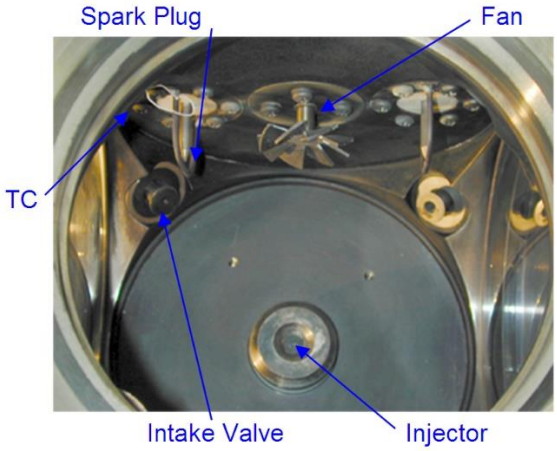

Figure 6-2 A picture of the inside of the combustion vessel

A consistent combustion in the high-density fuel lean environment is provided by the two spark plugs. The uniform ambiental conditions at the time of the injection is provided by the mixing fan, which operated at 8000 rpm. In addition, an optical access is provided by four sapphire windows with a dimensions of 102 mm located in the other four ports

The experimental procedure involves first filling the vessel with a lean, premixed, fuel-gas mixture to a desired pressure. After, the gas-mixture is spark-ignited and burned to create a high-temperatures and high-pressures conditions into the chamber. The heat transfer to the walls of the chamber and the mixing fan provides to cool the gas mixture and reach the desired ambiental conditions. Finally, the fuel injector is triggered, so the autoignition and combustion can begin. [55]

The vessel characteristics are summarised in the following table:

Characteristics	Units	Value
Width of the cube	mm	108
Window aperture	mm	102
Chamber volume	cm^3	1150
Injector position	-	Side windows
Mixing fan position	-	Upper corner (opposite injector)
Fan speed	rpm	1000-8000
Sprak plugs positions	-	Top window
Body temperature	K	461

Table 6-1 Vessel characteristics

The ECN working group has identified a few experimental conditions that will be the focus of modelers and experimentalists, in fact the experimental collaboration is made possible thanks to the donation of “indentical” injection system by Robert Bosch LLC. The ECN working groups offers a set of experimental conditions called “Spray A” for single-hole nozzle and “Spray B” for three-hole nozzle. In particular, the “Spay A” condition is a low-temperature combustion condition pertinent to engines that use moderate EGR. [55]

Specifications for Spray A operating condition of the Engine Combustion Network[1]	
Ambient gas temperature	900 K
Ambient gas pressure[2]	near 6.0 Mpa
Ambient gas density	22.8 kg/m³
Ambient gas oxygen (by volume)	15% O_2 reacting; 0% O_2 non-reacting
Ambient gas velocity	Near-quiescent, less than 1 m/s
Common rail fuel injector	Bosch solenoid-activated, generation 2.4
Fuel injector nominal nozzle outlet diameter	0.090 mm
Nozzle K factor	K= $(d_{inlet} - d_{outlet})$/10 [use μm] = 1.5
Nozzle shaping	Hydro-eroded
Mini-sac volume	0.2 mm³
Discharge coefficient	C_d=0.86, using 10 MPa pressure drop and diesel fuel
Number of holes	1 (single hole)
Orefice orientation	Axial (0&deg full included angle)
Fuel injection pressure	150 MPa (1500 bar), prior to start of injection
Fuel	n-dodecane[3]
Fuel temperature at nozzle[4]	363 K (90°C)
Common rail[5]	GM Part number 97303659. Used by 2005-2006 Duramax engines.
Common rail volume/length	22 cm³/28 cm
Distance from injector inlet to common rail	24 cm
Tubing inside and outside diameters[6]	Inside: 2.4 mm. Outside: 6-6.4 mm.
Fuel pressure measurement	7 cm from injector inlet / 24 cm from nozzle
Injection duration	1.5 ms
Injection mass	3.5 – 3.7 mg
Approximate injector driver current	18 A for 0.45 ms ramp, 12 A for 0.345 ms hold

From the full optical access, it is possible to use different experimental diagnostic such as: Schlieren imaging, mie-scattering and laser extinction that can be used for vapor and liquid penetration. The ignition delay and lift-off length are evaluated as well with a light-based model that measure the chemiluminescence.

[1] From SAE Paper 2010-01-2106

[2] This exact combination of ambient pressure and density corresponds to a particular set of gases for a 0%-O2 condition with 89.71% N2, 6.52% CO2, and 3.77% H2O by volume and a compressibility factor, Z = 1.01. When different gases are used, the pressure must vary to maintain the same density

[3] Chosen as a fluorescence-free diagnostics fuel with known chemistry and properties. Other fuels may be selected after initial study and comparison.

[4] Measured upstream of the orifice, at the time that injection would take place, from the SAE Paper 2010-01-2106. May be slightly different than injector body temperature, and different than the steady state temperature.

[5] Use rail outlet farthest away from fuel entrance (small orifice) to rail (i.e. cylinder #1)

[6] This 24 cm tube is available for purchase from USUI, reference part number IFP1. It is rated for 2500 bar

6.2 Experimental Condition

The ambiental conditions inside the vessel have been varied by the ECN data to assess the characteristics of the Diesel spray and combustion. In particular, the experimental tests have been performed varying the ambient gas density inside the combustion chamber, so it is possible to determine the following cases:

- Low ambient density
- High ambient density

Case	Base Case: Low density	Base Case: High density
Fuel type	D2	
Nozzle	Spray A, nozzle hole= 0.1 mm, single hole injector	
Ambient conditions	Temp=850 K ρ=14.8 kg/m³ Pressure=3.58 MPa O_2=21%; N_2=69.33%; CO_2=6.11%; H_2O=3.56% [molar fraction]	Temp=850 K ρ=30 kg/m³ Pressure=7.34 MPa O_2=21%; N_2=69.33%; CO_2=6.11%; H_2O=3.56% [molar fraction]
Injection conditions	Inj. Press=140 MPa; Inj. duration=4.9 ms; C_d=0.8	Inj. Press=140 MPa; Inj. duration=4.78 ms; C_d=0.8
Fuel condition	T_f=436K	T_f=436K
Ignition delay	1.19 ms	0.56 ms
Lift-Off length	40.6 mm	18.31 mm

Table 6-2 Experimental conditions for high and low ambient density

The fuel chosen is a standard #2 disel fuel, D2, whose characteristics are described in previous section (expressed in the following table:

Property	D2
Cetane number	46
Density [kg/m³]	843
C/H mass ratio	6.53
Low. Heating Val. [MJ/kg]	42.975
Molecular weight [g/mol]	199.9

Table 6-3 D2 property

6.3 D2 surrogate Numerical Simulation

The two experimental cases were performed on CONVERGE, using first the D2 surrogate

The Table 6-4 summarises the case setup conditions for the two cases analysed

Case	Base Case: Low density	Base Case: High density
Ambient pressure [Pa]	3580000	7340000
Ambient temperature [K]	850	850
Ambient composition	O_2=22.8%; N_2=65.89%; CO_2=9.12%; H_2O=2.17% [mass fraction]	
Injection conditions	Start of injection=0 s; Injection duration=0.0049 s, C_d=0.8	Start of injection=0 s; Injection duration=0.00478 s, C_d=0.8
Total injected mass [kg]	1.35e-05	1.365e-05
Fuel temperature [K]	436	
Nominal nozzle hole size [m]	0.0001	
Nominal nozzle length [m]	0.00115	
Sack diameter [m]	0.00094	
Spray cone angle [deg]	14.5	15.3
Embed scale	3	

Table 6-4 Low-density and high-density cases setup

In 1990, Hiroyasu and Arai have proposed an empirical equation for the calculation of the spray angle including some characteristics of the nozzle [56]:

$$2\theta = 83.5\left(\frac{l_0}{d_0}\right)^{-0.22}\left(\frac{d_0}{d_{sack}}\right)^{0.15}\left(\frac{\rho_g}{\rho_l}\right)^{0.26} \quad (6.1)$$

Where:

- l_0 the length of the nozzle
- d_0, the diameter of the nozzle
- d_{sack}, the diameter of the sack chamber
- ρ_g, gas density
- ρ_l, liquid density

From the Eq. 6.1 has been possible to calculate the spray cone angle. The characteristics of the nozzle have been considered, analyzing the work of Lyle M. Pickett, from the Sandia National Laboratories, in which the geometric characteristics of the nozzle are reproduced using a silicone mold [57]Finally the embed scale paramter define the embedded mesh size as expressed:

$$d_{x\_embed} = \frac{d_{x\_base}}{2^{embed\_scale}} \quad (6.2)$$

Where, d_{x_base}= 2 mm

6.3.1 Results

In this section, the ignition delay, which represents the time between the Start of injection and Start of Combustion, has been investigated as combustion indicator. From ECN platform, it is

possible to describe two differents definitions about of ignition delay, useful for its own determination [58]:

- Temperature rise: Time of maximum rate of rise of maximum temperature
- OH mass fraction: First time at which Favre-average OH mass fraction reaches 2% of the maximum in the domain after a stable flame is established.

The first definition has been chosen for this work. From the comparison between the trends of maximum temperature and CO mass and focusing on the time interval after which the trends have an exponential growth, it is possible to verify that the combustion has taken place. Unfortunately for the low ambient density case, the combustion process proceeds slowly, due to the reduced resistance of the gas in opposition to the liquid fuel jet. Therefore, the only Base Case: High Density was examined considering a threshold temperature of 1100 K.

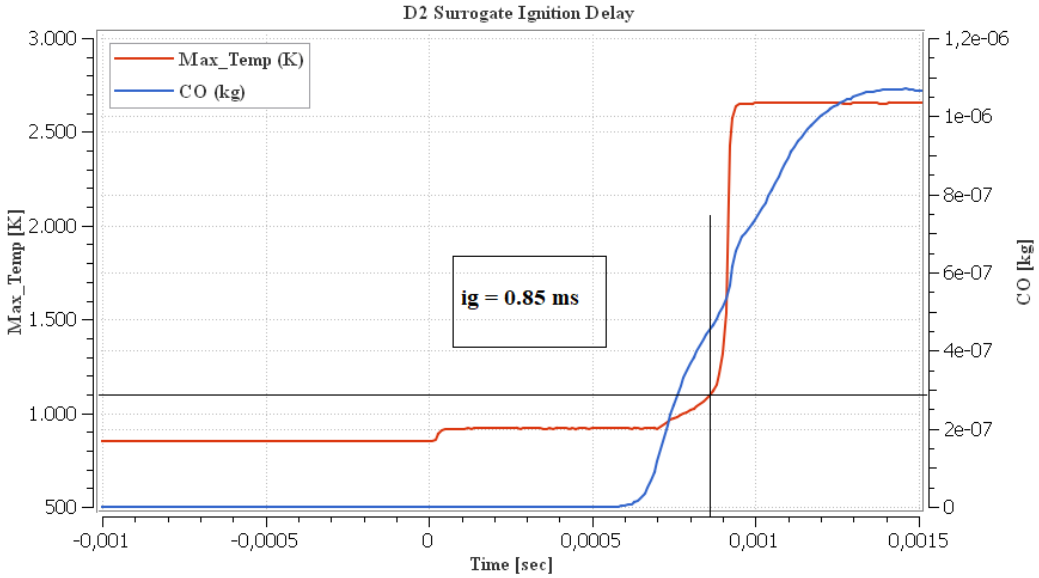

Figure 6-3 Ignition delay high density 30 kg/m³

From the Table 6-5, there is a remarkable difference between the experimental ignition delay and the numerical ignition delay for the Base Case: High Density. In fact the experimental ignition delay is smaller than the numerical ignition delay, it is necessary to reduce the latter through a recalibration process for the spray model

$\tau_{ig,experimental}$	$\tau_{ig,numerical}$	Percentual relative error [%]
0.56	0.85	51.78

Table 6-5 Ignition delay result: Base Case: High Density

6.4 Recalibration of the spray model for the D2 surrogate

6.4.1 Spray Break-up models

In a Diesel engine, the ignition delay represents the time interval (or crank angle) between the start of injection and the start of combustion. Both chemical and physical processes must take place before an important fraction of the chemical energy of the injected liquid fuel is released. The physical processes consist of the atomization of the liquid fuel jet, the vaporization of the fuel droplets and the mixing of fuel vapor with air. The chemical processes consist of the pre-combustion reactions of the fuel air, residual gas mixture which reach the autoignition. High cylinder air pressure, small injector hole diameter, optimum fuel viscosity and high fuel-injection pressure are required to obtain a good atomization. The rate of vaporization of the fuel droplets is influenced by the size of the droplets, their distribution, velocity, the pressure and the temperature inside the chamber and the volatility of the fuel. The rate of the fuel-air mixing is governed by the injector and the combustion chamber. The chemical delay is controlled by the precombustion reactions of the fuel. The Diesel engine combustion is heterogeneous, so the spontaneous ignition process is more complex. The ignition occurs into the vapor phase regions, the oxidation reactions may proceed in the liquid phase, between the fuel molecules and the oxygen that dissolves in the fuel droplets. In addition, cracking of large hydrocarbon molecules to smaller molecules is occurring. [8]

A conceptual model of the ignition delay period is shown in Fig.6-4. The physical delay portion of this model represents the time required for a fuel spray to leave the injector, form droplets and entrain hot air, vaporize, mix and achieve a critical temperature required for the onset of rapid chemical reactions. These processes may all be occurring simultaneously and are shown according to the properties of the fuel associated with them. The chemical delay represents the time required to initiate the chemical reactions that will lead to explosive chain branching also in this process, some fuel chemical properties that influence this step are shown in the Fig. 6-4 [48]

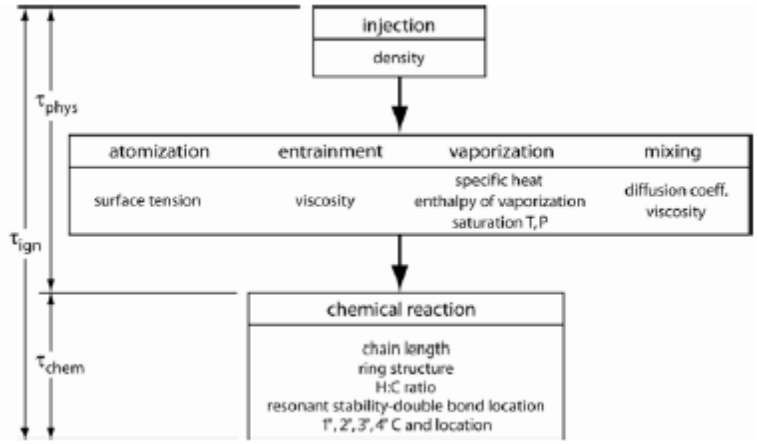

Figure 6-4 A conceptual model of ignition delay

The Kelvin-Helmholtz, Rayleigh-Taylor, and the hybrid model KH-RT are used for the atomization of the injected spray, and their implementations are considered in CONVERGE.

The “blob” injection model, based on the work of Reitz [59] and Reitz and Diwaker [60], is widely used in many Diesel applications. The large drops (blobs) with a diameter comparable to the size of the nozzle hole, are continuosly injected into the gas-phase, and the frequency of the new blobs is related to the fuel-injection rate, considering costant density of the liquid fuel and perfectly spherical blobs. Immediately after the injection region the Kelvin-Helmholtz model is applied, which describes the aerodynamic instabilities that growing on the droplet surface, it causes the generation of the smaller secondary droplets, cut from parent droplet surface, as shown in the Fig.6-5:

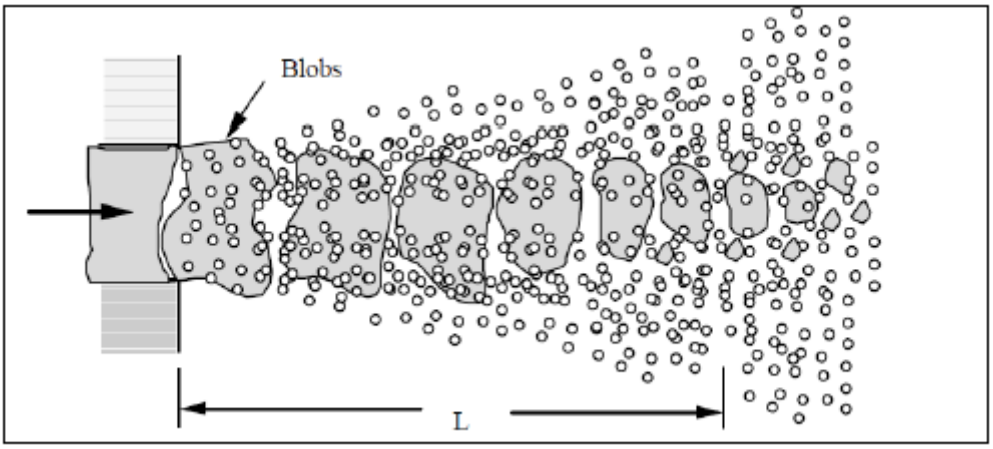

Figure 6-5 Illustration of the "blob" injection model

In accordance with the work of Reitz [59], the calculation of the resulting droplet radii is correlated with the fastest growing wavelength Λ and the maximum growth rate Ω, through the following Eq:

$$r_d = B_0 \Lambda \tag{6.3}$$

Where B_0=0.61, which is used to the description of the droplet “stripping” breakup regime characterized for the condition $25 < We < 50$

The original blobs are subjected to a reduction in size due to the breakup and the generation of small new droplets. The temporal change in radius of the parent drop in mathematical description is expressed as:

$$\frac{da}{dt} = -\frac{a - r_b}{\tau} \tag{6.4}$$

Where the breakup time τ, is given as:

$$\tau = 3.726 B_1 \frac{a}{\Lambda \Omega} \tag{6.5}$$

Where B_1, represents the time constant of the Kelvin-Helmholtz spray breakup model, and is introduced to account the internal flow effects of the nozzle flow on the breakup time. From the literature, Reitz [61] suggest a value of B_1 equal to 10, Xin et al. [62] suggest a value of B_1 equal to 40; and Senecal [38] equal to 39.6. So in the present work, the following range of variability has been considered for the Kelvin-Helmholtz Time Constant: $5 < B_1$ <40

Two adjustable constants are determined for the KH mechanism:

Mechanism	Size Constant	Time Constant
Kelvin-Hemholtz	B_0	B_1
Value	0.61	5~40

Table 6-6 Kelvin-Helmholtz constant

The Rayleigh-Taylor breakup model is used in conjunction with the KH model, to predict the secondary break-up of the droplets. The RT model suggest how the instabilities on the surface of the drop grows until a specific characteristics break-up time, then the drop finally break-up. In this model the frequency of the fastest growing wave is expressed as:

$$\Omega_{RT} = \sqrt{\frac{2}{3\sqrt{3\sigma}} \frac{\left[-g_t(\rho_f - \rho_a)\right]^{3/2}}{\rho_f + \rho_a}} \tag{6.6}$$

Where g is the acceleration into the direction of the travel, the wavelength, expressed as the Eq. 6.7, corresponding to the fastest growth rate is then compared to the radius of the droplet.

$$\Lambda_{RT} = \frac{2\pi C_{RT}}{K_{RT}} \tag{6.7}$$

Where K_{RT} represents the corresponding wave number.

If the wavelength is smaller then the radius of the drop, the waves of instability grow on the surface of the drop, in this condition the wave growth time is tracked, then this time is compared to the breakup time defined by the Eq. 6-8:

$$\tau_{RT} = \frac{C_\tau}{\Omega_{RT}} \tag{6.8}$$

Where C_τ is the time constant RT model, and it is expressed into this range of variability:

$$0.4 < C_\tau < 1$$

If the time where the Rayleigh-Taylor waves grows, is greater then the break-up time, the drop is subject to the break-up, and the radii of the new smaller droplets is expressed by :

$$r_c = \frac{\pi C_{RT}}{K_{RT}} \tag{6.9}$$

Where the size constant of the RT model, is labelled by C_{RT}, which is equal to a constant value of 0.1.

For the RT model, two adjustable constant were identified:

Mechanism	Size Constant	Time Constant
Rayleigh-Taylor	C_{RT}	C_τ
Value	0.1	0.4~1

Table 6-7 Rayleigh-Taylor constant

The Rayleigh-Taylor model is typically used in combination with the Kelvin-Helmholtz model, resulting in a hybrid model, called KH-RT model to describe the secundary droplet breakup. In this model, the KH and RT models are used in competing manners, focusing on the injector nozzle region, the RT model is predominant where the the velocities of the droplets are larger, while in KH model is implemented downstream.

Xin et al. [62] introduced the liquid break-up length concept to the hybrid model KH-RT. The break-up takes place in a different rate within and beyond the length of the liquid core, and the drops beyond the break-up length are influenced by the RT model. In according with the theory of Levich, this liquid break-up length is mathematical expressed by the following Eq.:

$$L_b = C_b d_0 \sqrt{\frac{\rho_f}{\rho_a}} \tag{6.10}$$

Where C_b, represents the brak-up length constant, which is an adjustable constant.

The disintegration of a parent droplet into several equal size product droplets is influenced by the RT model. The hybrid model KH-RT allows to consider the primary break-up of the injected drops with the KH instability model, while the secundary break-up is treated with the competing effects of the KH and RT mechanisms.

The last constant for the KH-RT hybrid was identified:

Mechanism	Length Size Constant
KH-RT	C_b
Value	1.5~20

Table 6-8 KH-RT constant

6.4.2 Recalibration process

The KH, RT and the hybrid model KH-RT are widely used for high-pressure diesel-fuel spray, the constants in the models are calibrated to predict the injection process, which is based on the injection condition, nozzle geometry and the fuel.
The simulation carried out for the spray calibration process, involving the “blob” injection method of Reitz and Diwakar. In accordance with this method the blob or parcel are injected into the computational domain with a characteristic size and velocity. The Kelvin-Helmholtz (KH), Rayleigh-Taylor (RT) instability mechanisms and the hybrid KH-RT model are used to simulate the breakup of the liquid blob and the generation of droplets in CONVERGE. The flowchart in Fig.6-6 summarizes the spray break-up models and the correnspondingvalues considered in this work:

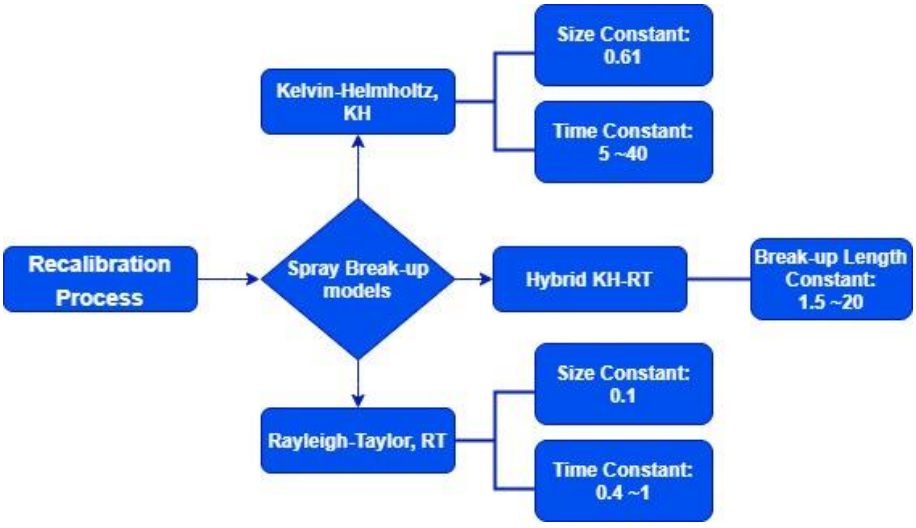

Figure 6-6 Spray Break-up models

In the recalibration process of the spray model, the effects on the spray breakup process resulting from variations in calibration parameters are analysed. The calibration cases are summarized in the following Table.

Simulation Case	KH time constant	KH size constant	RT time constant	RT size constant	RT breakup length	Ignition reached?
Base Case: High Density	7	0.6	1.0	0.1	-	YES
1	5	0.6	1.0	0.1	-	YES
2	7	0.6	0.8	0.1	-	YES
3	5	0.6	0.8	0.1	-	YES
4	10	0.6	1.0	0.1	-	YES
5	7	0.6	1.0	0.1	0.5	NO
6[7]	40	0.6	1.0	0.1	20	NO
7[8]	39.6	0.6	1.0	0.2	19.8	NO
8[9]	40	0.6	0.1	0.2	5.5	NO

Table 6-9 Simulation Cases

Unfortunately not all simulations performed reach the ignition conditions, only the following simulations are considered for the analysis of the recalibration process.

Simulation Case	Mechanism	KH time constant	KH size constant	RT time constant	RT size constant	RT breakup length
1	KH	5	0.6	1.0	0.1	-
2	RT	7	0.6	0.8	0.1	-
3	KH-RT	5	0.6	0.8	0.1	-
4	KH	10	0.6	1.0	0.1	-

Table 6-10 Final Simulation Cases

Spray characteristics, such as Sauter Mean Diameter (SMD), spray penetration, vapor penetration, spray parcel diameter, liquid spray mass, vapor mass, are chosen as the suitable metrics.

6.4.3 Effects on Spray Penetration

The effects of the KH, RT and KH-RT model's constant were performed to evaluate the effects on the spray penetration. The influence of the models on the spray penetration is shown in the Fig.6-6. In this way, the reduction of the time costant KH model shows a reduction of the 9 % compared to the Base case, similiar behaviour for the hybrid model KH-RT. Instead an increase in the time constant KH shows an increase of 30% compared to the Base case. The reduction of the time constant of the RT model, does not show any effect.

[7] From the work of Baele et al. [43]
[8] From the work of Senecal et al. [40]
[9] From the work of Xin et al. [62]

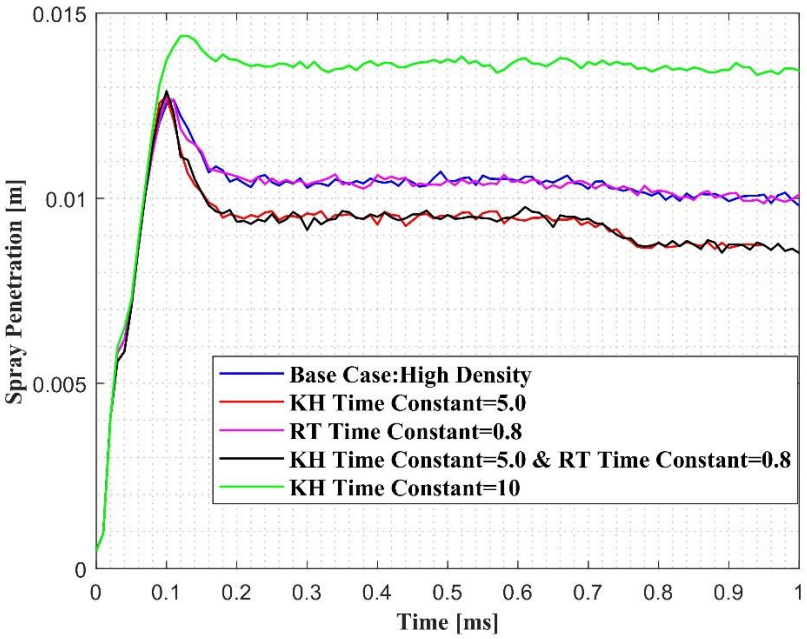

Figure 6-7 Spray Penetration Comparison

Similarly, analyzing the penetration distance from the nozzle output based on 90%, 95% and 99% respectively of the liquid mass, the same trend previously described is verified. In this case, reducing the time constant KH model and considering the hybrid model KH-RT, a reduction of about 9% compared to Base Case is verified in all analyses, with an increase of about 30% observed only in the case of an increase of the time constant KH. Once again, the reduction of the time constant RT model does not have any effect.

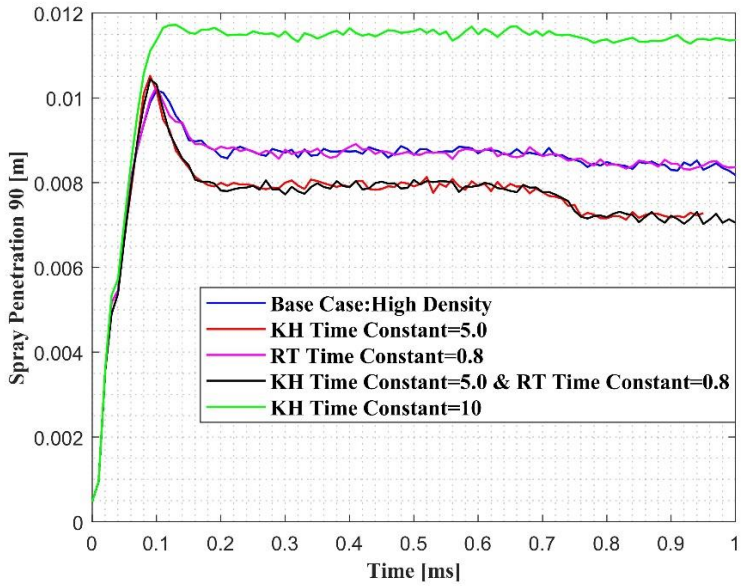

Figure 6-8 Spray Penetration based on the 90% of mass

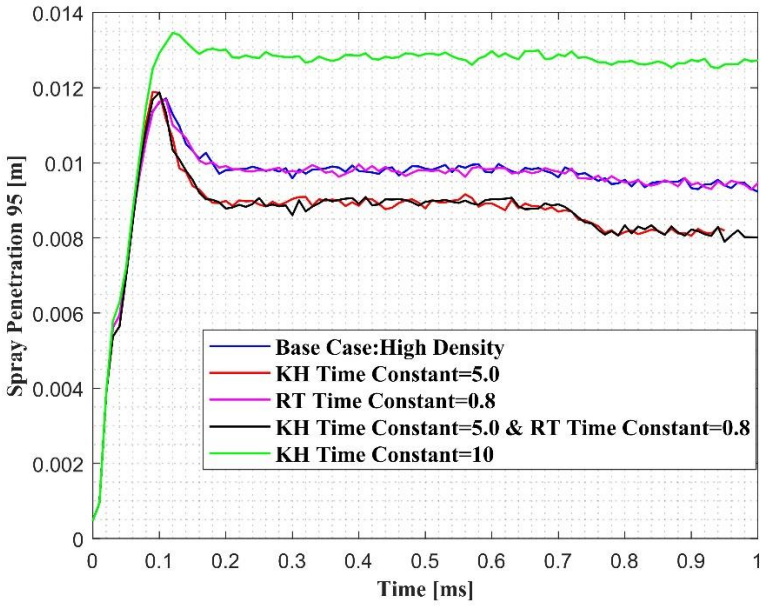

Figure 6-9 Spray Penetration based on the 95% of mass

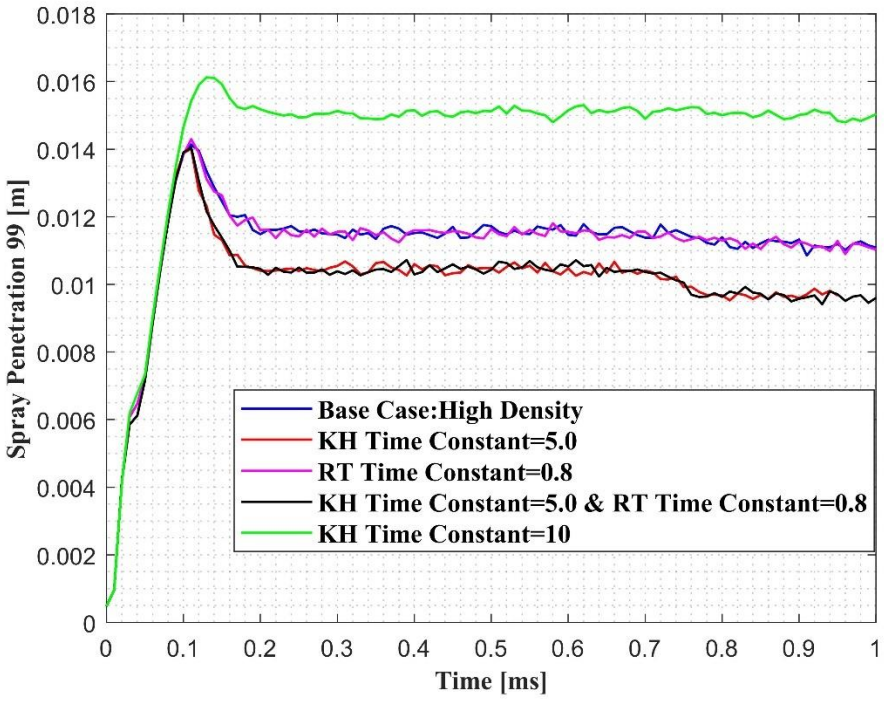

Figure 6-10 Spray Penetration based on the 99% of mass

The KH and KH-RT are predominant on the spray penetration focusing on the time constant parameter for the KH model, an increase of it causes an increase of the spray penetration and the momentum loss associated with atomization is delayed. A lower values for the breakup time

constant involve an improved atomization that occured earilier with its associated momentum loss.

6.4.4 Effects on the atomization process

In addition to the spray penetration, in the Fig.6-10, 6-11 are shown the results in term of mean diameter of drops based on the volume median particle size, DV50, and the ninetieth percentile by volume, DV90, at the end of the simulations. It is possible to evaluate how a variation of the time constant parameter of the RT model, does not involve any variation with respect to Base Case, according to the analysis on the spray penetration. While a significant reduction of about 40% is estimated in the DV50 analysis, by the reduction of the Time Constant KH model and the hybrid model KH-RT, the variation is reduced to about 7% in the DV90 analysis. Instead by increasing the Time Constant KH model, we can estimate an increase of about 1.5% for the analyses on DV50, while no effect was denoted for the DV90, denoting in this case a worsening of the atomization process compared to Base Case. Another important feature is the effect on the Sauter Mean Diameter, in which the minimum of it, involved an improvement on the atomization process.

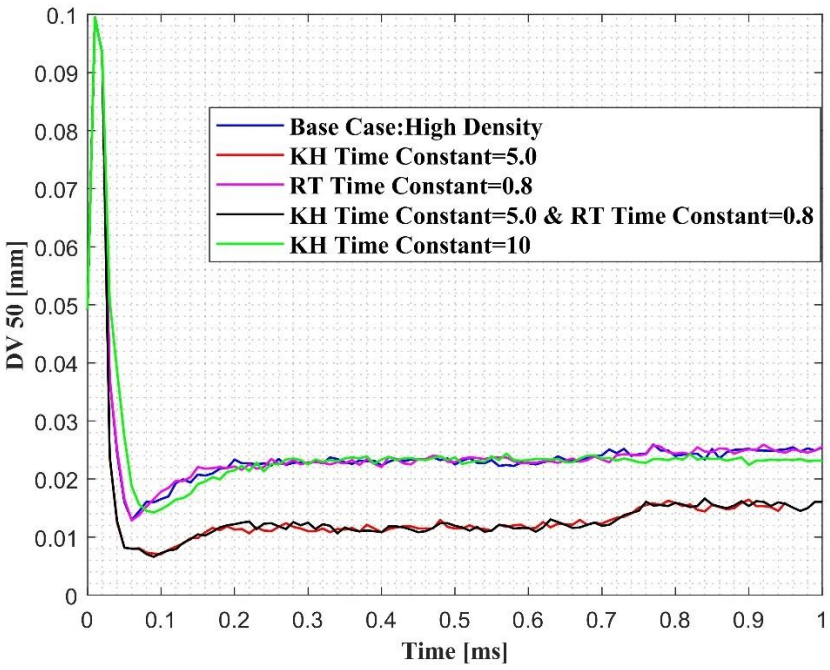

Figure 6-11 DV50

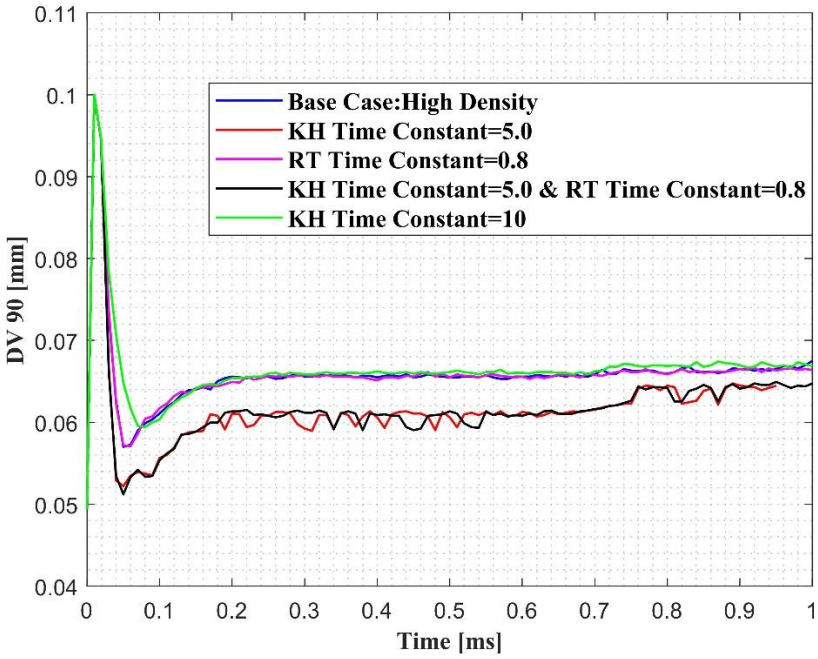

Figure 6-12 DV90

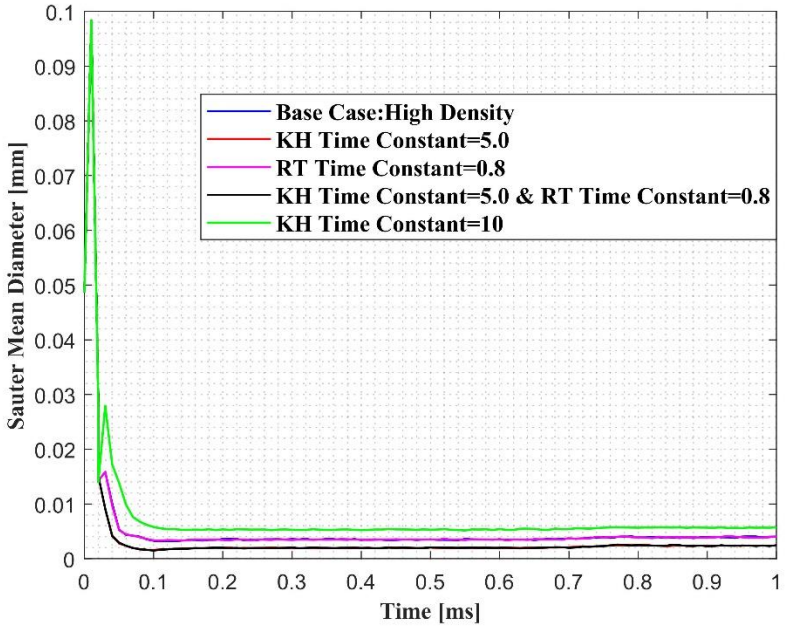

Figure 6-13 Sauter Mean Diameter

From Fig.6-13, reducing the Time Constant KH and considering the combination of KH and RT mechanisms, an effective improvement in terms of atomization has been achieved, evidenced by a reduction of about 40%, in terms of SMD compared to Base Case. This shows how the

recalibration process has led to an actual improvement over Base Case. Moreover the analysis on the SMD, verifies as the reduction of the Time Constant RT model does not have any effect on the recalibration process, while increasing the Time Constant KH model is evidenced a worsening of approximately 50% regarding the Base Case.

6.4.5 Results of the calibration process

In accordance with the analyses carried out, in the calibration process the best conditions are achieved in the KH mechanisms and in the hybrid model KH-RT. A reduction in the value of Time Constant KH model has a strong impact for the spray penetration and the atomization process, whose improvements compared to Base Case denote the effectiveness of the recalibration process. In this case, the best simulations are shown in the Table 6-11:

Best Simulation Case	Mechanism	KH time constant	KH size constant	RT Time constant	RT size constant
1	KH	5	0.6	1.0	0.1
3	KH-RT	5	0.6	0.8	0.1

Table 6-11 Optimum Calibration process

Although the atomization process has shown an improvement, for the two optimal cases, Case 1 and Case 3 there are no improvements in terms of ignition delay compared to Base Case, as shown in Table 6-12:

Simulation Case	Numerical Ignition delay [ms]
Base Case	0.85
1	0.88
3	0.87

Table 6-12 Ignition delay results

For this reason, the effect of the two optimal cases on the evaporation process of the drops should also be evaluated. In fact it denotes how comparing the vapor penetration (which represents the penetration distance from the nozzle exit for the current nozzle based on the 0.10% vapor mass fraction, shown in Fig. 6-13), and the vapor mass (Fig. 6-14), compared to Base Case, no effect is highlighted. This denotes how, in this case, the reduction of the KH Time Constant and the combination of the hybrid model KH-RT improve the atomization process but not the evaporation process.

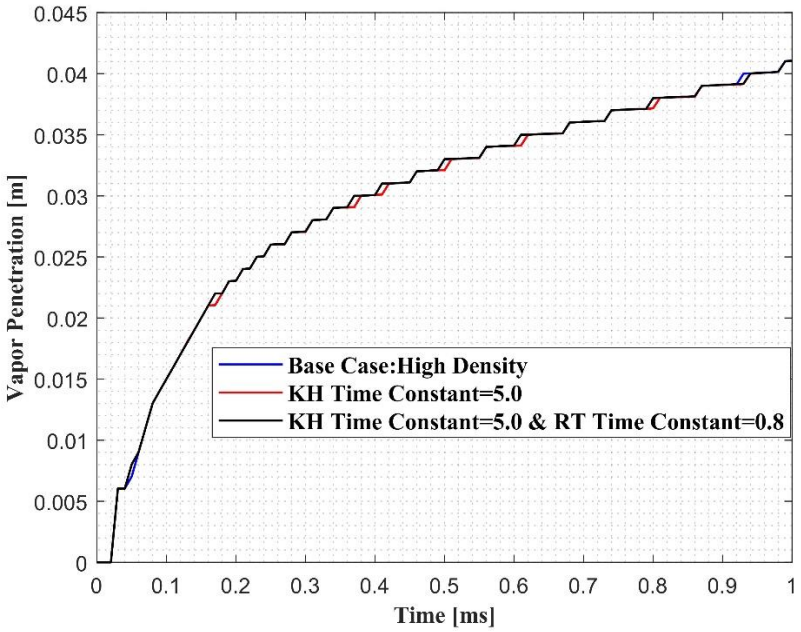

Figure 6-14 Vapor Penetration

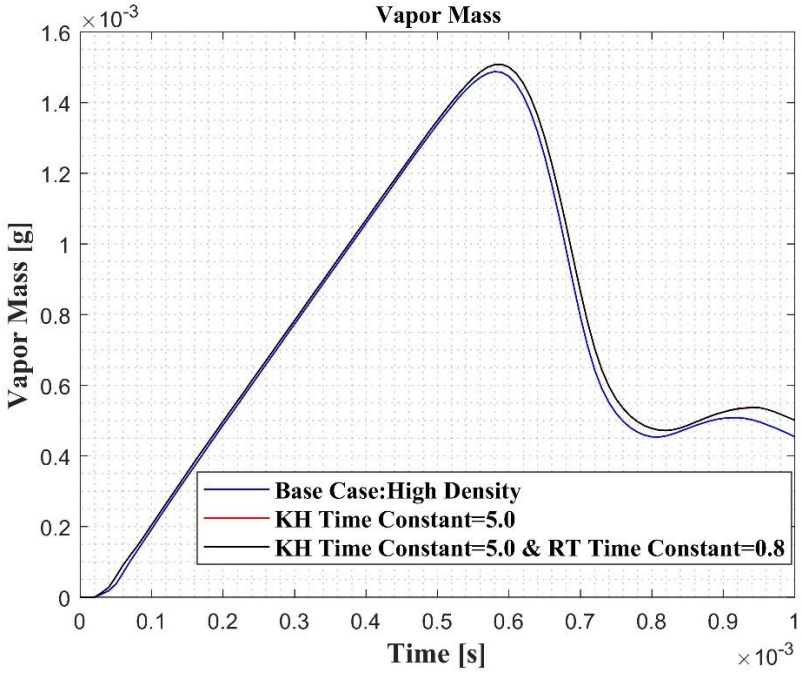

Figure 6-15 Vapor Mass

A worsening in terms of ignition delay, involves a physical problem, denoted by the evaporation process, as well as a chemical problem

6.5 NS2 Numerical Simulation

The experimental data for the high-density case, described in the section 6-4, was performed on CONVERGE using the mixture NS2. The ignition delay analysis returns the following result

$\tau_{ig,experimental}$	$NS2\tau_{ig,numerical}$	Relative error [%]
0.56	0.63	12.5

Table 6-13 Ignition delay result for NS2

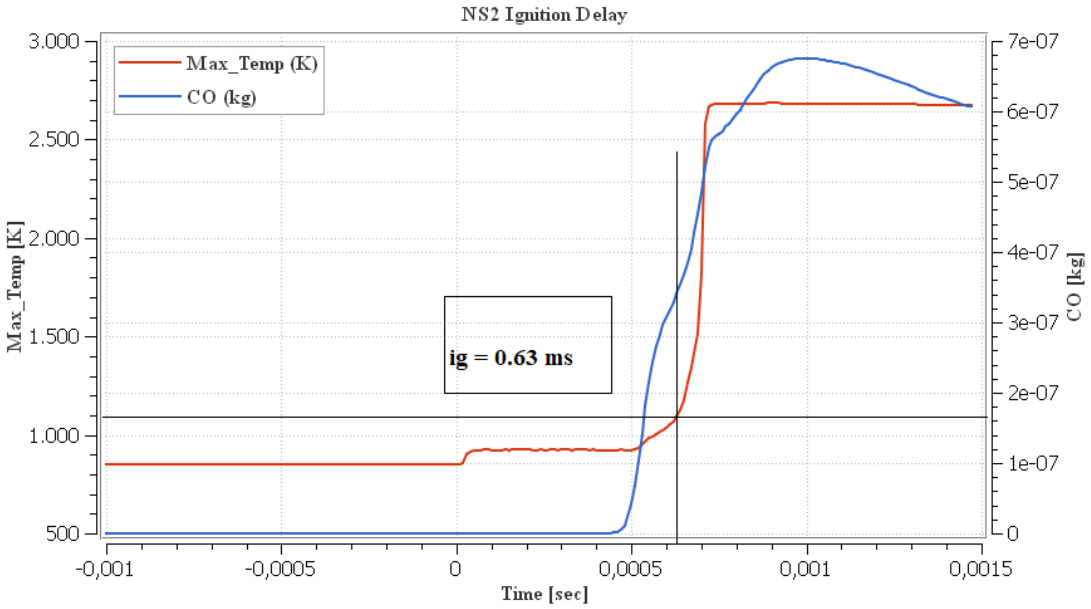

Figure 6-16 NS2 ignition delay

7 Test Engine Validation

In this section, the starting point is the description of the engine specifications and the operating point tested in this work, in addition a description of the initial conditions and various parameters used in CONVERGE are introduced in this work. Finally, the two Diesel surrogates, D2 surrogate and NS2, are tested on the sector geometry. The comparison between the two surrogate and the experimental data, was made in terms of:

- In-cylinder Pressure;
- Heat Rate Release;

7.1 Engine Specifications

The engine used in this work is the FPT F1A 2.3 L Euro VI light-duty diesel engine, the specifications are listed in the Table 7.1

Parameter	Units	Value
Number of cylinder	-	4
Bore	mm	88
Stroke	mm	94
Conrod length	mm	146
Crankshaft Offset	mm	0.5
Displacement	cm^3	2286.87
Compression ratio	-	17
Valves per cylinder	-	4
Intake Valve Closing (IVC)	deg	-140
Exhaust Valve Opening (EVO)	deg	110

Table 7-1 Engine Specifications

An eight-hole injector is located at the center of the cylinder bore, in which the combustion chamber is a bowl-in type. The simulation was carried out for a sector of 45° of the symmetrical piston, considering one eight of it. The schematic of the computational mesh used in this work, is show in the Fig. 7-1:

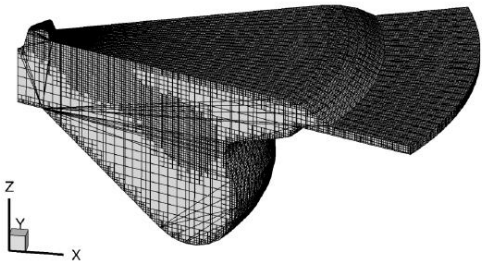

Figure 7-1 Computational mesh

The operating poitns in terms of engine speed versus load (expressed in break mean effective pressure, BMEP), are shown in the Fig. 7-2., in which the operating point tested in this work is:

- Operating point: 2000 [rpm] x 19 [bar]

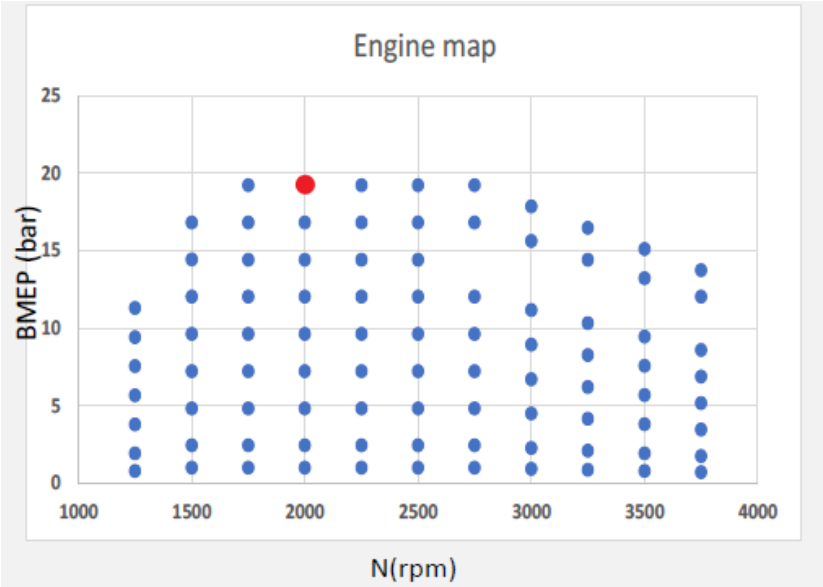

Figure 7-2 Engine operating point

The other experimental data for the operating point, used in CONVERGE are shown in the Table 7-2:

Parameter	Units	Value
Total trapped mass per cylinder at the IVC (air+EGR)	kg	0.0014
EGR mass fraction	%	7.14
Fuel rail pressure	bar	1213
Total fuel mass injected per cylinder	mg	61.36
Relative air-fuel ratio	-	1.32

Table 7-2 Experimental data for the operating point

7.1.1 In-Cylinder Pressure

The in-cylinder pressure curve is obtained by the Time Average Filter (TAF) procedure, which is used to filter the in-cylinder pressure signal during the test on the engine. This procedure is not included in this work of thesis. The in-cylinder pressure curve from IVC (-140 deg) to EVO (110 deg) is shown in the Fig. 7-3, and the maximum peak firing pressure at the operating point analyzed is 125.83 bar

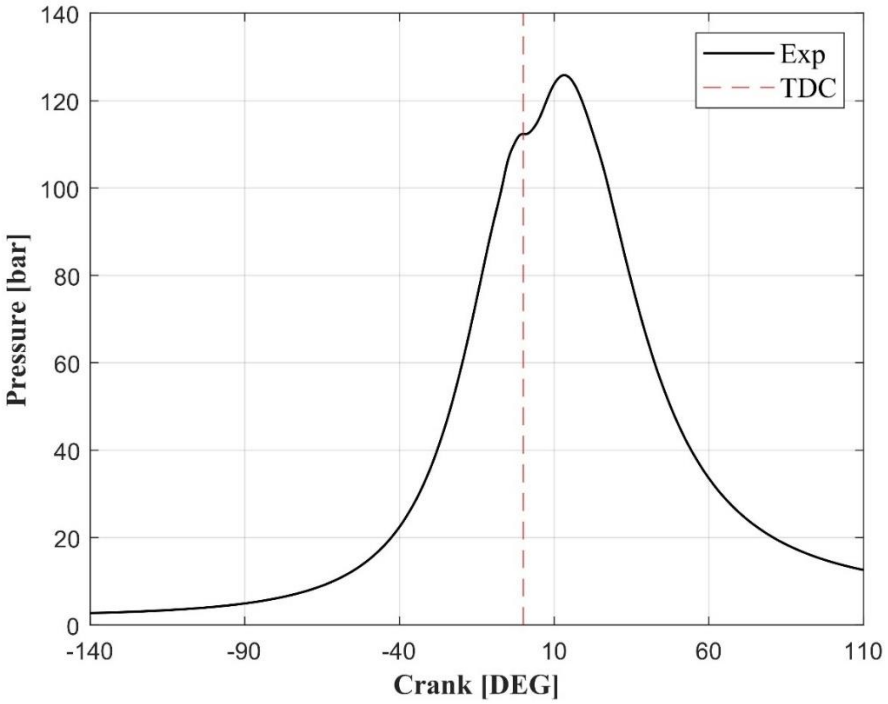

Figure 7-3 In-cylinder Pressure

7.1.2 Heat Release Rate

To determine the Heat Release Rate, HRR, the single-zone model is usually employed due to less complexity, and numerically more accurate accuracy than the multi-zone models. But the spatial variations are not included in the single-zone model, so the charge temperature and composition are assumed uniform. The effects are that the peak charge temperature is much lower than the actual peak burned gas temperature in the single-zone model. Other terms for work, such as the chemical energy changes and changes in sensible internal energy are always included in the models, while the additional terms as crevice volume, blowby, wall heat transfer, in-cylinder fuel injection mass and fuel enthalpy result in small effects for production engine so they can be neglected due to their minimal loss of accuracy. Also, the heat transfer from the charge to the wall is usually neglected for semplicity, so the result is labelled as the “Net Heat Release”, while the opposite case is known as “Gross Heat Release”. The “Net Heat Release” is usually 15% lower than the “Gross Heat Release” [63].

The traditional single-zone First Law equation to calculate the rate of heat release, is expressed in derivative form respect the distance, expressed in crank angle:

$$d\dot{Q}_{hr} = \frac{\gamma}{\gamma - 1} p \frac{dV}{d\theta} + \frac{1}{\gamma - 1} V \frac{dP}{d\theta} \tag{7.1}$$

Where, V is the cylinder volume, P is the in-cylinder pressure, θ is the crank angle and γ is the ratio of the specific heats.

The ratio of the specific heats varies with the composition and the charge temperature, it has a significant effect on the calculated of heat rate release energy. From an ideal point of view, the ratio would be varied with air fuel to rario, fuel specifications and exhaust gas recircolation (EGR), but in general gamma can be expressed as function with the mean in-cylinder temperature. [63]

In this work, the mean in-cylinder temperature at each crank angle is calculated using the perfect gas equation of state:

$$T = \frac{PV}{m_{air} R_{air} + m_{EGR} R_{EGR}} \tag{7.2}$$

Where m is the mass, and R is the gas constant

A relationship used for gamma, which was based on gasoline engine correlation, is used to calculate gamma in leaner mixtures used in diesel engines [63]

$$\gamma = 1.35 - 6.0 * 10^{-5} * T + 1.0 * 10^{-8} * T^2 \tag{7.3}$$

Where T is the mean in-cylinder temperature in Kelvin

The HRR curve for the operating point is shown from -20 CAD (before the start of injection) to 80 CAD (the HRR drops to zero around 70 CAD). The TAF procudure used to calculate the in-cylinder pressure and the neglibility of the in-cylinder fuel injection mass, crevice volumes, blowby involve an uncharacteristically smooth for diesel combustion

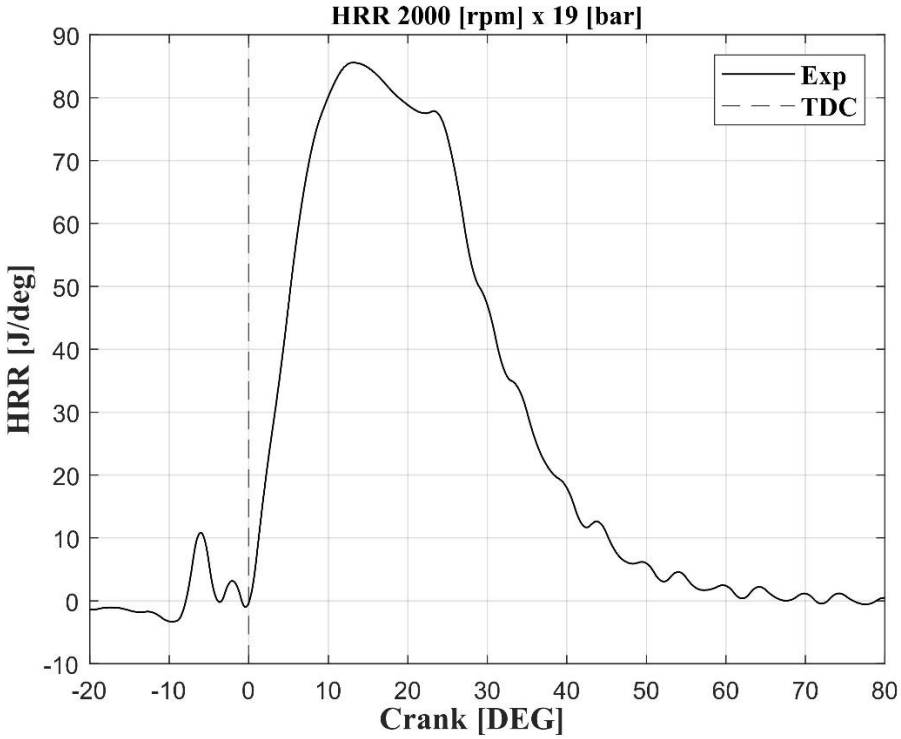

Figure 7-4 HRR

7.1.3 Injection parameter

The eperimental injection data are listed in the Table 7-3:

Parameter	Units	Value
Number of injection events	-	3 [Pilot1 (P1), Pilot2 (P2), Main (M)]
Injected mass (P1/P2/M)	mg	0.31/1.09/ 59.96
SOI (P1/P2/M)	deg	-23.2/-11.9/-3.2

Table 7-3 Injection parameter

The SOI defines the start of the electrical signal for the injector. The nozzle open delay (NOD) is determined by the experimental injection rate data, which value is 220 μs at 2000 [rpm]. The hydraulic start of injection can be calculated from the following formula:

$$SOI_{hyd} = SOI_{el} + \left(\frac{6 \cdot NOD \cdot n}{10^6}\right) \tag{7.4}$$

In the Fig. 7-5, the normalized injection rate is shown:

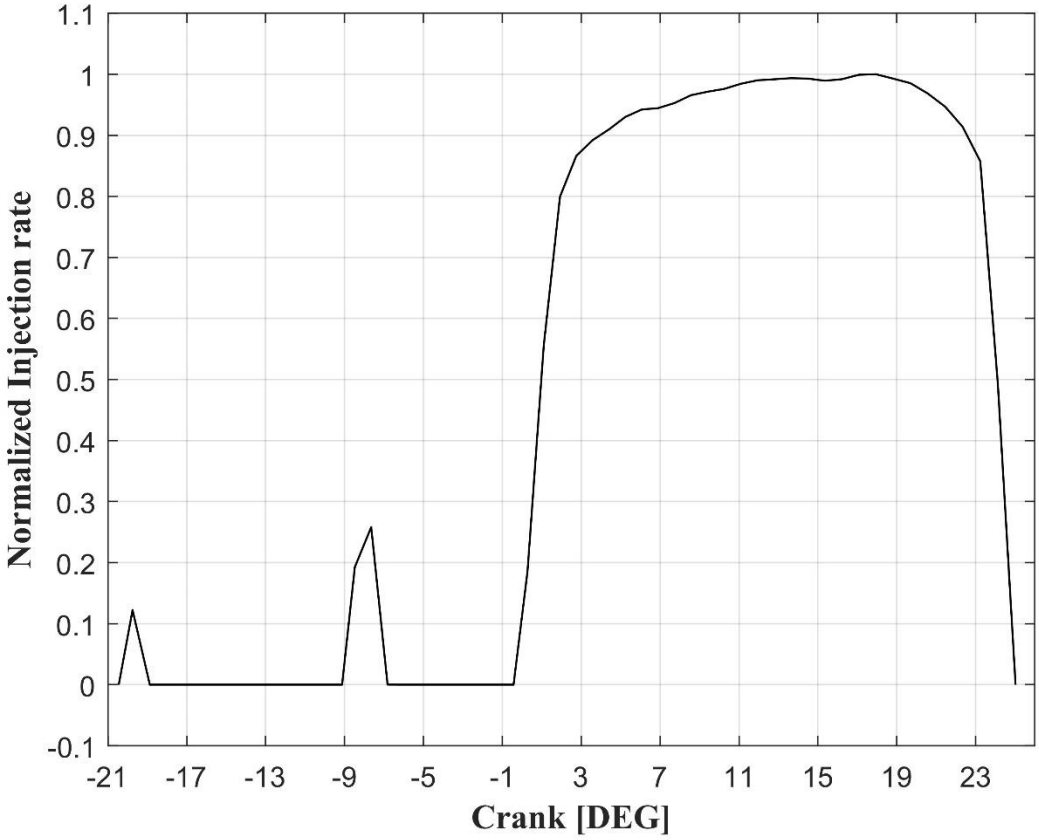

Figure 7-5 Normalized Injection Rate

7.1.4 Pollulant Emissions

The experimental values of NO_x, Soot, HC and CO are listed in the following table:

Parameter	Units	Value
NO_x	mg	1.22
Soot	mg	0.0071
HC	mg	0.0009
CO	mg	0.0058

Table 7-4 Emissions Data

7.2 Initial Conditions and Inputs

In this Section, the following conditions and inputs are described:

- Global Transport Parameters
- Boundaries
- In-cylinder region
- Inputs for Spray Modeling

7.2.1 Global Transport Parameters

The global transport parameters used in this work are:

- Turbolent Prandtl number
- Turbolent Schimdt number

The selected values are the follows:

Global Transport Parameters	Value
Turbolent Prandtl number	0.9
Turbolent Prandtl number	0.78

Table 7-5 Global Transport Parameters

7.2.2 Boundaries

In accordance with the terminology used in CONVERGE CFD, the boundaries of the computational domain are:

- Piston, represents the translating wall with the piston motion
- Head, whose boundary type is stationary wall
- Liner, whose boundary type is stationary wall
- Front Face, whose boundary type is periodic stationary with sector shape
- Back Face which is a periodic boundary

Except for the periodic boundaries, the temperature for each boundary is required. The mean surface temperatures are considered in the Table 7-6, in according to wide research:

Boundary	Units	Value
Piston	K	453
Head	K	433
Liner	K	388

Table 7-6 Boundaries

7.2.3 In-Cylinder Region

The in-cylinder pressure and temperature are calculated from the experimental data, in this work, the mean values of the experimental data for the pressure and temperature at the IVC were considered. The in-cylinder region parameters are listed in the following Table.

Parameter	Units	Value
Pressure	Pa	168500
Temperature	K	405.9
Turbolent kinetic energy	m^2/s^2	85.67
Turbolent dissipation	m^2/s^3	18532

Table 7-7 In-cylinder region

7.2.4 Inputs for Spray Modeling

The total number of injected parcels and the spray cone angle are listed in the Table 7-8.

Parameter	Units	Value
Total number of injected parcels	-	512000
Spray cone angle	°	15.4

Table 7-8 Inputs Spray Modeling

7.3 Surrogate Comparison

The two mixtures NS2 and D2 surrogate are compared with a traditional Diesel fuel on the sector geometry at the operating point 2000 [rpm] x 19 [bar]. From the Fig. 7-6, the pressure traces of the two surrogates grow rapidly starting from the IVC (-140 deg), accurately maintaining the compression stroke of the experimental curve

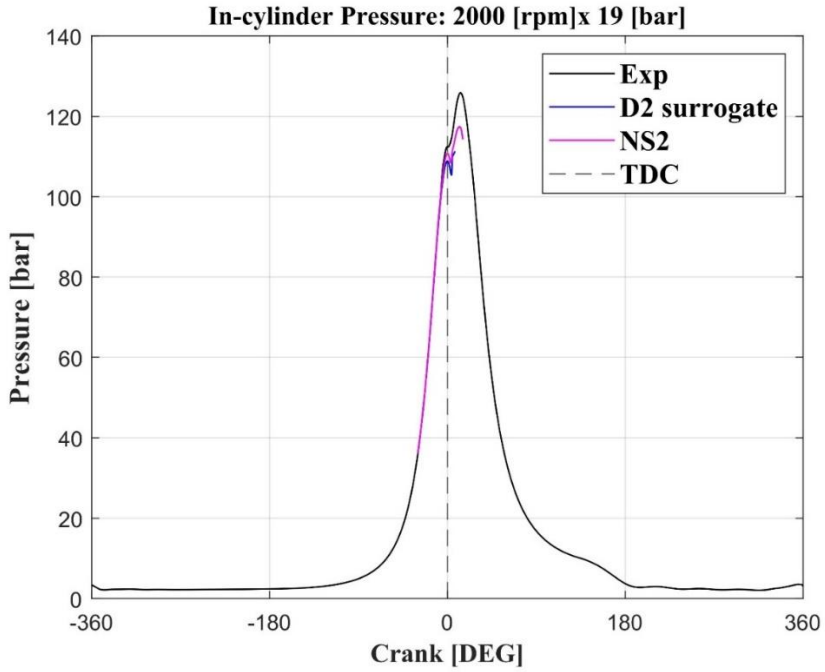

Figure 7-6 In-cylinder Pressure Comparison

From the Fig. 7-7, the D2 surrogate turns out to be little performing regarding the experimental case. Looking close to the PMS, the surrogate D2 underestimates the experimental pressure signal by about 3 % with a difference of about 3.41 bar. The in-cylinder pressure for the surrogate NS2, tends to follow the experimental pressure trace, however showing an understatement of 6 % compared to the experimental tract during the combustion process

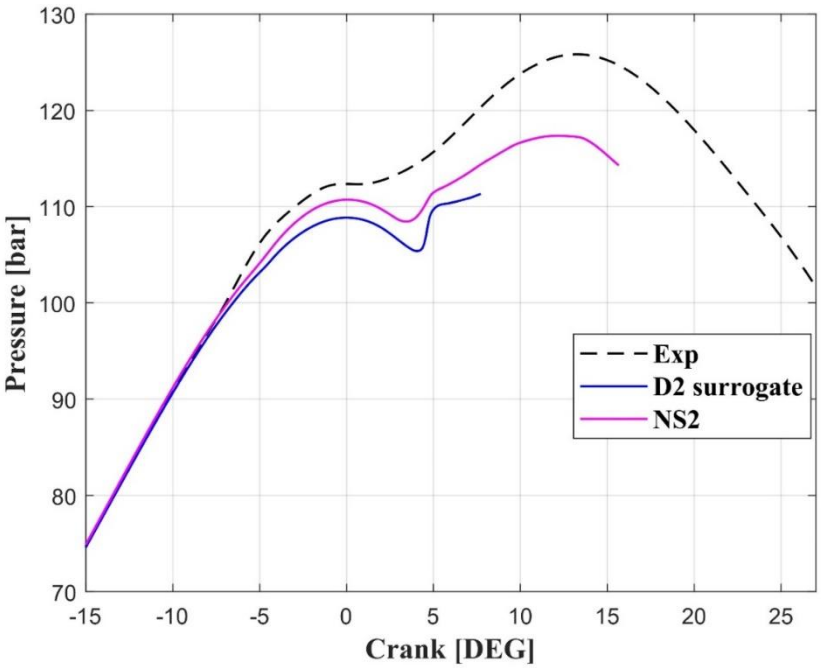

Figure 7-7 In-cylinder pressure comparison near the TDC

Observing the HRR, Fig. 7-8, the behaviour of the surrogates is totally variable regarding the experimental case. In particular, the ignition delay is evident compared to the P2 of the experimental case, respectively at -5.5 and -4.9 DEG for surrogates NS2 and D2 surrogates. The high-reactivity surrogate NS2 shows an effective reduction in ignition delay compared to the D2 surrogate by about 12 %. The HRR during the main injection, appears to underestimate the premixed phase of the experimental case. For the surrogate D2 there is an increase of HRR in the premixed phase of about 50 % compared to NS2, reaching a peak of 157 J/deg. This condition represents the effect of marked ignition delay for the two surrogates. During mixing controlled the two surrogates tend to follow the track of experimental HRR. Noting that in the case of NS2 there is an acceptable understatement of 2.4% compared to 17.8% of the surrogate D2

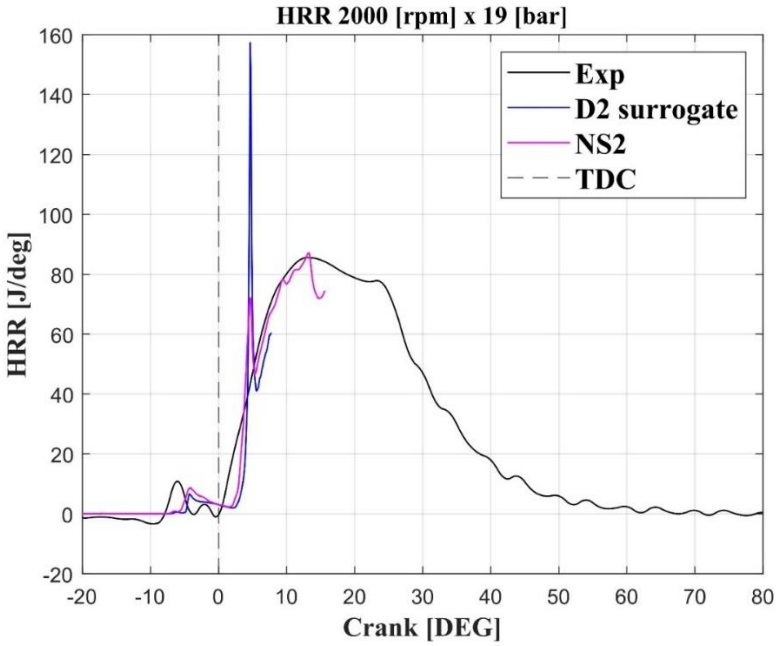

Figure 7-8 HRR Comparison

8 Conclusions

In the following thesis work, the numerical simulations were carried out on CONVERGE to analyze the characteristics of diesel spray and the combustion of surrogates capable of reproducing the chemical-physical properties of a traditional diesel fuel, such as D2. In addition the combustion behaviours for the surrogates D2 surrogate and NS2 have been analyzed by the sector geometry simulation for the F1A Diesel engine at the operating point 2000 [rpm] x 19 [bar]

The analysis showed that:

- The recalibration process for the surrogate D2 showed that Kelvin-Helmholtz and KH-RT spray break-up models are predominant in the spray penetration and atomization process
- The recalibration process carried out for the D2 surrogate did not lead to actual improvements in terms of ignition delay, denoting that the problem concerns the physical process of evaporation of fuel drops, and the chemical reaction process leading to the complete oxidation of the hydrocarbons in the fuel
- The increase in the Kelvin-Helmholtz Time constant showed worsening in terms of spray penetration rather than atomization, while the Rayleigh-Taylor mechanism showed no improvement for the same. during the recalibration process of the spray model
- The surrogate NS2 shows a higher cetane number (59) than the target diesel fuel D2 (46) and the surrogate D2 (46.45) and shows a higher reactivity, as well as a higher ignition tendency. Verifying the importance of the cetane number as an indicator parameter of the reactivity of a fuel in CI engines
- NS2 surrogate predicts in-cylinder pressure and HRR more accurately than surrogate D2. Therefore an appropriate calibration process could be carried out for this surrogate to assess its impact in terms of Soot and Nox emissions

The future steps to advance with the following project, will be the improvement of the physical and chemical properties for the NS2, such as the Low Heating Combustion, to assess its potential in terms of efficiency, performance and emissions of the engine, for which a 3D-CFD engine model is currently in phase of development with the DENERG research team of Prof. E. Spessa, Prof. D.A. Misul, Prof. M. Baratta and the Prof. P. Goel.

In addition, the investigation of the calibration process carried out for the D2 surrogate spray model could be more in-depth, to optimize the choice of the right calibration models, as well as the evaporation process of it. One of the possible objective to follow could be to monitor the effects in terms of ignition delay as conditions of the experimental environment variation.

Finally the process of validation of diesel surrogates will have to be improved, as well as extended to Biofuels of greater interest as the HVO

9 References:

[1] https://www.iea.org/reports/world-energy-outlook-2020.

[2] International Energy Agency, World Energy Outlook, 2018.

[3] H. Aatola, M. Larmi e T. Sarjovaara, *Hydrotreated Vegetable Oil (HVO) as a Renewable Diesel Fuel: Trade-off between NOx, Particulate Emission, and Fuel Consumption of a Heavy Duty Engine,* 2008 SAE International, 2008.

[4] G. Karavalakis, Y. Jiang, J. Yang e T. Durbin, *Emissions and Fuel Economy Evaluation from Two Current Technology Heavy-Duty Trucks Operated on HVO and FAME Blends*, SAE Int. J. Fuels Lubr. 9(1):2016, Riverside, 2016.

[5] K. Sugiyama, I. Goto, K. Kitano e K. Mogi, *Effects of Hydrotreated Vegetable Oil (HVO) as Renewable Diesel Fuel on Combustion and Exhaust Emissions in Diesel Engine*, SAE International, 2011.

[6] H. Pflaum, P. Hofmann, B. Geringer e W. Weissel, *Potential of Hydrogenated Vegetable Oil (HVO) in a Modern Diesel Engine*, SAE International, 2010.

[7] https://www.eni.com/it-IT/attivita/bioraffinerie.html.

[8] J. B. Heywood, *Internal Combuston Engine Fundamentals*, Mc-Graw Hill , 1998.

[9] Literature of Professor Millo.

[10] J. L. Lumley, *Engines. An Introduction*, Cambridge: Cambridge University Press, 1999.

[11] N. D. Wilson, A. J. Watkins e C. Dopson, *Asymmetric Valve Strategies and Their Effect on Combustion*, SAE Technical Paper Series 930821, Michigan, 1993.

[12] T. Kamimoto, H. Kobayashi e S. Matsuoka, *Big Size Rapid Compression Machine for Fundamental Studies of Diesel Combustion*, SAE 811004, Milwaukee, 1981.

[13] K. R. Browne, I. M. Partridge e G. Greeves, *Fuel Property Effects on Fuel!Air Mixing in an Experimental Diesel Engine*, SAE 860223, Michigan, 1986.

[14] B. Carsten, *Mixture Formation in Internal Combustion Engines,* Springer, Berlin, 2006.

[15] A. H. Lefebvre e V. G. McDonell, *Atomization and Sprays*, CRC Press, Boca Raton, 2017.

[16] P. B. Kowalczuk e J. Drzymala, *Physical meaning of the Sauter mean diameter of spherical particulate matter*, Taylor & Francis Group, Wroclaw, 2015.

[17] J. E. Dec, *A Conceptual Model of DI Diesel Combustion Bases on Laser-Sheet Imaging*, Sandia National Laboratories, 1997.

[18] J. E. Dec e C. Espey, *Ignition and Early Soot Formation in a DI Diesel Engine Using Multiple 2-D Imaging Diagnostics,* SAE 950456, 1995.

[19] J. Blazek, *Computational Fluid Dynamics: Principles And Applications*, ELSEVIER, 2001.

[20] https://it.wikipedia.org/wiki/Fluidodinamica_computazionale.

[21] A. J.D., *Computational Fluid Dynamics. The Basics with Applications*, New York: McGraw-Hill, 1995.

[22] J. D. A. Jr., J. Degroote, G. Degrez, E. Dick, R. Grundmann e J. Vierendeels, *Computational Fluid Dynamics An Introduction*, Belgium: A Von Karman Institute Book, Springer , 2009.

[23] D. A. A. R. H. P. John C. Tannehill, *Computational Fluid Mechanics and Heat Transfer*, Washington: Taylor & Francis Group, 1997.

[24] J. H. Ferziger e M. PeriC, *Computational Methods for Fluid Dynamics*, New York: Springer, 2002.

[25] W. e Richter, vol. No. 389, 1970, p. p. 200.

[26] https://www.treccani.it/enciclopedia/turbolenza.it

[27] B. R. Munson, D. D. Young, Okiishi e Theodore, *Fundamentals of Fluid Mechanics*, John Willey & Sons, 2006.

[28] http://www.lth.se/fileadmin/fm/Education/Courses/Combustion/Lect7_turbu.pdf.

[29] U. Frisch, P.-L. Sulem e M. Nelkin, *A simple dynamical model of intermittent fully developed turbulence*, Great Britain: Journal of Fluid Mechanics, 1978.

[30] E. Nobile, *Introduzione ai Modelli di Turbolenza in CFD*.

[31] G. Alfonsi, *Reynolds-Averaged Navier-Stokes Equations for Turbulence Modeling*, Università della Calabria, 2009.

[32] https://www.youtube.com/watch?v=fOB91zQ7HJU&t=1306s.

[33] : https://www.cfd-online.com/Wiki/RNG_k-epsilon_model.

[34] https://convergecfd.com/about/company-profile.

[35] https://convergecfd.com/applications/internal-combustion-engines.

[36] C. Science, *CONVERGE 2.4 Manual*, 2018.

[37] R. I. Issa, *Solution of the Implicitly Discretised Fluid Flow Equations by Operator-Splitting*, Academic Press, Inc., London , 1986.

[38] P. K. Senecal, K. J. Richards, E. Pomraning, T. Yang, M. Z. Dai, M. A. P. R. M. McDavid, S. Hou e T. Shethaji, *A New Parallel Cut-Cell Cartesian CFD Code for Rapid Grid Generation Applied to In-Cylinder Diesel Engine Simulations*, SAE International, USA, 2007.

[39] Turns e S.R., *An Introduction to Combustion*, McGraw-Hill, Inc., 1996.

[40] P. K. Senecal, E. Pomraning e K. J. Richards, *Multi-Dimensional Modeling of Direct-Injection Diesel Spray Liquid Length and Flam Lift-off Length using CFD an Parallel Detailed Chemistry*, SAE 2003-01-1043, 2003.

[41] F. d. Santos e L. L. Moyne, *Spray Atomization Models in Engine Applications, from Correlations to Direct Numerical Simulations*, IFP Energies nouvelles, 2011.

[42] *Best Practice Guidlines Computational Fluid Dynamics of Turbolent Combustion*, ERCOFTAC, 2015.

[43] Beale e Reitz, *Modeling Spray Atomization with the Kelvin-Hemholtz/Rayleigh-Taylor Hybrid Model*,Begell House, Inc, 1999.

[44] M. Mehl, *An Approach for Formulating Surrogates for Gasoline with Application toward a Reduced Surrogate Mechanism for CFD Engine Modeling*, ACS Publications, 2011.

[45] E. T e M. LQ, *Surrogate mixtures to represent complex aviation and rocket fuels*, 17:461-466., 2001.

[46] Y. Ra e R. D. Reitz, *Effects of Fuel Physical Properties on Diesel Engine Combustion using Diesel and Bio-diesel Fuels*, SAE International, 2008.

[47] B. Kerschgens, *Surrogate fuels for the simulation of diesel engine combustion of novel biofuels*, Internation Journal of Engine Research , 2014.

[48] M. A. Carr, *An Experimental And Modeling-Based Study Into The Ignition Delay Characteristics Of Diesel Surrogate Binary Blend Fuels*, ICEF2011-60027, Morgantown, West Virginia, USA, 2011.

[49] A. Li, L. Zhu, Y. Mao, J. Zhai, D. Han, X. Lu e Z. Huang, *Surrogate formulation methodology for biodiesel based on chemical deconstruction in consideration ofmolecular structure and engine combustion factors*, ISSN 0010-2180, 2019.

[50] Y. Qian, L. Yu, Z. Li, Y. Zhang, L. Xu, Q. Zhou e D. Han, *A New Methodology for Diesel Surrogate Fuel Formulation: Bridging Fuel Fundamental Properties and Real Engine Combustion Characteristics*, 10.1016/j.energy.2018.01.181, 2018.

[51] M. A. Carr, *An Experimental And Modeling-Based Study Into The Ignition Delay Characteristics Of Diesel Surrogate Binary Blend Fuels*, ICEF2011-60027, Morgantown, West Virginia, 2011.

[52] Y. Pei, M. Mehl, W. Liu, T. Lu, W. J. Pitz e S. Som, *A Multi-Component Blend As A Disel Fuel Surrogate For Compression Ignition Engine Applications*, ASME 2014 Internal Combustion Engine Division Fall Technical Conference; ICEF2014, Columbus, 2014.

[53] www.app.knovel.com.

[54] https://combustion.llnl.gov/mechanisms/surrogates/diesel-surrogate-detailed-and-reduced.

[55] https://ecn.sandia.com.

[56] F. d. Santos e L. L. Moyne, *Spray Atomization Models in Engine Applications, from Correlations to Direct Numerical Simulations*, HAL Id: hal-01937437, 2018.

[57] L. M. Pickett, *Silicone mold analysis of internal nozzle geometry for baseline n-heptane "Spray H" condition*, Engine Combustion Network.

[58] G. D'Errico, S.-Y. Lee, M. Bardi e J. M. Garcia-Oliver, *Subtopic 2.1: Combustion Indicators Experiment and Modeling*, 3rd Workshop of the Engine Combustion Network, Ann Arbor, USA, 2014.

[59] R. Reitz, *Computer Modeling of Sprays*, Spray Technology Short Course, Pittsburgh, PA, 1996.

[60] R. Reitz e R. Diwakar, *Structure of High-Pressure Fuel Sprays*, SAE Int.J.Engines 870598, 1987.

[61] R. D. Reitz, *Modeling Atomization Processes in High-Pressure Vaporizing Sprays*, General Motors Research Laboratories, Warren, Michigan, 1987.

[62] J. Xin, L. Ricart e R. Reitz, *Computer Modeling of Diesel Spray Atomization and Combustion*, Combustion Science and Technology, Vol. 137, pp. 171-194, Wisconsin, 1998.

[63] M. F. J. Brunt e K. C. Platts, *Calculation of Heat Release in Direct Injection Diesel Engines*, SAE 1999-01-0187, Detroit, Michigan, 1999.